

# CHALMERS



## Low Altitude Airspace Monitoring at Sea Radar Signal Processing, Path Planning and Collision Avoidance

Master Thesis in Systems, Control and Mechatronics

MOHAMMED RAZAUL KARIM

---

Department of Signals and Systems

Chalmers University of Technology

Göteborg, Sweden, 2015

EX020/2015



REPORT NO. EX020/2015

# Low Altitude Airspace Monitoring at Sea

Radar Signal Processing, Path Planning and Collision Avoidance

MOHAMMED RAZAUL KARIM

Department of Signals and Systems  
Chalmers University of Technology  
Göteborg, Sweden, 2015

Low Altitude Airspace Monitoring at Sea  
Radar Signal Processing, Path Planning and Collision Avoidance  
MOHAMMED RAZAUL KARIM

© MOHAMMED RAZAUL KARIM, 2015

Technical report no EX020/2015  
Department of Signals and Systems  
Chalmers University of Technology  
SE-412 96 Göteborg  
Sweden  
Email: mrkarim.chalmers@gmail.com

Cover:  
Department of Engineering Cybernetics, NTNU  
Trondheim, Norway 2015

Low Altitude Airspace Monitoring at Sea  
Radar Signal Processing, Path Planning and Collision Avoidance  
Mohammed Razaul Karim  
Department of Signals and Systems  
Chalmers University of Technology  
Göteborg, Sweden, 2015

## **Abstract**

There is an increasing trend to make lightweight unmanned aerial vehicles (UAV). One way of making UAV lighter is to reduce the weight of UAV on-board sensors. But there is always a limitation on making electronic device lighter. For our more specific problem, we are considering to control UAV from the UAV ground station which is mounted in the moving ship. As UAV will fly in the low altitude airspace and within a certain distance of the ship, we are studying the possibility of using ship navigational sensors and mounting some other sensors in the ship for path planning and collision avoidance of UAV, which will reduce on-board UAV sensors, hence reduced cost and lighter UAV. Thus, UAV path planning and collision avoidance will be taken care of from the ship having automatic dependent surveillance – broadcast (ADS-B) receiver for detecting cooperative aerial vehicles and ship radar for detecting non-cooperative aerial vehicles in low altitude airspace.

Ship radar is mounted in a ship for collision avoidance and navigation in the sea. It provides distance and bearing of ships and other marine vehicles in the vicinity of the radar scanner. Ship radar usually cannot detect high speed object because of its low speed object detection capacity. It is not possible to monitor high altitude air space by using ship radar for its small vertical beam width. ADS-B is a new technology used for sharing aircraft information (position, velocity, etc.). This is a cooperative technology. Thus, an aircraft without "ADS-B Out" device cannot be tracked using "ADS-B In" device.

In this thesis, a feasibility study is done for existing frequency modulated continuous wave (FMCW) ship radar for detecting non-cooperative aerial vehicles in low altitude airspace. An algorithm is developed and simulated for producing a flyable path of UAV for autonomous completion of search mission. Based on ADS-B and ship radar data, a collision detection and avoidance algorithm is also simulated for detecting collision with any cooperative and non-cooperative aerial vehicle and modifying the path for collision avoidance. The broad goal of the thesis is to integrate the ship radar for low altitude flight detection, ADS-B out data, automatic identification system (AIS) data, data from UAV flight management system and other sensors for collision avoidance of UAV and implementing electronic map for simultaneous operation with air and sea.

Keywords: FMCW marine radar, Radar signal processing, Flyable path, Collision avoidance, Differential geometry, Pythagorean hodograph, Quaternion.

## **Acknowledgement**

This publication is part of my master thesis work in Chalmers University of Technology, thanks to Swedish Institute Study Scholarship. Thanks to my supervisor Tor Arne Johansen and my examiner Bo Egardt for their guidance and Norwegian University of Science and Technology for giving me opportunity to work in their lab and providing required equipment.

# Table of Contents

Abstract	i
Acknowledgement	ii
Table of Contents	iii
1 Introduction	1
1.1 Objectives	2
1.2 Structure of the Thesis	2
2 Radar Systems	3
2.1 Introduction	3
2.2 Marine Radar	3
2.3 Radar Range Equation	3
2.4 Radar Range Resolution	4
2.5 Radar System	6
2.5.1 Transmitter	6
2.5.2 Duplexer	7
2.5.3 Receiver	7
2.5.4 Signal Processor	8
2.5.4.1 Input of Signal Processor	8
2.5.4.2 Matched Filter	9
2.5.4.3 Ambiguity Function	10
2.5.4.4 Stretched Processing	12
2.5.4.5 Sea Clutter Model	13
2.5.4.6 Rain Clutter Model	18
2.5.4.7 Slow Moving Clutter Rejection	19
2.5.5 General Purpose Computer	19

2.5.6	Radar Display	21
2.6	Using FMCW Ship Radar for Low Altitude Airspace Monitoring	21
3	Other Sensors	23
3.1	Introduction	23
3.2	Global Navigation Satellite System (GNSS)	23
3.3	Automatic Dependent Surveillance – Broadcast (ADS-B)	23
3.4	Automatic Identification System (AIS)	24
4	Flyable Path Generation and Collision Avoidance	25
4.1	Introduction	25
4.2	Flyable Path Generation in 2D	26
4.2.1	Problem Formulation	26
4.2.2	Dubins Path Generation using Analytical Geometry	26
4.2.3	Dubins Path Generation using Differential Geometry	33
4.2.4	Flyable Path with Continuous Curvature	37
4.3	Flyable Path Generation in 3D	42
4.3.1	Problem Formulation	42
4.3.2	Flyable Path with Continuous Curvature and Torsion	42
4.4	Flyable Lawn-mower Search Path Generation	45
4.4.1	Problem Formulation	45
4.4.2	Flyable Search Path with Continuous Curvature and Torsion	45
4.5	Collision Avoidance	48
5	Conclusion	53
6	Future Work	53
7	References	55

# 1. Introduction

Typical civil applications of unmanned aerial vehicles (UAV) operation from ship are environmental monitoring (e.g. oil spill), mapping and survey (geological, marine, marine mammals, biological), icebergs and ice floes monitoring, monitoring of ship traffic, etc.

We will operate low cost fixed wing UAV from moving ship for civil use, where UAV launching and retrieval system is independent of the type of ship – UAV will be launched from pneumatic launcher and captured using Net Recovery system. For autonomous operation of UAV, a flyable search path will be generated prior to launching of the UAV. We are considering 2D flyable lawn-mower search path generation at a certain altitude and 3D flyable path generation for launching and retrieval. We assume that there is no mapped static obstacles in the sea environment. We will mount required sensors in the moving ship for continuously sensing unmapped static and dynamic obstacles during the flight. If an imminent collision is detected, 3D flyable path will be generated to avoid the collision without much deviating from the search path.

Sensors used for collision avoidance are two types – sensor for avoiding cooperative obstacles and sensor for avoiding non-cooperative obstacles. In general, these sensors are mounted in the UAV on-board. Mounting these in the ship has some benefits such as using same sensors for operating more than one UAV, making UAV lighter and cost effective, and using ship navigational sensors to assist collision avoidance. As UAV will fly in the low altitude airspace and within a certain distance of the ship, we are studying the possibility of using ship navigational radar for detecting non-cooperative obstacles and we will mount automatic dependent surveillance – broadcast (ADS-B) receiver in the ship to detect cooperative aerial vehicles.

Military security and surveillance radars are being used for both airspace and marine surveillance. One of the low cost radar systems based on solid state radar transmitter is Harrier security and surveillance radar system which is used for simultaneous air and marine detection [1]. An x-band radar based airborne collision avoidance system is tested in [2] – specifications of the radar is not fully disclosed in the paper. We are studying the possibility of using very low cost civil marine radar for simultaneous air and marine detection.

There has been a lot of research in autonomous take-off and landing of UAV. An algorithm for autonomous take-off and landing of low cost fixed wing UAV is presented in [3]. An autonomous take-off and landing control for unmanned helicopter is designed and implemented in [4] and autonomous flight control law is designed and implemented in [5]. A system for net recovery of fixed wing UAV is tested in [6]. A field test is described in [7] where UAV is used as communication relay for autonomous underwater vehicles. Co-operative path planning and collision avoidance of fixed wing UAV is well described in [8].

In this thesis, an algorithm is developed and simulated for producing a flyable path of UAV for autonomous completion of search mission. Based on the algorithm presented in [8], a modified analytical geometric approach is used to generate 2D Dubins path. 2D Dubins path is also generated using differential geometry, which is easy to implement compared to the one in [8]. Finally, complex algebra method of Pythagorean Hodograph is used for 2D flyable path generation. Similar method is used in [9] for planar hermite interpolation. 3D flyable path is generated using Pythagorean Hodograph based on quaternion. This method is used in [10] for special hermite interpolation. Finally, based on 2D

and 3D path planning algorithm, a flyable search path is generated for autonomous completion of search mission and a collision avoidance algorithm based on conflict detection and resolution method [11, 12, 13] is simulated.

In conclusion, a feasibility study is done for existing frequency modulated continuous wave (FMCW) ship radar for detecting non-cooperative aerial vehicles in low altitude airspace. An algorithm is developed and simulated for producing a flyable path of UAV for autonomous completion of search mission. Based on ADS-B and ship radar data, a collision detection and avoidance algorithm is also simulated for detecting collision with any cooperative and non-cooperative aerial vehicle and modifying the path for collision avoidance. The broad goal of the thesis is to integrate the ship radar for low altitude flight detection, ADS-B out data, automatic identification system (AIS) data, data from UAV flight management system and other sensors for collision avoidance of UAV and implementing electronic map for simultaneous operation with air and sea.

## **1.1 Objectives**

The objectives of the thesis are to

1. Provide a feasibility analysis on existing FMCW ship radar for low altitude airspace monitoring.
2. Develop and simulate an algorithm for producing flyable path of UAV for autonomous completion of search mission.
3. Provide the simulation result of algorithm for collision detection and avoidance of the UAV based on available information from ship radar and ADS-B.
4. Provide a brief understanding to integrate the ship radar data, ADS-B out data, AIS data, data from UAV flight management system and other sensors to implement an electronic map for simultaneous operation with air and sea.

## **1.2 Structure of the Thesis**

Chapter 2 describes the theory of radar system and presents feasibility analysis of FMCW ship radar for detecting high speed aerial vehicles. Chapter 3 contains a description of other sensors, which are proposed to use along with ship radar, for operation of UAV in low altitude airspace in sea and to implement the electronic map for simultaneous operation with air and sea. In chapter 4, algorithms for producing flyable path and providing dynamic collision detection and avoidance of the UAV are explained and simulated.

## 2. Radar System

### 2.1 Introduction

This chapter describes the theory of radar system and presents feasibility analysis of FMCW ship radar for detecting high speed aerial vehicle. The radar theory part of the chapter describes very simple to state-of-art topics on radar system, which are important for understanding different aspects of FMCW ship radar. In the feasibility analysis part, more generalized description is presented on FMCW ship radar.

### 2.2 Marine Radar

There are four broad classes of radar: ground based radar, marine radar, airborne radar and spaceborne radar. The detail description of how marine radar detects target is presented in [14]. A brief overview of sea clutter is given in chapter 15 of [15]. Mathematically rigorous explanation of sea clutter and its exploration in radar systems is presented in [16]. Filtering methods of rain clutter is presented in [17, 18]. In depth theory of signals return in navigational systems from fluctuating target is presented in [19].

Use of civil marine radar includes merchant ships, small commercial vessels, fishing vessels, leisure craft, high speed craft, search and rescue craft, buoy tenders, coastal surveillance systems, Vessel Traffic Services (VTS), etc. The purposes of these radars are assessing traffic situation, monitoring the speed and heading of other marine vehicles for collision avoidance, monitoring progress of own ship relative to sea marks or coastal features, detecting ice, wrecks and other popup obstacles, maintaining anchor watch, etc. [14]. Marine radar functionalities vary according to user needs and type of radars, but all of the marine radar manufacturers and users have to follow marine regulations. Different organizations define international regulations. International Maritime Organization (IMO) works for international maritime safety and protection of the marine environments. IMO is a sister organization of International Civil Aviation Organization (ICAO) [15]. International Association of Marine Aids to Navigation and Lighthouse Authorities (IALA) works for defining operational and technical requirements of VTS radar. The United Nations Convention on the Law of the Sea (UNCLOS) defines international law and customs for using sea [14].

Marine radars operate at frequency band of 2900–3100MHz (IMO name is 3GHz) or 9200–9500MHz (IMO name is 9GHz). According to regulation, ships have to use 9GHz radar set and are encouraged to use 3GHz radar as second set (3GHz radar works well in case of precipitation). Scanner aperture should be more than 3m for 3GHz radar set and 1m for 9GHz radar set, respectively, for better resolution. Small azimuth beam width has to be chosen for low level of sea clutter. VTS radar set has different regulations, see [14] for detail.

### 2.3 Radar Range Equation

Let us consider a pulsed radar with pulse repetition interval  $T_p$ , pulse duration  $T$ , transmitted power of the pulse  $P_t$ , and average power of the radar

$$P_{av} = \frac{P_t T}{T_p}$$

Considering a directive antenna with gain  $G$ , power density of the transmitted pulse at distance  $R$  is

$$P_{td} = \frac{P_t G}{4\pi R^2}$$

Gain of a lossless scanner with horizontal (azimuth) beam width  $\phi$ , and vertical (elevation) beam width  $\theta$  is given by

$$G = \frac{4\pi}{\phi\theta},$$

where  $4\pi$  is the total steradians in a sphere and  $\Omega = \phi\theta$  is solid angle of the beam in steradians. Considering loss for unavoidable resistance, mismatch, etc. commonly used approximation of gain is

$$G = \frac{26000}{\Omega_{\text{deg}}},$$

where  $\Omega_{\text{deg}} = \phi_{\text{deg}}\theta_{\text{deg}}$ . Gain of the scanner can also be given by

$$G = \frac{4\pi A_e}{\lambda^2},$$

where  $A_e$  is the antenna effective aperture area and  $\lambda$  is the wavelength of the radar transmitted signal. Reflected power density from the target RCS  $\sigma$  to the radar can be calculated by

$$P_{rd} = \frac{P_t G}{4\pi R^2} \cdot \sigma \cdot \frac{1}{4\pi R^2}$$

If the radar receiver effective area is also  $A_e$ , total received power for a transmitted pulse is

$$P_r = \frac{P_t G}{(4\pi R^2)^2} \sigma A_e$$

Substituting the value of  $A_e$ , total received power for a transmitted pulse becomes

$$P_r = \frac{P_t G^2 \lambda^2 \sigma}{(4\pi)^3 R^4}$$

Considering propagation loss factor  $L_a$  (includes absorption for atmosphere, rain, mist, clouds, refraction loss and multipath propagation) and loss factor  $L_\mu$  due to microwave losses and filter mismatch losses, total received power for a transmitted pulse is

$$P_r = \frac{P_t G^2 \lambda^2 \sigma}{(4\pi)^3 R^4 L_a L_\mu} \quad (1)$$

Similar equation can also be derived for sea clutter in case of marine radar. Hence, received clutter power for a transmitted pulse can be written as

$$P_c = \frac{P_t G^2 \lambda^2 \sigma_0 A_c}{(4\pi)^3 R^4 L_a L_\mu}, \quad (2)$$

where  $\sigma_0$  is the normalized sea clutter RCS and  $A_c$  is illuminated area by the radar. Considering radar viewing geometry, beam shape, range resolution, etc. calculation method of  $A_c$  is shown in chapter 12 of [16]. Calculation of  $\sigma_0$  depends on the sea conditions, grazing angle and aspect angle.

Radar input noise power to a lossless scanner can be represented as

$$P_{ni} = kT_o B,$$

where  $k$  is Boltzmann's constant,  $T_o$  is input noise temperature in Kelvin, and  $B$  is matched filter bandwidth. Considering system gain and thermal noise generated in the system output noise power can be modelled as

$$P_n = kT_o B F_n, \quad (3)$$

where  $F_n$  is called noise figure.

## 2.4 Radar Range Resolution

Pulse radar use single antenna for both transmitting and receiving the signal. After transmitting, a pulse, antenna is switched from transmitting mode to receiving mode. For transmitting pulse duration  $T$ , minimum distance at which object cannot be detected is given by

$$R_{min} = \frac{cT}{2},$$

where  $c$  is the speed of the transmitted wave. Similarly, maximum unambiguous range from which back scattered signal is returned to the receiver before starting to transmit the next pulse is given by

$$R_{max} = \frac{c(T_p - T)}{2}$$

There is a minimum required distance between two objects to be detected as distinct objects by the radar is called range resolution. Range resolution is given by

$$\Delta R = \frac{cT}{2}$$

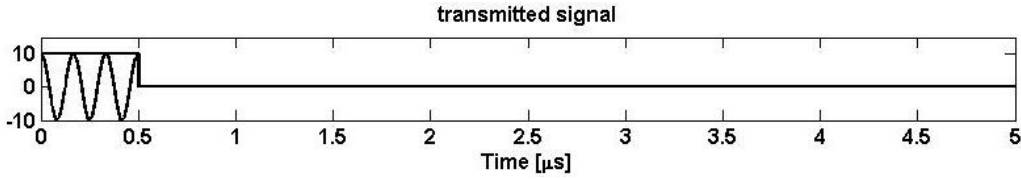


Figure-1: Single frequency modulated transmitted signal (frequency is scaled for visualization)

In case of single frequency modulation of transmitted signal, see Figure 1, range resolution  $\Delta R = 75 \text{ m}$ . In the power spectral density curve,  $-3\text{dB}$  bandwidth  $B$  of this type of pulse is approximately

$$B = \frac{1}{T}$$

Thus, range resolution can be written as

$$\Delta R = \frac{c}{2B}, \quad (4)$$

showing that the radar range resolution can be improved by increasing the bandwidth. One way of increasing bandwidth is to reduce the pulse width. However, this will decrease the pulse duration. It is very hard to generate short duration pulses with enough energy [20]. Increasing bandwidth with enough average transmission power can be achieved with pulse compression technique.

Among different types of pulse compression waveform, linear frequency modulation (LFM) waveform is discussed in this section. Let the transmitted signal have carrier frequency  $f_c = 9405 \text{ MHz}$  and waveform generation section of the transmitter generates LFM waveform with tuneable bandwidth  $B$ ,  $0 - 10 \text{ MHz}$ , also called swept bandwidth. Thus, actual frequency of the transmitted signal is from  $9400 \text{ MHz}$  to  $9410 \text{ MHz}$  in case of  $10 \text{ MHz}$  bandwidth of LFM waveform. Figure 2 shows an LFM transmitted signal with duty cycle 0.2.

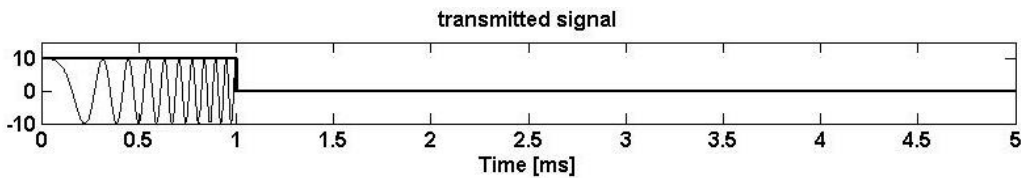


Figure-2: LFM transmitted signal (frequency is scaled for visualization)

Pulse compression filter consists of matched filter to maximize SNR. In case of LFM waveform, matched filter is usually followed by a weighting filter to reduce the side lobe gain at the cost of reduced value of SNR. It will be shown in section 2.5.4, for large time-bandwidth product, at the output of matched filter,  $-3 \text{ dB}$  width of the compressed time domain pulse are  $0.886/B$  and side lobe level is  $-13.2 \text{ dB}$ . In [15], side lobe level is reduced to  $-40 \text{ dB}$  in expense to the loss of SNR for  $1.15 \text{ dB}$

using Taylor weighting filter and  $-3$  dB width of the compressed time domain pulse increased to  $1.25/B$ . Considering the width of the compressed pulse as  $1/B$ , range resolution of the compressed pulse is same as in equation (4). Thus, range resolution of a compressed waveform does not depend on time duration of the pulse; rather it depends on the swept bandwidth. In our case, Figure 2, for swept bandwidth of 10 MHz, range resolution is  $\Delta R = c/2B = 15$  m. If we use single frequency modulation technique for same pulse width, bandwidth  $B = 1/T = 1$  kHz, range resolution  $\Delta R = c/2B = 150$  km is not reasonable at all.

## 2.5 Radar System

The basic block diagram of a radar is shown in Figure 3. The transmitter generates high voltage radio frequency signal. Duplexer is used for time sharing of single antenna for transmitting high voltage radio frequency signal and reception of low voltage reflected echo. Antenna or scanner is used to propagate electromagnetic wave to detect object. For continuous wave radar, separate transmitting and receiving antennas are used to avoid interruption. In this case, duplexer is not used. The purpose of the receiver is to receive reflected echoes. Most modern radar receivers are superheterodyne. The signal processor is used for pulse compression filtering and radar clutter rejection. General purpose computer is used for detection, thresholding, parameter estimation and tracking. Finally, radar display is used for digitally displaying the radar image. All of these sections are briefly described below.

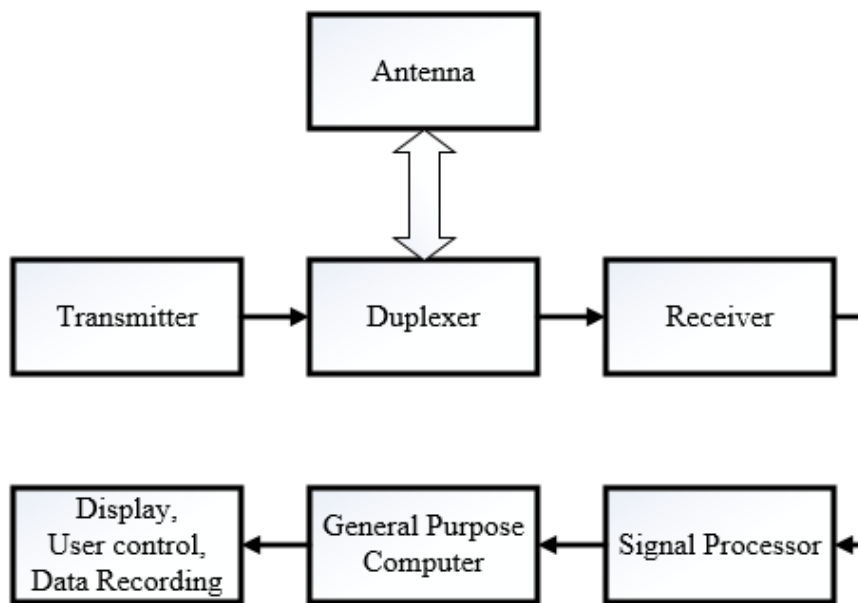


Figure-3: Basic block diagram of radar

### 2.5.1 Transmitter

The transmitter of the radar has two sections- low voltage section and high voltage section, see Figure 4. Transmitting waveform is generated in low voltage section. In this section, pulsed radar with small duty cycle usually use single frequency, i.e. pure sine wave, modulation technique to transmit high frequency pulse. Radars having facility of pulse compression use different types of modulation techniques such as linear frequency modulation, nonlinear frequency modulation, phase modulation, etc. In high voltage section, this wave form is amplified to provide enough energy for transmission. In general, two types of amplifier is used in this section- high power tube amplifiers (e.g. Klystron, Traveling Wave Tube, Crossed Field Amplifier, and Magnetron) and solid state RF power amplifiers. Magnetron is very common in civil marine radar because this radar does not require very high

transmitter power and Doppler processing to separate moving target. Small and light weight marine radars, e.g. Simrad broadband 4G radar, have started to use solid state RF power amplifiers. Solid state RF power amplifiers have very low output power, 10-100 W, comparing to vacuum tube amplifier, 10KW-1MW. Output power of this solid state amplifier is increased by series-parallel operation with more than one stage, e.g. a module may consists of 8 transistor – first stage has two transistor in series, second stage has 2 transistor in parallel and third stage has four transistor in parallel [21]. Solid state amplifier cannot operate at high peak power. Thus, for providing enough transmission energy, large duty cycle is required. Hence, for high resolution, pulse compression technique should be applied in case of solid state amplifier.

### 2.5.2 Duplexer

Duplexer is used for time sharing of single antenna for transmitting radar signal and reception of reflected echo. During transmission of signal, duplexer protect receiver from high voltage. Transmit/receive (T/R) Radio Frequency Switch is used as duplexer for high transmission power. For continuous wave radar, separate transmitter and receiver are used to avoid interruption.

### 2.5.3 Receiver

While transmitted signal has high power, 10 kW – 1 MW, reflected echoes received by the receiver are of very low power, 10  $\mu$ W – 1 mW [21]. After reception of reflected echoes a low noise amplifier is used for amplifying intended signal and reducing noise followed by a mixer which down convert the signal to intermediate frequency (IF) signal. Then, multistage IF amplifier is used for amplifying the down converted echoes. After that, in phase (I) and quadrature (Q) demodulation is done followed by the amplifier and analogue-to-digital converter. If the radar detector does not need the phase information of the received signal, quadrature demodulation is not required. Finally, digital signal is sent to signal processor. Radar transmitter low voltage site and receiver share same oscillator for coherent system and have some similar operation.

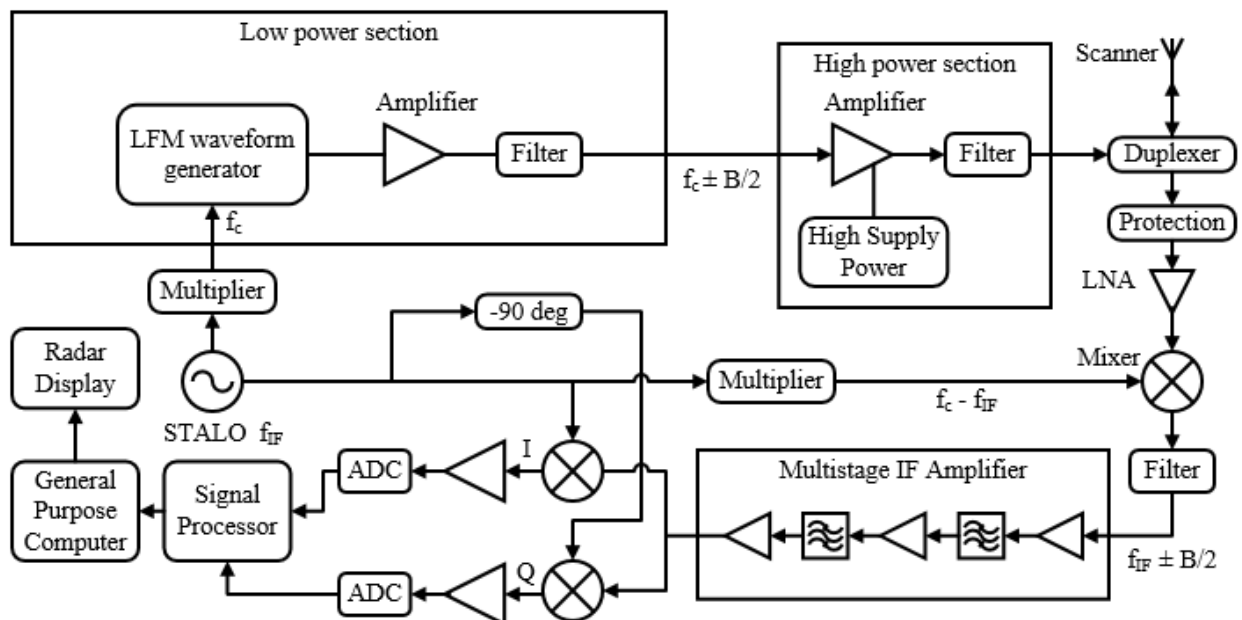


Figure-4: Radar block diagram with details on transmitter and receiver.

## 2.5.4 Signal Processor

The signal processor of the radar system comprises pulse compression filter and clutter rejection filter. There are different types of pulse compression waveforms, e.g. Linear Frequency Modulated (LFM) waveform, Nonlinear Frequency Modulated (NLFM) waveform, Phase Modulated waveform, Time Frequency Modulated waveform. Radar clutter is simply defined as the reflected echoes from unwanted objects, e.g. backscatter from ground, sea, rain, birds, etc. Object in one radar may be regarded as clutter in another type of radar. As the emphasis of this chapter is on FMCW ship radar with solid state high power amplifier, detailed description of pulse compression filtering for LFM waveform, sea clutter and rain clutter are presented.

### 2.5.4.1 Input of Signal Processor

Consider first the input signal of the signal processor. LFM pulse compression filtering is usually done digitally. In Figure 4, analogue demodulator is used for extracting baseband I and Q components and separate ADC is used for analogue-to-digital conversion of these two baseband signals. It is also possible to use Direct Digital Downconversion technique. In this technique, digital signal processing (DSP) system of analogue-to-digital converter evaluates complex envelop of the received signal at intermediate frequency. Here, performance is not degraded by amplitude and phase imbalance. In summary, the input of the signal processor is complex envelop sequences of the received signal formed by either extracting I and Q components and then converting to digital signals using two ADC, or Direct Digital Downconversion technique, see chapter 25 of [15]. Complex envelope is used for both amplitude and phase information of the received signal. Transmitted LFM waveform with carrier frequency  $f_c$ , bandwidth  $B$ , pulse width  $T$ , pulse repetition interval  $T_p$ , can be represented mathematically as

$$x(t) = \begin{cases} A \cos 2\pi \left( f_c + \frac{B}{2T} t \right) t = A \cos \left( 2\pi f_c t + \pi \frac{B}{T} t^2 \right), & \text{where } -\frac{T}{2} \leq t \leq \frac{T}{2} \\ 0, & \text{otherwise} \end{cases} \quad (5)$$

The above equation is rather straightforward. We want to change the frequency of the pulse linearly from  $f_c - B/2$  to  $f_c + B/2$ . Instantaneous frequency of the above signal is the time derivative of the phase  $2\pi f_c t + \pi \frac{B}{T} t^2$  multiplied by  $1/2\pi$ . Thus, equation of the instantaneous frequency is written as  $f = f_c + (B/T)t$ . Figure 5 shows the plot of the equation.

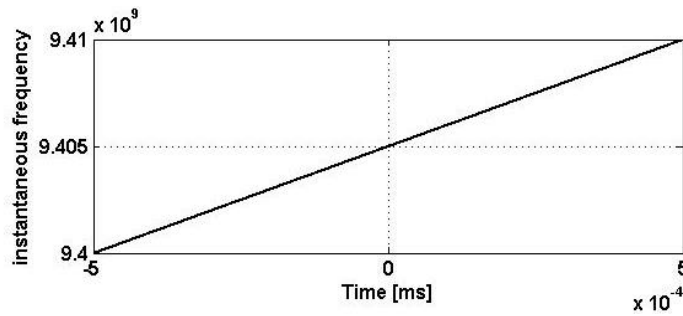


Figure-5: Instantaneous frequency of LFM waveform

The amplitude and phase shift of the equation (5) is  $A$  and  $\pi \frac{B}{T} t^2$  respectively. So, complex envelop of the equation is

$$u(t) = A \exp \left( j 2\pi \left( \frac{B}{2T} t \right) t \right); \text{ for } -\frac{T}{2} \leq t \leq \frac{T}{2} \quad (6)$$

Signal  $x(t)$  is transmitted signal where amplitude was constant. When the signal is reflected back, amplitude depends on the reflected power, say  $r(t)$ , frequency is changed by Doppler frequency and time delay is introduced. The reflected signal can be represented as

$$y(t) = \begin{cases} r(t) \cos\left(2\pi(f_c + f_d)(t - \tau) + \pi\frac{B}{T}(t - \tau)^2\right), & \text{where } -\frac{T}{2} \leq t \leq \frac{T}{2}, \\ 0, & \text{otherwise} \end{cases}$$

which is multiplied by reference signal  $2 \cos(2\pi(f_c - f_{IF})t)$  and filtered to down convert the signal to intermediate carrier frequency  $f_{IF}$ . Using identity  $2 \cos A \cos B = \cos(A + B) + \cos(A - B)$  and removing high frequency term, for  $-\frac{T}{2} \leq t \leq \frac{T}{2}$ , the filtered output is

$$\begin{aligned} y(t) &= r(t) \cos\left(2\pi(f_c + f_d)(t - \tau) + \pi\frac{B}{T}(t - \tau)^2 - 2\pi(f_c - f_{IF})t\right); \text{ for } -\frac{T}{2} \leq t \leq \frac{T}{2} \\ &= r(t) \cos\left(2\pi f_{IF}t + 2\pi\left(f_d - \frac{B}{T}\tau + \frac{B}{2T}t\right)t - 2\pi(f_c + f_d)\tau + \pi\frac{B}{T}\tau^2\right); \text{ for } -\frac{T}{2} \leq t \leq \frac{T}{2} \end{aligned}$$

The envelop of this signal

$$v(t) = r(t) \exp\left(j2\pi\left(\left(\frac{B}{2T}t + f_d - \frac{B}{T}\tau\right)t - (f_c + f_d)\tau + \frac{B}{2T}\tau^2\right)\right); \text{ for } -\frac{T}{2} \leq t \leq \frac{T}{2}, \quad (7)$$

is the input of the signal processor.

#### 2.5.4.2 Matched Filter

Let us consider a filter with impulse response  $h(t)$ . The input signal of the filter is the receiver output which is the sum of transmitted signal  $s(t)$  and Gaussian white noise  $n(t)$ . Thus, output of the filter is the sum of

$$s_o(t) = s(t) * h(t)$$

and

$$n_o(t) = n(t) * h(t)$$

Autocorrelation function of Gaussian white noise, filter input noise, is represented as

$$R_n(t) = \frac{N_0}{2} \delta(t),$$

where  $N_0$  is real constant and  $\delta$  is direct delta function, and the power spectral density of the filter input noise is, which is the Fourier transform of autocorrelation function  $R_n(t)$ ,

$$S_n(\omega) = \frac{N_0}{2}$$

For filter autocorrelation function  $R_h(t)$ , autocorrelation function of filter output noise is

$$R_{n_o}(t) = R_n(t) * R_h(t) = \frac{N_0}{2} \delta(t) * R_h(t) = \frac{N_0}{2} R_h(t)$$

and the corresponding power spectral density is, Fourier transform of the above equation,

$$S_{n_o}(\omega) = \frac{N_0}{2} |H(\omega)|^2$$

We also know that total average output noise power is  $R_{n_o}(0)$ , which can be calculated as

$$R_{n_o}(0) = \frac{N_0}{2} R_h(0) = \frac{N_0}{2} \int_{-\infty}^{\infty} |h(u)|^2 du$$

Now, instantaneous peak signal power to average noise power,  $SNR(t)$ , can be written as

$$SNR(t) = \frac{|s_o(t)|^2}{R_{n_o}(0)} = \frac{|s(t) * h(t)|^2}{R_{n_o}(0)} = \frac{|\int_{-\infty}^{\infty} s(t-u)h(u) du|^2}{\frac{N_0}{2} \int_{-\infty}^{\infty} |h(u)|^2 du}$$

Schwarz inequality says that

$$\left| \int_{-\infty}^{\infty} s(t-u)h(u) du \right|^2 \leq \int_{-\infty}^{\infty} |s(t-u)|^2 du \cdot \int_{-\infty}^{\infty} |h(u)|^2 du$$

and the above inequality becomes an equality if  $h(u) = ks^*(t-u)$ . Hence, from Schwarz inequality, instantaneous peak signal power to average noise power can be rewritten as

$$SNR(t) \leq \frac{\int_{-\infty}^{\infty} |s(t-u)|^2 du}{\frac{N_0}{2}} = \frac{2E}{N_0},$$

where, according to Parseval's theorem, signal energy  $E = \int_{-\infty}^{\infty} |s(t-u)|^2 du$ .

We see that  $SNR(t)$  is maximum if equality holds, i.e. if equality occurs at  $t = t_0$  and  $k = 1$ ,

$$h(u) = s^*(t_0 - u)$$

Finally, considering  $t_0 = 0$  and replacing  $u$  by  $t$ , impulse response of the matched filter is

$$h(t) = s^*(-t) \quad (8)$$

A matched filter can be implemented in time domain by using digital convolution, matlab command `xcorr(ReceivedSignalWithNoise, TransmittedSignal)`, or in frequency domain by using FFT, matlab command `ifft(fft(ReceivedSignalWithNoise).*conj(fft(TransmittedSignal)))`. Cost of frequency domain implementation is relatively lower than digital convolution. For LFM waveform, matched filter can also be implemented using stretched processing, detailed on stretched processing is discussed in 2.5.4.4.

### 2.5.4.3 Ambiguity Function

Ambiguity function,  $x(t, f_d)$ , is not part of the signal processor. It is used to get an idea how a signal processor may respond to a received signal. It is the correlation between transmitted and reflected pulse, delayed in time and frequency. Ambiguity function can be represented as,

$$x(t, f_d) = \int_{-\infty}^{\infty} s^*(\tau - t)s(\tau)e^{-j2\pi f_d \tau} d\tau \quad (9)$$

From matched filter point of view,  $s(t)$  is a transmitted signal, only considering delay of the received signal for Doppler frequency, received signal from a moving object is

$$s(t)e^{-j2\pi f_d t}$$

Here, keeping all other delay to zero is helpful to find out relative delay for Doppler frequency shift. Now, matched filter output is

$$\begin{aligned} s_o(t) &= h(t) * s(t)e^{-j2\pi f_d t} \\ &= \int_{-\infty}^{\infty} h(t-\tau)s(\tau)e^{-j2\pi f_d \tau} d\tau \end{aligned}$$

Using the matched filter transfer function  $h(t)$  from (8), matched filter output becomes

$$s_o(t) = \int_{-\infty}^{\infty} s^*(\tau - t)s(\tau)e^{-j2\pi f_d \tau} d\tau$$

For pulse duration  $T$ , ambiguity function of an upward LFM signal can be derived as

$$x(t, f_d) = \begin{cases} A^2(T - |t|)\text{sinc}\left(\left(\frac{B}{T}t - f_d\right)(T - |t|)\right), & \text{where } |t| \leq T \\ 0, & \text{otherwise} \end{cases} \quad (10)$$

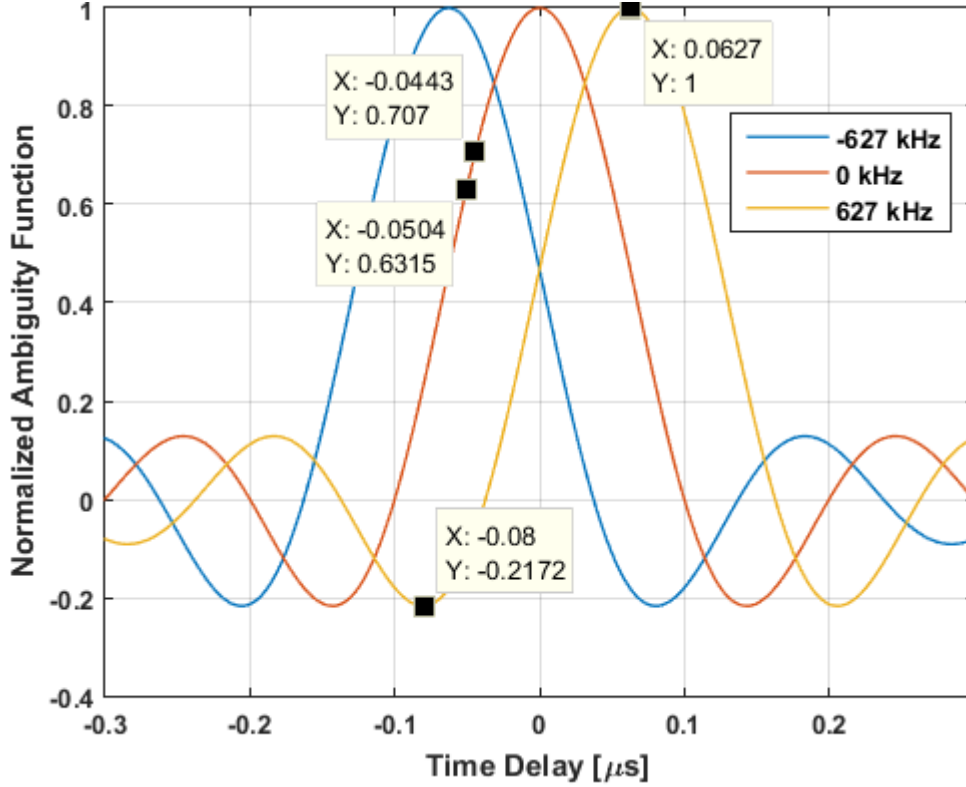


Figure-6: LFM ambiguity function for low speed object (10 m/s)

Figure 6 and Figure 7 show two plots of ambiguity function for LFM swept bandwidth  $B = 10$  MHz, pulse period  $T = 1$  ms and carrier frequency,  $f_c = 9405$  MHz. To show the effect of changing Doppler frequency, ambiguity function is plotted for different Doppler frequency rather than choosing Doppler frequency as continuous function. Doppler frequency in these figures are calculated for opening and closing target. The equation for Doppler frequency calculation of closing target is follows

$$f_d = \frac{2v}{c - v} f_0 \quad (11)$$

Figure 6 is plotted for object with velocity  $v = 10$  m/s. Corresponding calculated Doppler frequency is 627Hz and  $-627$ Hz for closing and opening targets respectively. Figure also shows that, for Doppler frequency 627Hz, relative time delay is  $0.0627\mu\text{s}$ . Range equivalent of this time delay is 9.405 m. This time delay can also be calculated by

$$t_{delay} = \frac{f_d T}{B} \quad (12)$$

FMCW ship radar use this type of modulation technique. In this radar, at any instant of time, frequency difference between transmitted and received signal is taken. From this frequency difference, distance of the object is measured. As explained before, this frequency difference is the sum of the frequency difference because of time delay and Doppler frequency. It is not possible to separate these two parts. In our case, for velocity  $10$  m/s, error due to Doppler frequency is small compared to the resolution of the radar signal processing unit.

Figure 7 is plotted for object with velocity  $200$  m/s. Corresponding calculated Doppler frequency is  $12.54$  KHz and relative time delay is  $1.254\mu\text{s}$ . Equivalent range for this time delay is  $188.1$  m which is much larger than resolution of a good FMCW ship radar signal processing unit.

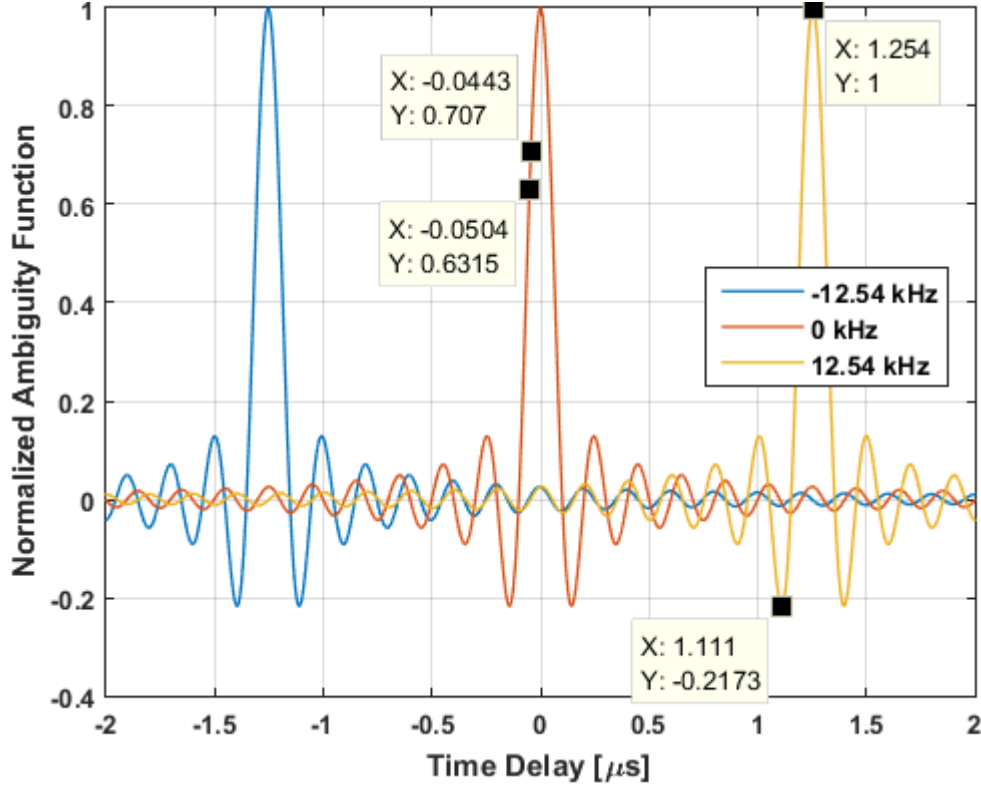


Figure-7: LFM ambiguity function for high speed object (200 m/s)

Similarly, for large Doppler frequency, e.g. 0.5 MHz, relative time delay is 50  $\mu\text{s}$  and corresponding error in range measurement is 7.5 km. Equation (12) is a simple equation for calculating relative time delay. It shows that relative time delay decreases with the increase of swept bandwidth and with decrease of pulse width. Figure 6 and Figure 7 also show  $-3\text{dB}$  and  $-4\text{dB}$  width and side lobe level of the filtered signal, which are same as explained in section 2.4.

#### 2.5.4.4 Stretched Processing

If radar signal processor bandwidth is much smaller than swept bandwidth of LFM waveform, stretched processing is used without loss of SNR and range resolution. Figure 8 shows a radar block diagram for stretched processing. In this technique, received signal, see section 2.5.4.1,

$$y(t) = \begin{cases} r(t) \cos\left(2\pi(f_c + f_d)(t - \tau) + \pi\frac{B}{T}(t - \tau)^2\right), & \text{where } -\frac{T}{2} \leq t \leq \frac{T}{2} \\ 0, & \text{otherwise} \end{cases}$$

is multiplied by reference waveform  $2 \cos(2\pi(f_c - f_{IF})(t - \tau_R) + \pi\frac{B_R}{T_R}(t - \tau_R)^2)$ , where  $\tau_R$ ,  $B_R$  and  $T_R$  are time delay, bandwidth and pulse width of reference waveform respectively. For simplicity, detail of this topic is presented in [15] and [22], considering same LFM slope for transmitted and reference waveform, i.e.  $\frac{B}{T} = \frac{B_R}{T_R}$ , and  $\tau_R = 0$ , complex envelop to the input of signal processor can be calculated as

$$v(t) = r(t) e^{j2\pi((f_d - \frac{B}{T}t) - (f_c + f_d)\tau + \frac{B}{2T}t^2)}; \text{ for } -\frac{T}{2} \leq t \leq \frac{T}{2}$$

Thus, the frequency offset is

$$\Delta f = f_d - \frac{B}{T}\tau$$

Rearranging the equation, the time delay is

$$\tau = -\frac{\Delta f T}{B} + \frac{f_d T}{B}$$

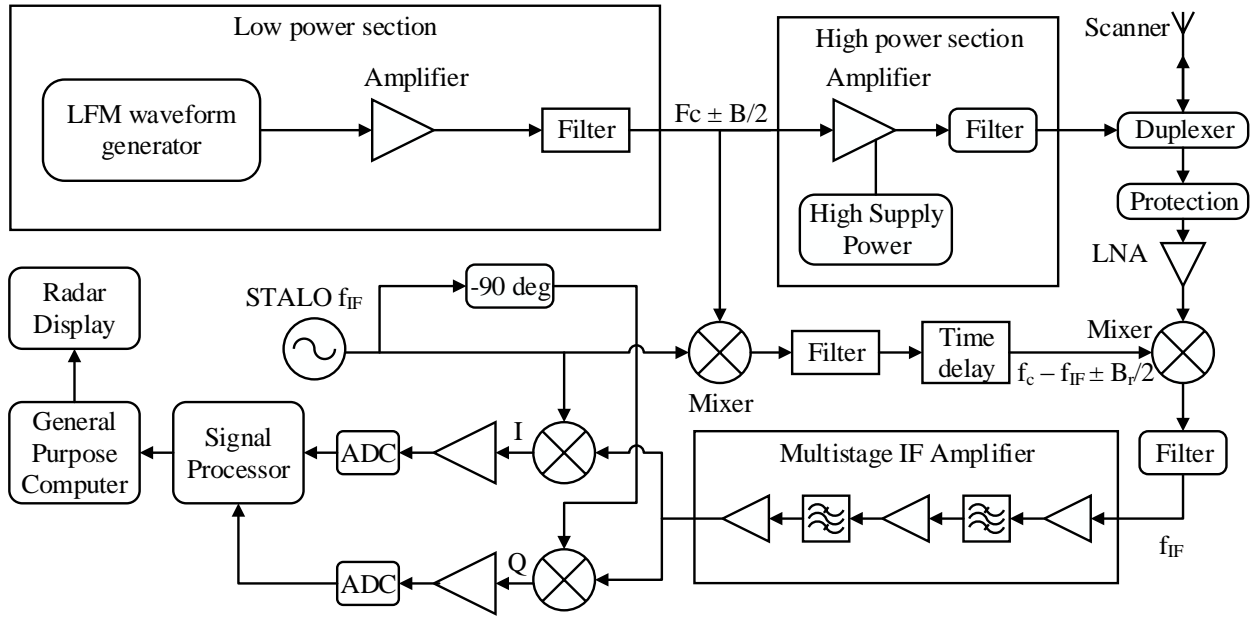


Figure-8: Radar block diagram with stretched processing.

For low speed or stationary object, ignoring  $f_d$ , simplified equation for the time delay becomes

$$\tau = -\frac{\Delta f T}{B}$$

Range of the object can be measured from this frequency difference  $\Delta f$ , for stationary or low speed object, as

$$R = \frac{c\tau}{2} = -\frac{c\Delta f T}{2B} \quad (13)$$

This equation is also used for measuring range of detected object in FMCW ship radar. Frequency difference,  $\Delta f$ , can be measured easily using spectrum analyser and it is not possible to separate  $f_d$  from the frequency difference. Thus, with the increase of  $f_d$ , range measurement error will increase, which is also shown in Figure 6 and 7.

#### 2.5.4.5 Sea Clutter Model

Radar clutter is simply defined as the reflected echoes from unwanted objects, e.g. backscatter from ground, sea, birds, precipitation, etc. Figure 9 shows dependence of sea clutter reflectivity on grazing angle and polarization. It is shown in equation (2) that normalized sea clutter RCS, or sea clutter mean power, or clutter reflectivity, is  $\sigma_0$ . Instantaneous power of radar return from a radar resolution cell varies around this mean.

For low resolution radar and large grazing angle, Rayleigh distribution can be used for modelling of radar return from the sea. For high resolution and low grazing angle radar, K distribution is used for modelling of radar return from the sea. Ship radar is used for very low grazing angle where scattering mechanism is more complex. Some features used for characterizing sea clutter are normalized clutter RCS  $\sigma_0$ , amplitude or power distribution of clutter, clutter spectrum, spatial variation, polarization and discrete clutter spike [16]. Radar return from the sea depends on sea state. Sea state is the numerical

description of ocean surface roughness. Table-1 shows the sea state according to World Meteorological Organization.

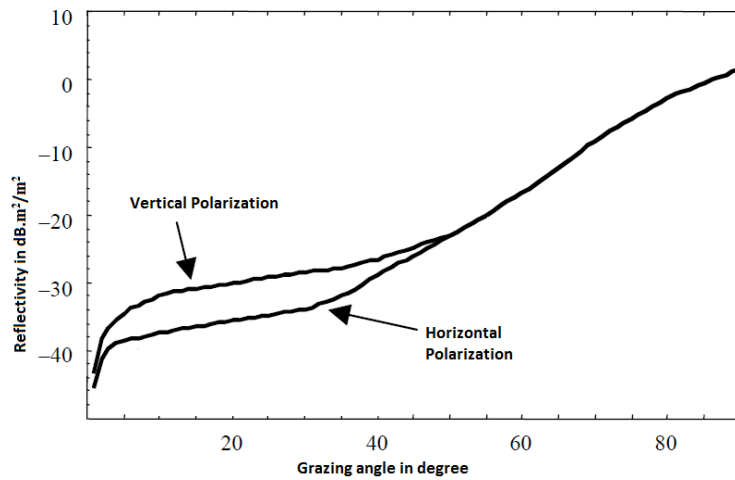


Figure-9: Variation of sea clutter reflectivity with grazing angle and polarization [16]

Table 1: Sea state (World Meteorological Organization)

Sea state	Average height of highest 1/3 of the waves (ft.)	Description
0	0	Calm, glassy
1	0-1/3	Calm, rippled
2	1/3-2	Smooth, wavelets
3	2-4	Slight
4	4-8	Moderate
5	8-13	Rough
6	13-20	Very rough
7	20-30	High
8	30-45	Very high
9	>45	Phenomenal

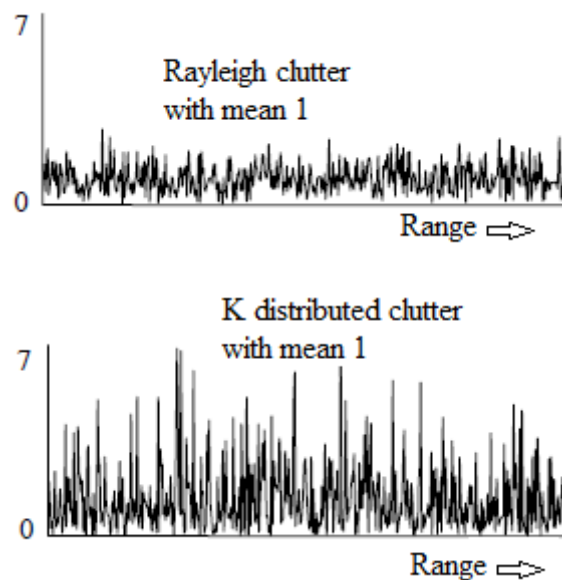


Figure-10: Typical sketch of Rayleigh and K distributed clutter [16]

Figure 10 shows typical Rayleigh and K distributed clutter model with equal mean amplitude. Rayleigh clutter has short temporal decorrelation time. K distributed clutter model is the mixture of Rayleigh distributed speckle and gamma distributed sea spike. Sea spike has large temporal decorrelation time.

If a radar receive backscatter from an intended target and sea clutter, the output of IF filter of the radar is

$$r(t) = E_I \cos \omega_o t + E_Q \sin \omega_o t ,$$

where  $E_I = E \cos \varphi = A + C_I$ ,  $E_Q = E \sin \varphi = C_Q$ ,  $A$  is the amplitude of signal return from target,  $C_I$  and  $C_Q$  are in phase and quadrature components of signal return from sea clutter respectively,  $\varphi$  is phase angle of the received signal. For low resolution radar, radar return from sea clutter can be considered as Gaussian distributed as follows

$$P(C_I) = \frac{1}{\sqrt{2\pi\psi^2}} \exp\left(-\frac{(E_I - A)^2}{2\psi^2}\right)$$

and

$$P(C_Q) = \frac{1}{\sqrt{2\pi\psi^2}} \exp\left(-\frac{E_Q^2}{2\psi^2}\right)$$

where  $\psi^2$  is variance of sea clutter. From probability theory, probability distribution of in phase and quadrature components of signal return from an intended target and sea clutter (echo) can be calculated as

$$P(E_I) = \frac{\partial C_I}{\partial E_I} P(C_I) = \frac{1}{\sqrt{2\pi\psi^2}} \exp\left(-\frac{(E_I - A)^2}{2\psi^2}\right)$$

and

$$P(E_Q) = \frac{\partial C_Q}{\partial E_Q} P(C_Q) = \frac{1}{\sqrt{2\pi\psi^2}} \exp\left(-\frac{E_Q^2}{2\psi^2}\right)$$

Now, the joint probability distribution of radar echo is

$$P(E_I, E_Q) = \frac{1}{2\pi\psi^2} \exp\left(-\frac{(E_I - A)^2 + E_Q^2}{2\psi^2}\right)$$

Considering mean intensity of clutter  $x \equiv 2\psi^2$ , joint probability distribution of clutter becomes

$$P(E_I, E_Q) = \frac{1}{\pi x} \exp\left(-\frac{(E \cos \varphi - A)^2 + (E \sin \varphi)^2}{x}\right) = \frac{1}{\pi x} \exp\left(-\frac{E^2 + A^2}{x}\right) \exp\left(\frac{2AE \cos \varphi}{x}\right)$$

Again, from probability theory, we know that

$$P(E, \varphi) = \begin{vmatrix} \frac{\partial E_I}{\partial E} & \frac{\partial E_I}{\partial \varphi} \\ \frac{\partial E_Q}{\partial E} & \frac{\partial E_Q}{\partial \varphi} \end{vmatrix} P(E_I, E_Q) = EP(E_I, E_Q) = \frac{E}{\pi x} \exp\left(-\frac{E^2 + A^2}{x}\right) \exp\left(\frac{2AE \cos \varphi}{x}\right)$$

and

$$\begin{aligned} P(E) &= \int_0^{2\pi} P(E, \varphi) d\varphi = \frac{2E}{x} \exp\left(-\frac{E^2 + A^2}{x}\right) \frac{1}{2\pi} \int_0^{2\pi} \exp\left(\frac{2AE \cos \varphi}{x}\right) d\varphi \\ &= \frac{2E}{x} \exp\left(-\frac{E^2 + A^2}{x}\right) I_0\left(\frac{2AE}{x}\right), \end{aligned} \quad (14)$$

where  $I_0$  is the modified Bessel's equation of first kind. Equation (14) is called Rice distribution of radar echo. For  $E^2 = z$ ,  $P(z)$  can be derived as

$$P(z) = \frac{1}{x} \exp\left(-\frac{z + A^2}{x}\right) I_0\left(\frac{2A\sqrt{z}}{x}\right) \quad (15)$$

Considering  $A = 0$ , equations (14) and (15) are reduced to

$$P(E) = \frac{2E}{x} \exp\left(-\frac{E^2}{x}\right) \quad (16)$$

and

$$P(z) = \frac{1}{x} \exp\left(-\frac{z}{x}\right) \quad (17)$$

Equation (16) and (17) are called Rayleigh model of clutter amplitude and Exponential model of clutter power respectively.

For high resolution radar with low grazing angle, mean intensity of clutter,  $x$  is a random variable and fits best with gamma distribution. Thus, probability distribution of mean intensity of clutter is

$$P(x) = \frac{b^v}{\Gamma(v)} x^{v-1} \exp(-bx),$$

where  $b$  and  $v$  are scale and shape parameter respectively and depend on radar parameter and sea conditions. An empirical model of shape parameter given in chapter 3 of [16], for grazing angle  $0.1^\circ - 10^\circ$ , is

$$\log_{10} v = \frac{2}{3} \log_{10}(\phi_{gr}) + \frac{5}{8} \log_{10}(A_c) - k_{pol} - \frac{1}{3} \cos(2\theta_{sw}),$$

where  $\phi_{gr}$  is grazing angle in degree,  $A_c$  is resolved area of radar,  $k_{pol}$  is a factor for radar polarization,  $\theta_{sw}$  is the aspect angle with swell direction. Equation (16) is rewritten showing the dependence of  $x$  as follows

$$P(E|x) = \frac{2E}{x} \exp\left(-\frac{E^2}{x}\right)$$

Hence, from probability theory, probability distribution of sea clutter is

$$\begin{aligned} P(E) &= \int_0^\infty P(E|x)P(x)dx = 2E \frac{b^v}{\Gamma(v)} \int_0^\infty x^{v-2} \exp\left(-bx - \frac{E^2}{x}\right) dx \\ &= \frac{4b^{(v+1)/2} E^v}{\Gamma(v)} K_{v-1}(2E\sqrt{b}), \end{aligned} \quad (18)$$

where  $K$  is modified Bessel function and corresponding equation for  $z = E^2$  is

$$P(z) = \frac{2b^{(v+1)/2} z^{(v-1)/2}}{\Gamma(v)} K_{v-1}(2\sqrt{zb}) \quad (19)$$

The mean value of the envelope can be calculated as

$$\langle E \rangle = \frac{\Gamma(3/2)\Gamma(v+1/2)}{\sqrt{b}\Gamma(v)} \quad (20)$$

Similarly, for showing the dependence of  $x$  in equation (14), reflected signal from target is included with the clutter, can be rewritten as

$$P(E|x) = \frac{2E}{x} \exp\left(-\frac{E^2 + A^2}{x}\right) I_0\left(\frac{2AE}{x}\right)$$

and probability distribution of echo is

$$\begin{aligned} P(E) &= \int_0^\infty P(E|x)P(x)dx \\ &= 2E \frac{b^v}{\Gamma(v)} \int_0^\infty x^{v-2} \exp(-bx) \exp\left(-\frac{E^2 + A^2}{x}\right) I_0\left(\frac{2AE}{x}\right) dx \end{aligned} \quad (21)$$

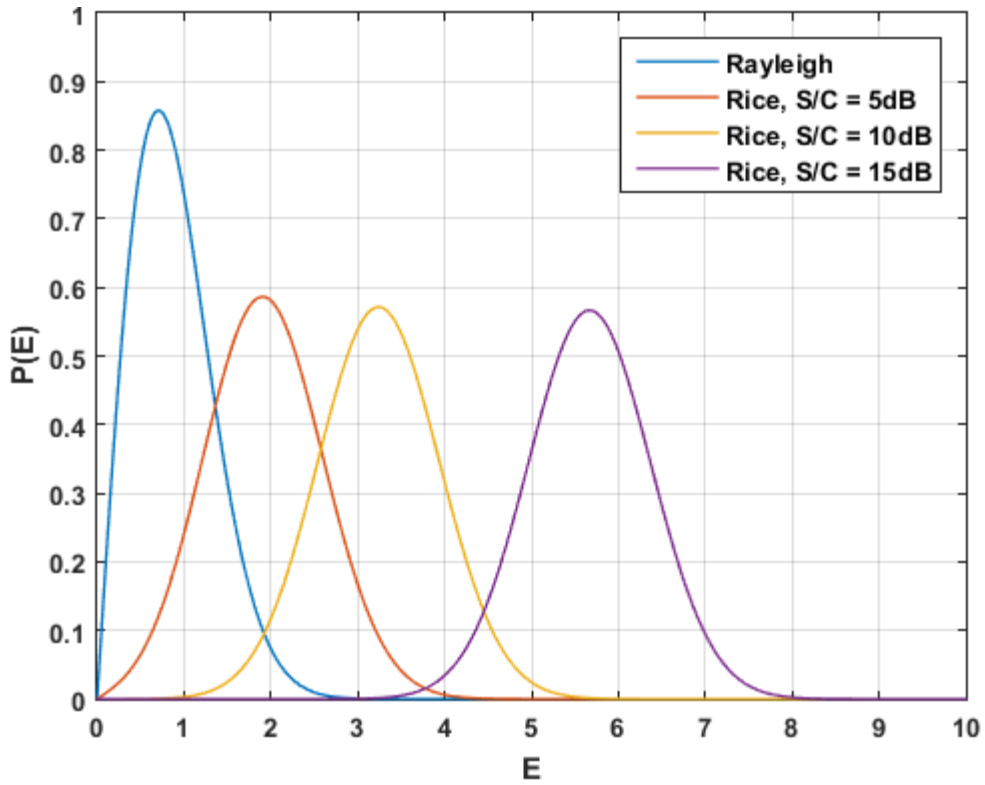


Figure-11: Rayleigh distributed clutter and Rice distributed echo for different signal-to-clutter ratio.

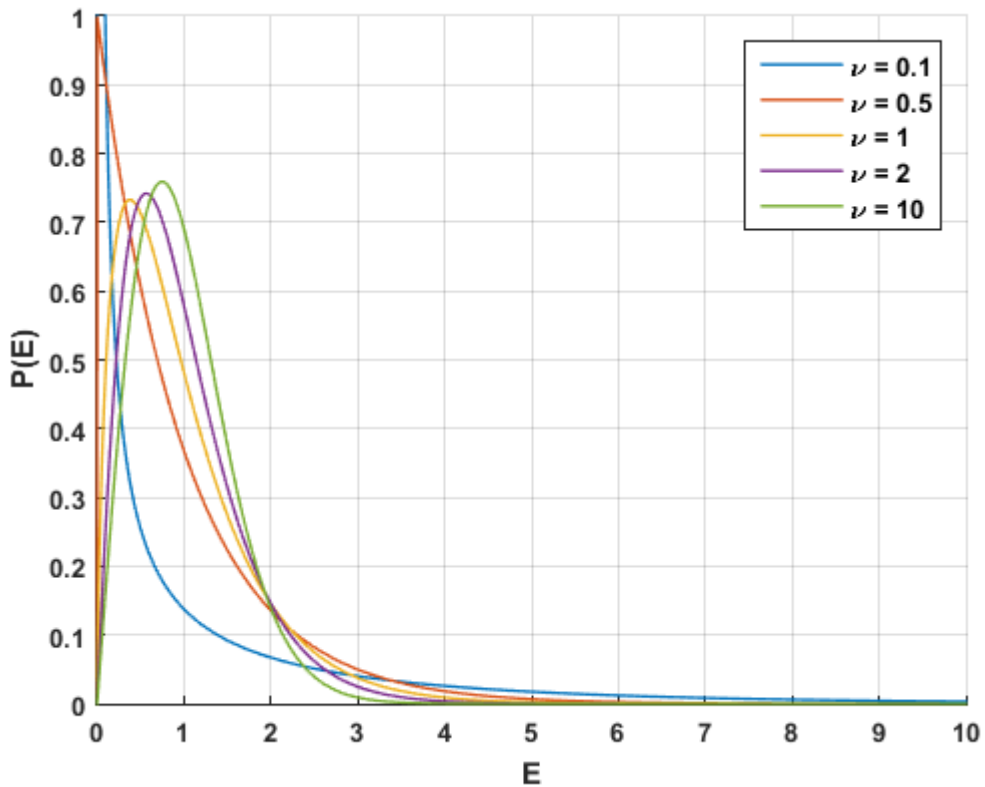


Figure-12: K distributed clutter for different shape parameter. Scale parameter is calculated for unity mean value of envelope using equation (20).

Equation (21) is called homodyned K process and has to be evaluated numerically. In another method introduced by Jakeman and Tough, reflected signal amplitude from target is also considered as gamma distributed. The resultant probability distribution can be represented as

$$P(E) = 2E \frac{b^\nu}{\Gamma(\nu)} I_0(2AE) \int_0^\infty x^{\nu-2} \exp(-(b + A^2)x) \exp\left(-\frac{E^2}{x}\right) dx \quad (22)$$

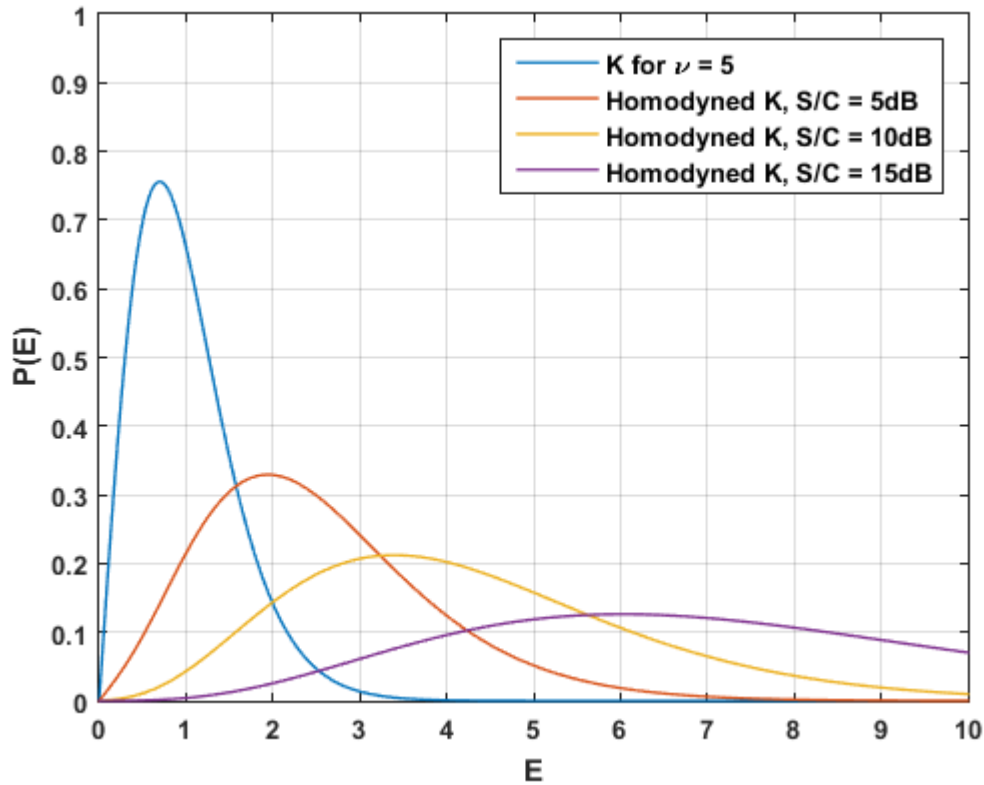


Figure-13: K distributed clutter and homodyned K process for different signal-to-clutter ratio.

In conclusion, compound clutter model has two parts: speckle model  $P(z|x)$  with short decorrelation time and modulation model  $x$  with large decorrelation time. For detail description of sea clutter see [16].

#### 2.5.4.6 Rain Clutter Model

Rain can effect radar detection performance in two ways – attenuation of radar signal reflected from target, reflected echoes from rain (clutter). Radar signal attenuation depends on rainfall rate, radar operating frequency and polarization. According to the concept of underwater communication, high frequency signal attenuate rapidly in rain. As mentioned earlier, ships have to use 9GHz radar set (>1m antenna aperture, 0.66 dB/km signal attenuation in heavy rain) and are encouraged to use 3GHz radar as second set (>3m antenna aperture, 0.019 dB/km signal attenuation in heavy rain).

Rain clutter is volume clutter. The amount of clutter is proportional to the volume of rain illuminated by radar beam. Thus, the narrower the azimuth and elevation beamwidths the less the rain clutter. Rain clutter can also be reduced by 20dB using circular polarization. As because radar cross section is reduced for circular polarization, radar should be switched to linear polarization during normal environment to ensure optimal operation. Fourier filter bank based on Doppler frequency, slope based filter and discrete wavelet transform are few familiar techniques for removing rain clutter [17, 18].

### 2.5.4.7 Slow Moving Clutter Rejection

If a radar detects only moving targets, it is easier to reject slow moving clutter. There are two different methods of removing slow moving clutter in this type of radar- Moving Target Indicator (MTI) techniques and Pulsed Doppler techniques. In MTI techniques, slow moving clutter are rejected with low pass Doppler filter. MTI canceller is used in this technique. In Pulsed Doppler techniques Doppler filter bank is used for removing slow moving clutter and measuring the Doppler frequency. Moving Target Detector clutter map technique is used to detect slow speed targets where backscatter signal power is greater than clutter power.

### 2.5.5 General Purpose Computer

General purpose computer is used for detecting, thresholding, parameter estimation and tracking. Considering equation (17) for simple clutter model or (19) for compound clutter model, if threshold is  $Y$ , probability of false alarm is given by

$$P_{FA}(Y) = \int_Y^{\infty} P_C(z) dz, \quad (23)$$

where  $P_{FA}$  is probability of false alarm;  $P_C(z)$  is similar to  $P(z)$  in (17) and (19),  $C$  stands for clutter.

Similarly, Considering equation (15) for simple clutter model including signal from target or (21) for compound clutter model including signal from target, if threshold is  $Y$ , probability of detection is given by

$$P_D(Y) = \int_Y^{\infty} P_S(z) dz, \quad (24)$$

where  $P_D$  is probability of detection;  $P_S(z)$  is similar to  $P(z)$  in (15) and (21),  $s$  stands for signal from target and clutter.

In equation (23), false alarm rate is determined by considering only single pulse. Setting Constant false alarm rate (CFAR) is the first step of detection process. In [16], after pulse to pulse integration a threshold is applied and after scan to scan integration threshold is adjusted using a CFAR system for a specified false alarm rate. For pulse to pulse integration correlation properties are important. Only compound model of sea clutter is needed to be considered for modelling the partial correlation of frequency agile sea clutter. The compound model of sea clutter is given in equation (19). Probability of clutter power in noise for one pulse can be written as

$$P(z_1|x) = \frac{1}{x + P_n} \exp\left(-\frac{z_1}{x + P_n}\right),$$

where  $P_n$  is the noise power,  $x$  is constant within the dwell time of scanning radar. Now, considering integration of  $N$  pulses,  $z = z_1 + z_2 + \dots + z_N$ , probability of clutter power in noise for  $N$  pulses,

$$P(z|x) = P(z_1|x) * P(z_2|x) * P(z_3|x) * \dots * P(z_N|x),$$

can be solved by using properties of characteristics function. Derived equation is

$$P(z|x) = \frac{z^{N-1}}{(x + P_n)^N (N-1)!} \exp\left(-\frac{z}{x + P_n}\right)$$

Probability of false alarm for threshold  $Y$  is

$$P_{FA}(Y|x) = \int_Y^{\infty} P(z|x) dz = \frac{\Gamma\left(N, \frac{Y}{x + P_n}\right)}{(N-1)!}$$

Hence, from probability theory,  $P_{FA}(Y)$  can be calculated as

$$P_{FA}(Y) = \frac{1}{(N-1)!} \int_0^{\infty} \Gamma\left(N, \frac{Y}{x + P_n}\right) P(x) dx, \quad (25)$$

where  $P(x)$  is gamma distributed which is explained in previous section. Equation (25) is computationally easy to solve numerically.

For high resolution radar, greater fluctuation in sea clutter is observed by the radar. This fluctuation in sea clutter, or sea spike, can be modelled using Swerling type 1 target model, special cases of the Chi-Squared model. Hence, this is mixture of K distribution model and Swerling type 1 target model, which is called KA model.

In [16], binary scan-to-scan integration is explained. For  $m$  out of  $n$  scan-to-scan integration, the probability of CFAR is derived as

$$P_{FA}^{s-s} = \sum_{i=m}^n \frac{n!}{(n-i)! i!} P_{FA}^i(Y) (1 - P_{FA}(Y))^{n-i} \quad (26)$$

Equation (25) and (26) are used to calculate threshold value for a specific CFAR if certain parameter (clutter-to-noise ratio, signal-to-noise ratio, shape parameter etc.) are known. When these parameters are not known, parameter estimation is needed.

From equation (16) and (23) probability of false alarm is

$$P_{FA} = \exp\left(-\frac{Y^2}{x}\right)$$

or,

$$Y^2 = x \log_e(P_{FA}) \quad (27)$$

Radar should be able to estimate  $x$  to solve the above equation for  $Y$ . In unknown amplitude of clutter,  $x$  needs to be estimated adaptively. First step of the estimation of  $x$  is to control the gain of the receiver for keeping the received signal level within the receiver signal dynamic range. Then, a threshold is set using cell averaging CFAR system, where estimation of mean level of interference, noise plus clutter, is required.

Methods used for receiver gain control are Sensitivity Time Control (STC) and Automatic Gain Control (AGC)/ Instantaneous Automatic Gain Control (IAGC). Any one or combination of the methods may be used for this purpose. Received signal power from any object depends on range and bearing of the object. So, time dependent amplifier gain should be adjusted to remove the dependence of range on received signal power. Sensitivity Time Control circuit is used during a single pulse repetition time to adjust this gain. If the radar is not range ambiguous, STC is very useful for clutter rejection. A combined STC curve can be drawn considering the attenuation for range, sea, rain and minimum SNR and subtracted from the received signal. AGC is used to control the gain by using local signal level. This is a closed loop control system which depends on range and bearing. It adjusts the receiver sensitivity for the best signal reception in large variation of signal amplitude. Another method used in earlier radar is Log FTC receiver for Rayleigh distributed clutter. In this receiver logarithmic video amplifier is used for getting clutter power independent output with constant variance. This output is differentiated by First Time Constant (FTC) circuit for removing slowly varying clutter.

Cell-averaging CFAR detector is used for estimating expected mean level of the clutter in the cell under test. Figure-14 shows a double sided Cell-averaging CFAR detector. In this technique, keeping a guard band of  $2G$  number of cells near the cell under test, signal return from  $2M$  number of cells are averaged for estimating the mean level of clutter. Multiplication factor  $\alpha$  depends on the clutter amplitude statistics and specific probability of CFAR.

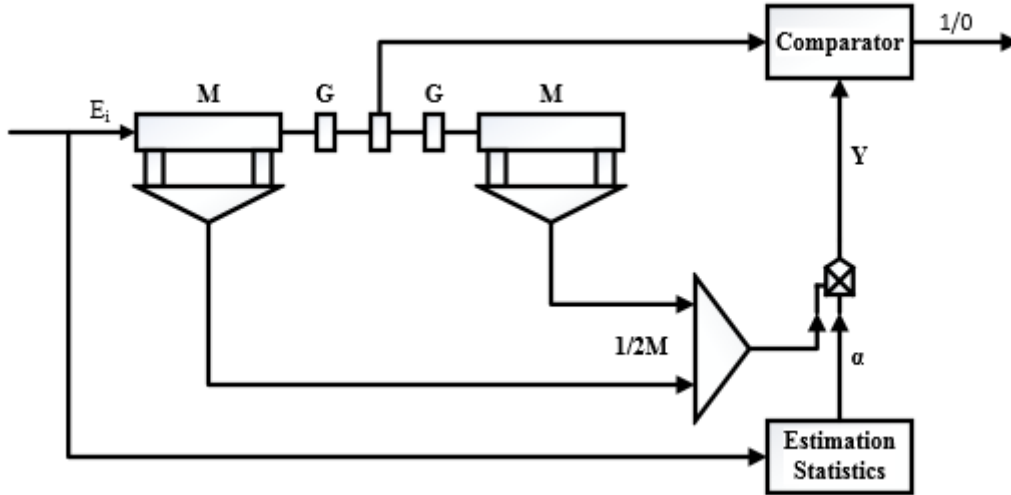


Figure-14: Double sided Cell-averaging CFAR detector.

Detail description on estimation statistics and different variation in Cell-averaging CFAR detector can be found in [16]. CFAR technique for spatially correlated K distributed clutter is presented in [23].

### 2.5.6 Radar Display

Radar display produce map like image. There are different types of radar display: A-scope, B-scope, PPI-scope, RHI-scope, Raster scan monitor. A-scope display shows the range and relative strength of the target. B-scope is a 2 dimensional diagram, where horizontal axis represents azimuth angle and vertical axis represents range of target. Plan position indicator (PPI) scope is most used radar display. It is a polar coordinate display where radar own position is indicated in center of the display and targets surrounding to the radar is plotted according to range, azimuth and strength of the received signal from the target. The range-height indicator (RHI) scope shows range and height of the target 2 dimensional diagram. Raster scan monitor shows range, azimuth angle, elevation angle and other information of the target.

### 2.6 Using FMCW Ship Radar for Low Altitude Airspace Monitoring

An unmodulated continuous wave radar continuously transmits signal. This can measure velocity of object by measuring Doppler frequency shift. For calculating velocity, equation (11) can be simplified as follows

$$v = \frac{\lambda f_d}{2} \quad (28)$$

But, this radar cannot measure distance of an object because of missing of time reference. In contrast, frequency modulated continuous wave (FMCW) radar can always measure the range of an object. Velocity measurement of the object depends on modulation technique used. For sawtooth modulation technique, see section 2.5.4.4, Doppler frequency shift cannot be separated from the frequency shift due to range, equation (13) is used for distance measurement, presented here again

$$R = \frac{c \Delta f T}{2B} \quad (29)$$

This modulation technique is usually used in ship radar for large range measurement and negligible Doppler frequency shift. It is explained in section 2.5.4.3 that, for relative velocity 10 m/s, Doppler shift is negligible compared to the resolution of ship radar signal processor. But, for relative velocity 200 m/s, Doppler shift is big enough to measure even negative distances. Using triangular modulation technique, both range and Doppler frequency shift can be measured [24]. Here, we have both rising and

falling edge of frequency. Frequency difference due to range is the average of frequency difference during rising and falling edge and Doppler frequency shift is the half of the difference of frequency difference during rising and falling edge.

$$f_m = \frac{\Delta f_1 + \Delta f_2}{2} \quad (30)$$

$$f_d = \frac{|\Delta f_1 - \Delta f_2|}{2} \quad (31)$$

where,  $\Delta f_1$  is frequency difference during rising edge,  $\Delta f_2$  is frequency difference during falling edge,  $f_m$  is frequency difference due to range,  $f_d$  is Doppler frequency shift. In this technique, if wrong Doppler frequency is assigned to a destination it can lead to ghost target. Thus, extra effort is needed to resolve this problem [25].

Existing FMCW ship radar uses sawtooth modulation technique and scan-to-scan integration. For high speed objects, we see that sawtooth modulation technique introduces big range measurement errors and scan-to-scan integration can remove high speed objects from the radar display. Perhaps there are some other manufacturer specific settings which will also remove high speed objects from the radar display. In spite of having these limitations, it would be possible to detect moderate speed vehicles with some changes in radar signal processing. Further analysis is needed to exactly determine the speed limit of the objects.

## 3. Other Sensors

### 3.1 Introduction

In this chapter, a basic description of global navigation satellite system (GNSS), automatic dependent surveillance-broadcast (ADS-B), and automatic identification system (AIS) is given. These three sensors are proposed to be used along with ship radar, for operation of UAV in low altitude airspace in sea and to implement the electronic map for simultaneous operation with air and sea.

### 3.2 Global Navigation Satellite System (GNSS)

Global navigation satellite system (GNSS) is used for positioning in land, air and offshore. Present operational GNSSs are United States GPS and Russian GLONASS. GNSS receiver provides position and time information anywhere in the globe if four or more GNSS satellites are in line of site of the receiver. To improve the precision of position accuracy local or global augmentation data is used. In general, GPS uses three types of signal- code, message, and carrier. For civilian use, GPS encode 50 bps message with 1.023 Mbps C/A code using modulo 2 addition and modulate the encoded code using L1 carrier of 1575.42 MHz and transmit the modulated carrier from GPS satellite. Users receive the modulated carrier using GPS receiver, demodulate it using L1 carrier, correlate user generated code with received code to calculate receiving time and find time of arrival (TOA) from difference of calculated receiving time and transmitted time available in GPS message. Distance between GPS satellite and GPS receiver is measured by multiplying the velocity of light with TOA. For military use, GPS encode 50 bps message with 10.23 Mbps P(Y) code using modulo 2 addition and modulate the encoded code using L1 carrier of 1575.42 MHz as well as L2 carrier of 1227.6 MHz and transmit both modulated carrier from GPS satellite. Thus, military users can measure the local ionosphere delay as they have access of GPS data in two different carrier frequency.

Distance measurement is subject to large error because of following reasons - i) solar activity dependent delay in code observation and advance in carrier observation in ionosphere (error 5m-20m), ii) satellite elevation angle dependent carrier and code observation delay in troposphere (error 2.5m-15m), iii) receiver measurement noise (error .5m), iv) imperfection in satellite clock correction parameters sent from satellite (error 1.5m), v) imperfection in orbital parameter sent from satellite (error 1.5m), vi) multipath propagation (error 1m-5m), v) geophysical effect (0.5m). Different methods are available to reduce the measurement error by providing augmentation data such Differential GPS, Wide Area GPS, Real Time Kinematics (RTK), Post Processed Positioning and Precise Point Positioning (PPP). Some GPS augmentation service providers are commercial supplier, Marine Radio Beacon and Free-to-Air Satellite Based Augmentation Systems [26].

### 3.3 Automatic Dependent Surveillance-Broadcast (ADS-B)

Automatic dependent surveillance-broadcast (ADS-B) is a new surveillance technology used for sharing aircraft information (position, velocity, heading, altitude, aircraft identification etc.) with other aircrafts and ADS-B ground stations. Aircraft receives its position data from global navigation satellite system and continuously broadcasts all information, including position information, using ADS-B Out. ADS -B In is used to receive the broadcasted information by other aircrafts. When ADS -B In is in the range of ADS-B ground stations, it can also see the weather radar information and same air traffic picture what ADS-B ground stations see.

ADS-B Out needs an approved position source. This position data should be transmitted using mode S transponder with "Extended Squitter" technology having 1090 MHz data link in all over the world except USA. The technique must also be used with in class A airspace, above 18000 ft, in USA. Inside USA, if aircrafts fly below 18000 ft, it is also possible to use Universal Access Transceiver (UAT). UAT broadcast ADS-B Out data using 978 MHz data link. Dual link UAT can receive ADS-B In information from both type of ADS-B Out device.

ADS-B is a line-of-sight technology. So, maximum range of ADS-B depends on atmospheric conditions and obstacles. ADS-B Technologies introduce a variation of ADS-B called ADS-B Link Augmentation System (ALAS). ALAS is a space based ADS-B used for minimizing line-of-sight loss for obstacles. With the normal operation of ADS-B, it can detect large obstacles from reflected signal. If it detects an obstacle, it will send the information to air traffic control automation center by using reliable satellite link.

Majority of aircrafts have to use ADS-B in United State airspace by January, 2020 and planes having weight above 12600lb or cruise above 250 knots will need ADS-B to operate in European airspace by 2017 [27].

### **3.4 Automatic Identification System (AIS)**

Automatic identification system (AIS) is used by vessels and vessel traffic services for automatic tracking of vessels. According to requirement of International Convention for Safety of Life at Sea all vessels with 300 gross tonnage or above and all passenger ships need to use Class A AIS. Class B AIS is introduced for lighter commercial and leisure vessels which is not mandatory to use and has less functionality compared to Class A. Class C AIS is low cost receive only device.

Class A AIS transmitter uses one of the two available VHF radio channels 87B (161.975MHz) and 88B (162.025MHz) for transmitting own information such as position, position accuracy, speed, heading, bearing, navigational status, UTC seconds, nine digit MMSI identification number, seven digit IMO ship identification number, rate of turn, destination name, estimated time of arrival, draught of ship, position source type, radio call sign etc. It can receive signal from other AIS in both frequency band using two VHF receivers. Transceiver uses self-organized time division multiple access (SOTDMA) and transmits signal at maximum power 12.5W. SOTDMA assigns time slot without using central station and time synchronization is done by Coordinated Universal Time. Over 12.5 KHz or 25 KHz channel it use 9600 bps GMSK modulation using HDLC packet protocol. It also has one VHF DSC receiver. GNSS or Inertial Navigation System is used as position source. An internal position source is also available as backup. Moving vessels update AIS information within 2-10 seconds depending on speed of the vessels - fast moving vessels update interval is small. Anchored vessels update their information every 3 minutes.

Class B AIS is almost similar to Class A with less functionalities. In Class B, two receivers use Carrier Sense Time Division Multiple Access (CSTDMA) while Class A receivers use TDMA. It uses similar VHF channels for transmitter, VHF DSC receiver and position source as Class As. However, it transmits signal at maximum power 2W, information update time for vessels with speed greater than 2 knots is 30 seconds and 3 minutes otherwise [28].

## 4. Flyable Path Generation and Collision Avoidance

### 4.1 Introduction

This chapter describes flyable path generation and collision avoidance of an unmanned aerial vehicle (UAV) in 2D and 3D environment. Before starting the mission, path planning and collision avoidance algorithm is used for choosing a flyable path from an initial pose (position and angle) to a final pose considering mapped static obstacles. A path is flyable if UAV can manoeuvre properly obeying motion constraints. During flight, the airspace is continuously monitored for any types of unmapped static and dynamic obstacles. If any obstacle is detected, the collision avoidance algorithm is used to avoid the obstacle and modify the path for safety. Figure 1 shows the functional architecture of the mission planner. Layer 1 is decision maker and used for tracking the objectives of the mission. It allocates tasks, e.g. waypoints, to layer 2. Layer 2 is used for path planning and collision avoidance of UAV according to the allocated task. Layer 3 is in the UAV on-board used for guidance and control of UAV, taking input from layer 2. For our application, processors and sensors for layer 1 and layer 2 are situated in the ship, ground station. It makes the UAV lighter and these processors can be used for more than one UAV. Thus, layer 3 shares data, e.g. position and velocity information of UAV and input from layer 2, through wireless communication.

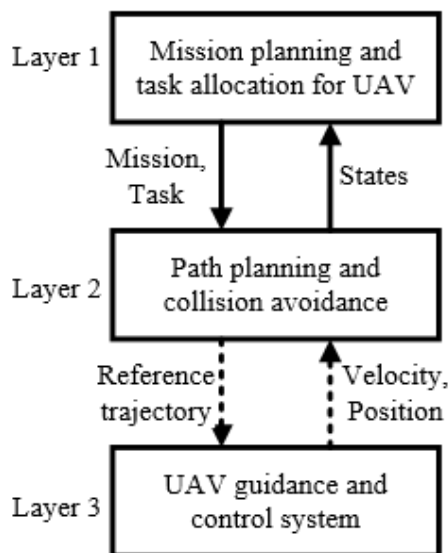


Figure-1: Functional architecture of the mission planner

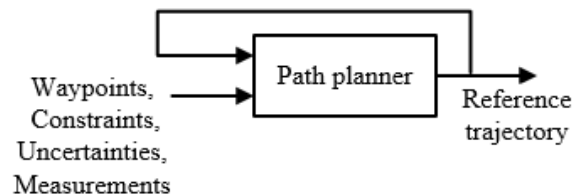


Figure-2: Path planner block diagram [8]

Figure 2 shows the formulation block diagram of the path planner. It is a feedback system and takes waypoints, constraints, uncertainties, and measurements as input.

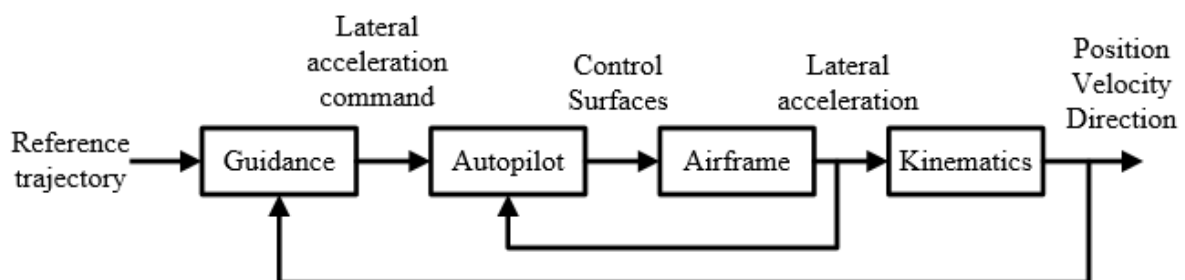


Figure-3: Autopilot and guidance control loop [8]

Figure 3 shows the autopilot and guidance control loop of UAV, where inner loop is autopilot and outer loop is guidance system. In case of fixed wing UAV, guidance system generate lateral acceleration command and autopilot control ailerons, elevator, and rudder to achieve the acceleration.

A brief description of autopilot systems for small UAV is presented in [29]. Small UAV may have three types of control mode: remote control, autopilot control and mixed control. For remote control mode, an expert human operator is needed. Thus, autopilot mode is more reliable for guidance of small UAV. Autopilot is used during flight to guide UAV without any assistance from human operator. It assists some or all of the following tasks of UAV: take off, trajectory following, ascent, descent, and landing. Autopilot may take input from UAV ground station, satellite, on-board sensors, and remote control device and send output to the servo motors. Autopilot has two functions: state estimation and control input generation based on reference trajectory and estimated states. State estimator takes input from GPS and inertial navigation sensors (e.g. magnetic, infrared, pressure, ultrasonic, sonar, vision, rate gyro, and acceleration). GPS has slow update frequency, usually 1 Hz, but required update frequency should be larger, usually 25 Hz. An estimation algorithm, e.g. Kalman filtering, is used to increase the update speed by using data from inertial navigation sensors, by calculating optimal value of position between two update from GPS. Two basic controllers inside autopilot are altitude controller, and velocity and heading controller. Different control strategies (e.g. PID, Fuzzy logic based, Neural network based,  $H\infty$ ) are used for controller part of autopilot.

## 4.2 Flyable Path Generation in 2D

### 4.2.1 Problem Formulation

For simple 2D flyable path generation from a start pose to a final pose, we consider that there is no obstacles in the scenario. Start pose and final pose of UAV can be represented by  $P_s(x_s, y_s, \varphi_s)$  and  $P_f(x_f, y_f, \varphi_f)$  respectively, where  $\varphi_s$  and  $\varphi_f$  are heading angles measured counter-clockwise from x-axis. For calculating the shortest flyable path, the problem can be mathematically defined as

$$P_s(x_s, y_s, \varphi_s) \xrightarrow{\mathbf{r}(t)} P_f(x_f, y_f, \varphi_f),$$

where  $t$  is the path parameter and  $\mathbf{r}(t)$  is the shortest flyable path. Dubins path is a shortest path between two poses which obeys curvature constraint  $|\kappa| \leq \kappa_{max}$ . This path is not flyable because its curvature is discontinuous at the joining point of constant curvature segment and straight line segment. To make the path flyable, Clothoid path approach or Pythagorean hodograph approach might be used.

### 4.2.2 Dubins Path Generation using Analytical Geometry

Dubins path is the shortest path between two poses. In this section, four different Dubins path between two poses  $P_s(x_s, y_s, \varphi_s)$  and  $P_f(x_f, y_f, \varphi_f)$  are generated using analytical geometry by obeying maximum start pose curvature  $\kappa_s = 1/r_s$  and finish pose curvature  $\kappa_f = 1/r_f$ . Figure 4 and Figure 5 are external tangent Dubins path generated by right-to-right and left-to-left turn and Figure 6 and Figure 7 are internal tangent Dubins path generated by right-to-left and left-to-right turn respectively. Shortest path is the minimum distance path among these four paths.

**Right-to-right turn:** Figure 4 shows the Dubins path generated by right-to-right turn. From the start position, UAV turns to the right, clockwise, by angle  $\theta_s$  with constant curvature  $\kappa_s$ . Then, it flies straight followed by another right angle turn  $\theta_f$  with constant curvature  $\kappa_f$ . Start tangent circle center  $P_{cs}(x_{cs}, y_{cs})$  and finish tangent circle center  $P_{cf}(x_{cf}, y_{cf})$  can be calculated from given start and finish pose using

$$\begin{aligned}
x_{cs} &= x_s - \frac{1}{\kappa_s} \cos(\varphi_s + \frac{\pi}{2}) \\
y_{cs} &= y_s - \frac{1}{\kappa_s} \sin(\varphi_s + \frac{\pi}{2}) \\
x_{cf} &= x_f - \frac{1}{\kappa_f} \cos(\varphi_f + \frac{\pi}{2}) \\
y_{cf} &= y_f - \frac{1}{\kappa_f} \sin(\varphi_f + \frac{\pi}{2})
\end{aligned}$$

and the slope of the center line  $P_{cs}P_{cf}$  can be calculated using

$$\beta = \tan^{-1} \frac{y_{cf} - y_{cs}}{x_{cf} - x_{cs}}$$

An inner circle with radius  $(1/\kappa_f - 1/\kappa_s)$  is drawn at finish tangent circle center, given that  $1/\kappa_f > 1/\kappa_s$ .  $P_{cs}P_T$  is the tangent of the inner circle; hence,  $P_T P_{cf}$  is the perpendicular on  $P_{cs}P_T$ . Line  $P_{cs}P_{Ns}$  is drawn parallel to  $P_T P_{Nf}$ . Now, the angle between lines  $P_{cs}P_T$  and  $P_{cs}P_{cf}$  can be calculated using

$$\alpha = \sin^{-1} \frac{\frac{1}{\kappa_f} - \frac{1}{\kappa_s}}{c},$$

where  $c$  is the length of line  $P_{cs}P_{cf}$ .

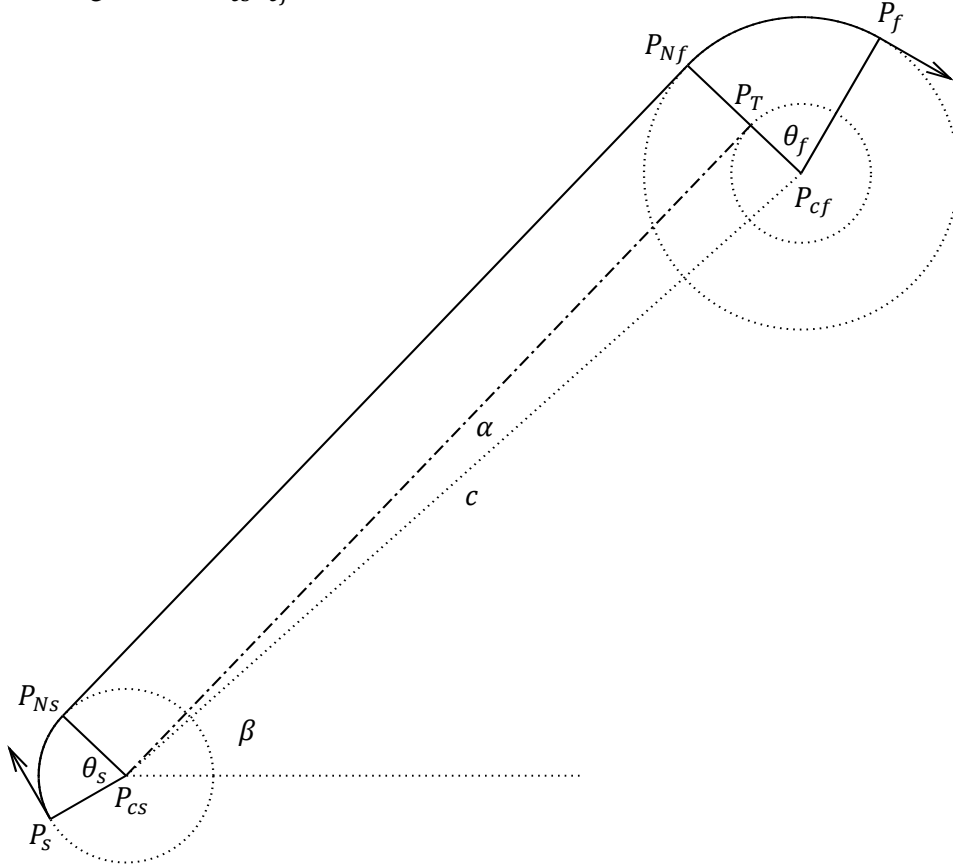


Figure-4: Dubins path for right-to-right turn ( $\varphi_s = 120^\circ$ ,  $\varphi_f = 330^\circ$ )

Tangent exit point  $P_{Ns}(x_{Ns}, y_{Ns})$  and entry point  $P_{Nf}(x_{Nf}, y_{Nf})$  can be calculated using

$$\begin{aligned}
x_{Ns} &= x_{cs} + \frac{1}{\kappa_s} \cos(\varphi_{start}) \\
y_{Ns} &= y_{cs} + \frac{1}{\kappa_s} \sin(\varphi_{start})
\end{aligned}$$

$$x_{Nf} = x_{cf} + \frac{1}{\kappa_f} \cos(\varphi_{finish})$$

$$y_{Nf} = y_{cf} + \frac{1}{\kappa_f} \sin(\varphi_{finish})$$

Here,

$$\varphi_{start} = \beta + \alpha + \frac{\pi}{2}$$

$$\varphi_{finish} = \beta + \alpha + \frac{\pi}{2}$$

**Left-to-left turn:** Figure 5 shows the Dubins path generated by left-to-left turn. From the start position, UAV turns to the left, counter clockwise, by angle  $\theta_s$  with constant curvature  $\kappa_s$ . Then, it flies straight followed by another left angle turn  $\theta_f$  with constant curvature  $\kappa_f$ . Start tangent circle center  $P_{cs}(x_{cs}, y_{cs})$  and finish tangent circle center  $P_{cf}(x_{cf}, y_{cf})$  can be calculated from given start and finish pose using

$$x_{cs} = x_s - \frac{1}{\kappa_s} \cos(\varphi_s - \frac{\pi}{2})$$

$$y_{cs} = y_s - \frac{1}{\kappa_s} \sin(\varphi_s - \frac{\pi}{2})$$

$$x_{cf} = x_f - \frac{1}{\kappa_f} \cos(\varphi_f - \frac{\pi}{2})$$

$$y_{cf} = y_f - \frac{1}{\kappa_f} \sin(\varphi_f - \frac{\pi}{2})$$

and slope of the center line  $P_{cs}P_{cf}$  can be calculated using

$$\beta = \tan^{-1} \frac{y_{cf} - y_{cs}}{x_{cf} - x_{cs}}$$

An inner circle with radius  $(1/\kappa_f - 1/\kappa_s)$  is drawn at finish tangent circle center, given that  $1/\kappa_f > 1/\kappa_s$ .  $P_{cs}P_T$  is the tangent of the inner circle; hence,  $P_T P_{cf}$  is the perpendicular on  $P_{cs}P_T$ . Line  $P_{cs}P_{Ns}$  is drawn parallel to  $P_T P_{Nf}$ . Now, angle between lines  $P_{cs}P_T$  and  $P_{cs}P_{cf}$  can be calculated using

$$\alpha = \sin^{-1} \frac{\frac{1}{\kappa_f} - \frac{1}{\kappa_s}}{c}$$

Tangent exit point  $P_{Ns}(x_{Ns}, y_{Ns})$  and entry point  $P_{Nf}(x_{Nf}, y_{Nf})$  can be calculated using

$$x_{Ns} = x_{cs} + \frac{1}{\kappa_s} \cos(\varphi_{start})$$

$$y_{Ns} = y_{cs} + \frac{1}{\kappa_s} \sin(\varphi_{start})$$

$$x_{Nf} = x_{cf} + \frac{1}{\kappa_f} \cos(\varphi_{finish})$$

$$y_{Nf} = y_{cf} + \frac{1}{\kappa_f} \sin(\varphi_{finish})$$

Here,

$$\varphi_{start} = \beta - \alpha + 3\frac{\pi}{2}$$

$$\varphi_{finish} = \beta - \alpha + 3\frac{\pi}{2}$$

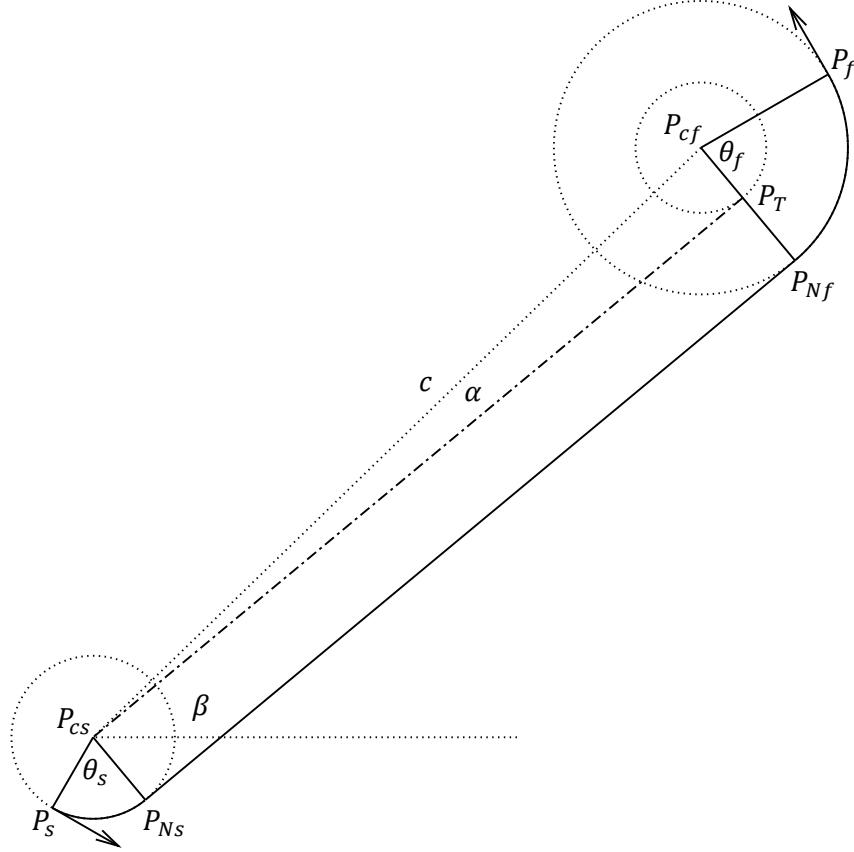


Figure-5: Dubins path for left-to-left turn ( $\varphi_s = 330^\circ$ ,  $\varphi_f = 120^\circ$ )

**Right-to-left turn:** Figure 6 shows the Dubins path generated by right-to-left turn. From the start position, UAV turns to the right, clockwise, by angle  $\theta_s$  with constant curvature  $\kappa_s$ . Then, it flies straight followed by another left angle turn  $\theta_f$  with constant curvature  $\kappa_f$ . Start tangent circle center  $P_{cs}(x_{cs}, y_{cs})$  and finish tangent circle center  $P_{cf}(x_{cf}, y_{cf})$  can be calculated from given start and finish pose using

$$\begin{aligned} x_{cs} &= x_s - \frac{1}{\kappa_s} \cos(\varphi_s + \frac{\pi}{2}) \\ y_{cs} &= y_s - \frac{1}{\kappa_s} \sin(\varphi_s + \frac{\pi}{2}) \\ x_{cf} &= x_f - \frac{1}{\kappa_f} \cos(\varphi_f - \frac{\pi}{2}) \\ y_{cf} &= y_f - \frac{1}{\kappa_f} \sin(\varphi_f - \frac{\pi}{2}) \end{aligned}$$

and slope of the center line  $P_{cs}P_{cf}$  can be calculated using

$$\beta = \tan^{-1} \frac{y_{cf} - y_{cs}}{x_{cf} - x_{cs}}$$

An outer circle with radius  $(1/\kappa_f + 1/\kappa_s)$  is drawn at finish tangent circle center.  $P_{cs}P_T$  is the tangent of the outer circle; hence,  $P_T P_{cf}$  is the perpendicular on  $P_{cs}P_T$ . Line  $P_{cs}P_{Ns}$  is drawn parallel to  $P_T P_{Nf}$ . Now, angle between lines  $P_{cs}P_T$  and  $P_{cs}P_{cf}$  can be calculated using

$$\alpha = \sin^{-1} \frac{\frac{1}{\kappa_f} + \frac{1}{\kappa_s}}{c}$$

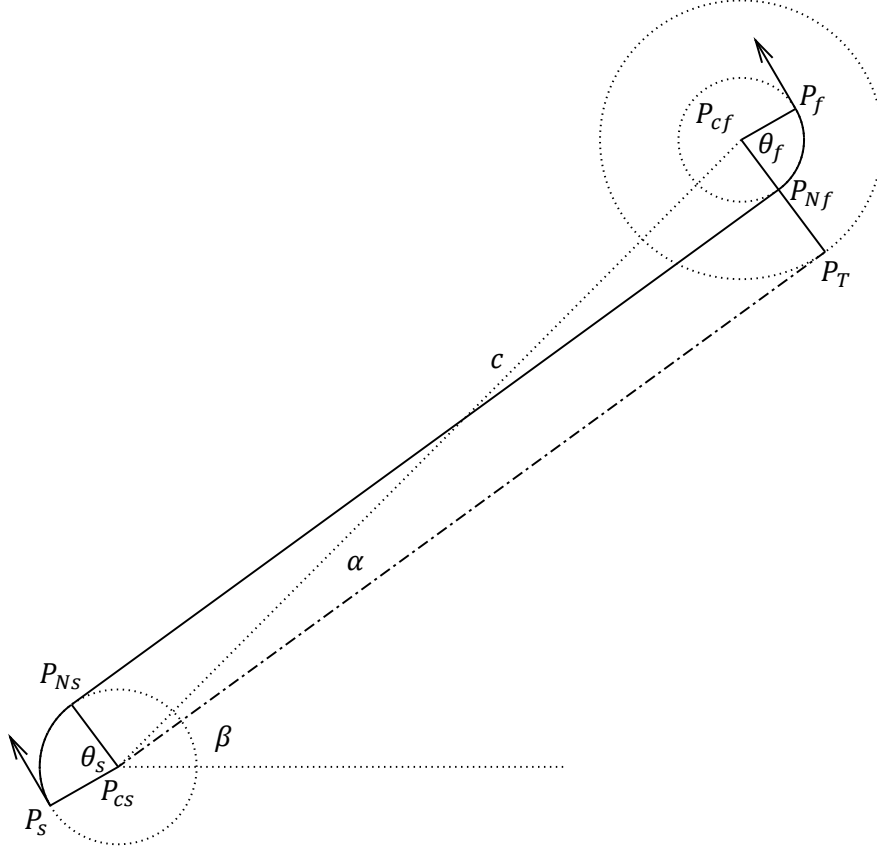


Figure-6: Dubins path for right-to-left turn ( $\varphi_s = 120^\circ, \varphi_f = 120^\circ$ )

Tangent exit point  $P_{Ns}(x_{Ns}, y_{Ns})$  and entry point  $P_{Nf}(x_{Nf}, y_{Nf})$  can be calculated using

$$\begin{aligned} x_{Ns} &= x_{cs} + \frac{1}{\kappa_s} \cos(\varphi_{start}) \\ y_{Ns} &= y_{cs} + \frac{1}{\kappa_s} \sin(\varphi_{start}) \\ x_{Nf} &= x_{cf} + \frac{1}{\kappa_f} \cos(\varphi_{finish}) \\ y_{Nf} &= y_{cf} + \frac{1}{\kappa_f} \sin(\varphi_{finish}) \end{aligned}$$

Here,

$$\begin{aligned} \varphi_{start} &= \beta - \alpha + \frac{\pi}{2} \\ \varphi_{finish} &= \beta - \alpha + 3\frac{\pi}{2} \end{aligned}$$

**Left-to-right turn:** Figure 7 shows the Dubins path generated by left-to-right turn. From the start position, UAV turns to the left, counter clockwise, by angle  $\theta_s$  with constant curvature  $\kappa_s$ . Then, it flies straight followed by another right angle turn  $\theta_f$  with constant curvature  $\kappa_f$ . Start tangent circle center  $P_{cs}(x_{cs}, y_{cs})$  and finish tangent circle center  $P_{cf}(x_{cf}, y_{cf})$  can be calculated from given start and finish pose using

$$x_{cs} = x_s - \frac{1}{\kappa_s} \cos(\varphi_s - \frac{\pi}{2})$$

$$y_{cs} = y_s - \frac{1}{\kappa_s} \sin(\varphi_s - \frac{\pi}{2})$$

$$x_{cf} = x_f - \frac{1}{\kappa_f} \cos(\varphi_f + \frac{\pi}{2})$$

$$y_{cf} = y_f - \frac{1}{\kappa_f} \sin(\varphi_f + \frac{\pi}{2})$$

and slope of the center line  $P_{cs}P_{cf}$  can be calculated using

$$\beta = \tan^{-1} \frac{y_{cf} - y_{cs}}{x_{cf} - x_{cs}}$$

An outer circle with radius  $(1/\kappa_f + 1/\kappa_s)$  is drawn at finish tangent circle center.  $P_{cs}P_T$  is the tangent of the outer circle; hence,  $P_T P_{cf}$  is the perpendicular on  $P_{cs}P_T$ . Line  $P_{cs}P_{Ns}$  is drawn parallel to  $P_T P_{Nf}$ . Now, angle between lines  $P_{cs}P_T$  and  $P_{cs}P_{cf}$  can be calculated using

$$\alpha = \sin^{-1} \frac{\frac{1}{\kappa_f} + \frac{1}{\kappa_s}}{c}$$

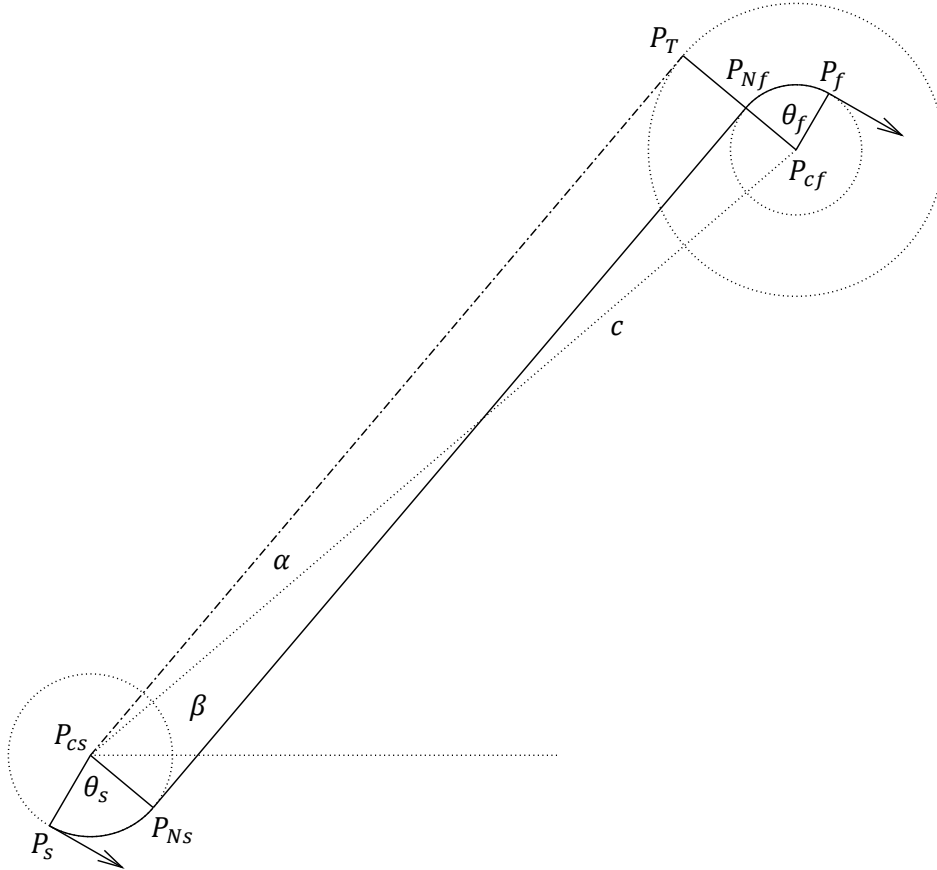


Figure-7: Dubins path for left-to-right turn ( $\varphi_s = 330^\circ, \varphi_f = 330^\circ$ )

Tangent exit point  $P_{Ns}(x_{Ns}, y_{Ns})$  and entry point  $P_{Nf}(x_{Nf}, y_{Nf})$  can be calculated using

$$x_{Ns} = x_{cs} + \frac{1}{\kappa_s} \cos(\varphi_{start})$$

$$y_{Ns} = y_{cs} + \frac{1}{\kappa_s} \sin(\varphi_{start})$$

$$x_{Nf} = x_{cf} + \frac{1}{\kappa_f} \cos(\varphi_{finish})$$

$$y_{Nf} = y_{cf} + \frac{1}{\kappa_f} \sin(\varphi_{finish})$$

Here

$$\varphi_{start} = \beta + \alpha + 3\frac{\pi}{2}$$

$$\varphi_{finish} = \beta + \alpha + \frac{\pi}{2}$$

$P_s, P_f, P_{cs}, P_{cf}, P_{Ns}$  and  $P_{Nf}$  are known; therefore, initial rotation angle  $\theta_s$ , final rotation angle  $\theta_f$ , and distance between  $P_{Ns}$  and  $P_{Nf}$  can be calculated. If distance between  $P_{Ns}$  and  $P_{Nf}$  is  $a$ , the path length is given by

$$\text{Path length} = \frac{\theta_s}{\kappa_s} + a + \frac{\theta_f}{\kappa_f}$$

**Example:** For start pose  $P_s(5,10,10^\circ)$  and finish pose  $P_f(100,100,70^\circ)$  four possible Dubins paths are simulated. Figure 8 shows that shortest path is the Dubins path for left-left turn.

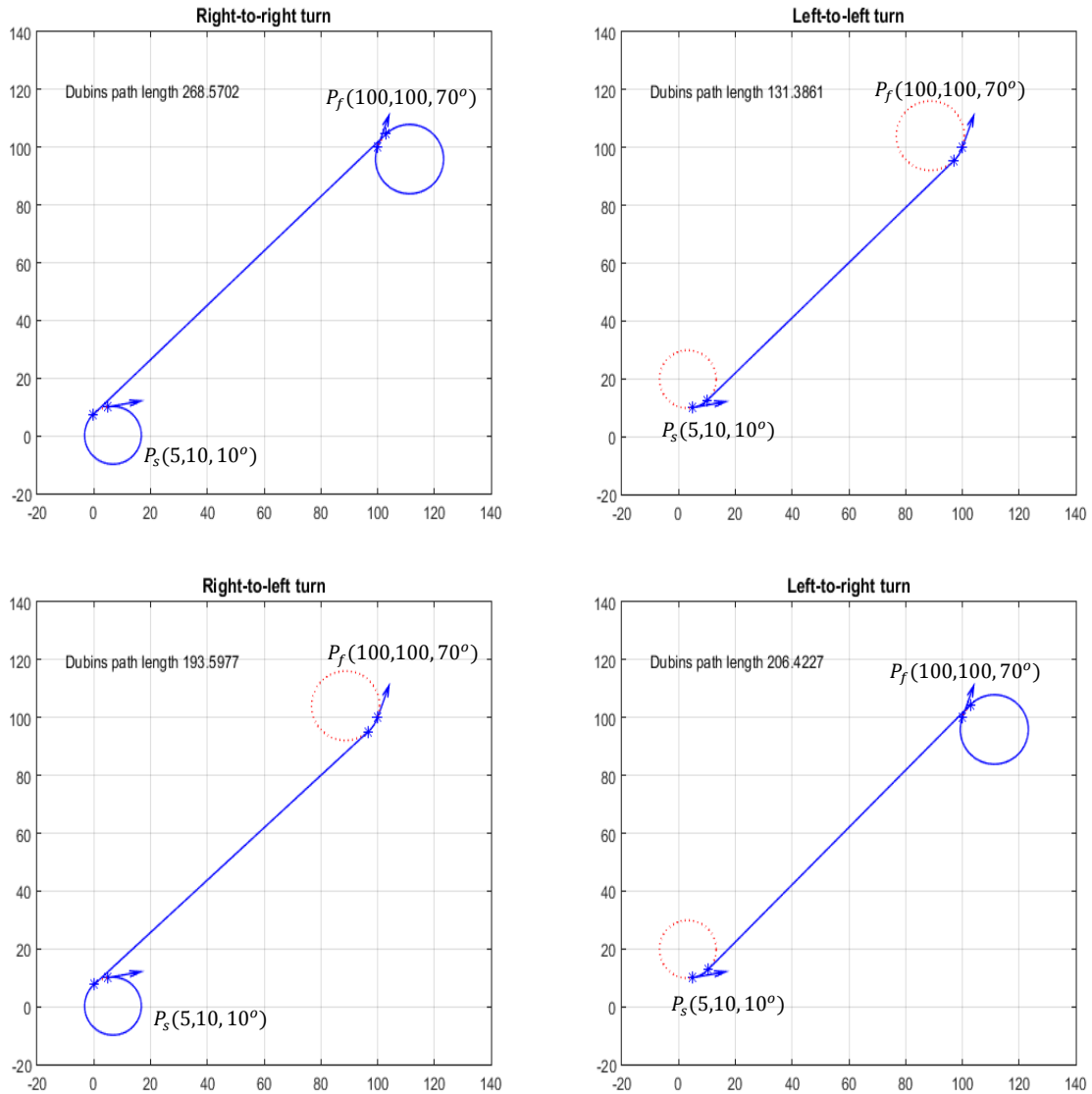


Figure-8: Four possible Dubins path for start pose  $P_s(5,10,10^\circ)$  and finish pose  $P_f(100,100,70^\circ)$ .

### 4.2.3 Dubins Path Generation using Differential Geometry

Differential geometry is more advanced compared to analytical geometry. In differential geometric approach, unity vector is used to represent a pose and at every point of the curve a local frame is considered which is called Frenet-Serret frame. Four different Dubins paths between two poses  $P_s(x_s, y_s, \varphi_s)$  and  $P_f(x_f, y_f, \varphi_f)$  are generated using this approach by obeying maximum start pose curvature  $\kappa_s = 1/r_s$  and finish pose curvature  $\kappa_f = 1/r_f$ . Figure 9 and Figure 10 are external tangent Dubins path generated by right-to-right and left-to-left turn and Figure 11 and Figure 12 are internal tangent Dubins path generated by right-to-left and left-to-right turn respectively. Shortest path is the minimum distance path among these four paths.

The Frenet-Serret frame at start pose and finish pose are  $\mathbf{e}_s = [\mathbf{t}_s \quad \mathbf{n}_s]$  and  $\mathbf{e}_f = [\mathbf{t}_f \quad \mathbf{n}_f]$  respectively. Here,

$$\mathbf{t}_s = \begin{bmatrix} \cos(\varphi_s) \\ \sin(\varphi_s) \end{bmatrix}; \quad \mathbf{n}_s = \begin{bmatrix} \cos(\varphi_s + \frac{\pi}{2}) \\ \sin(\varphi_s + \frac{\pi}{2}) \end{bmatrix}$$

$$\mathbf{t}_f = \begin{bmatrix} \cos(\varphi_f) \\ \sin(\varphi_f) \end{bmatrix}; \quad \mathbf{n}_f = \begin{bmatrix} \cos(\varphi_f + \frac{\pi}{2}) \\ \sin(\varphi_f + \frac{\pi}{2}) \end{bmatrix}$$

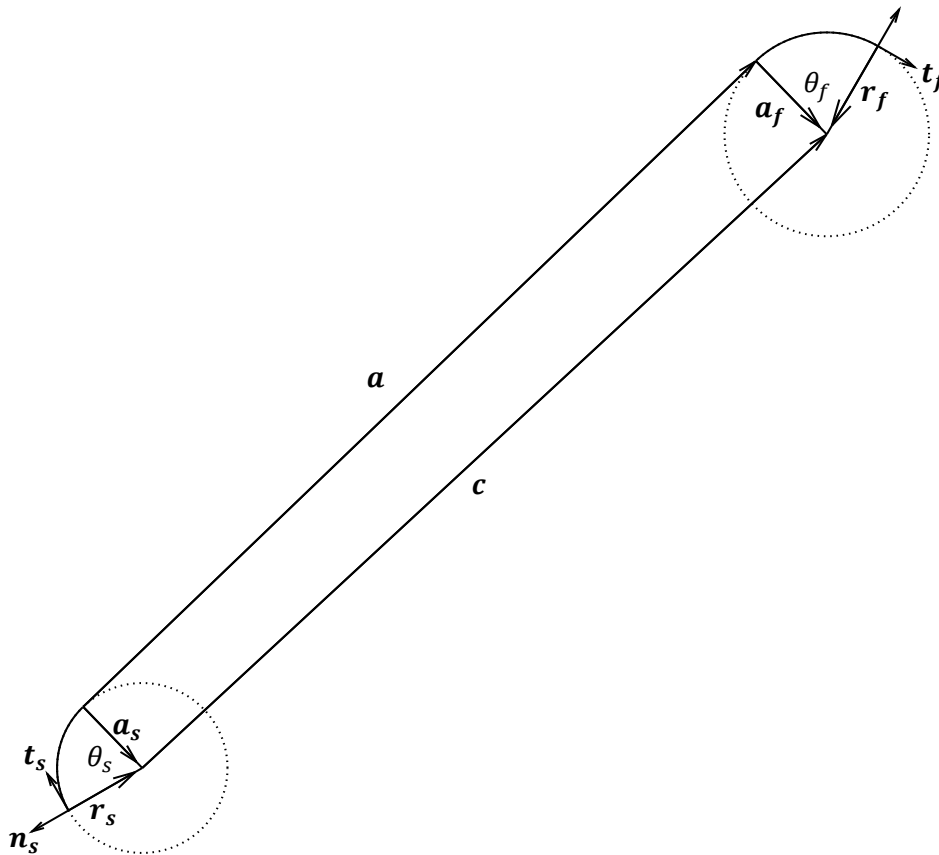


Figure-9: Dubins path for right-to-right turn ( $\varphi_s = 120^\circ, \varphi_f = 330^\circ$ )

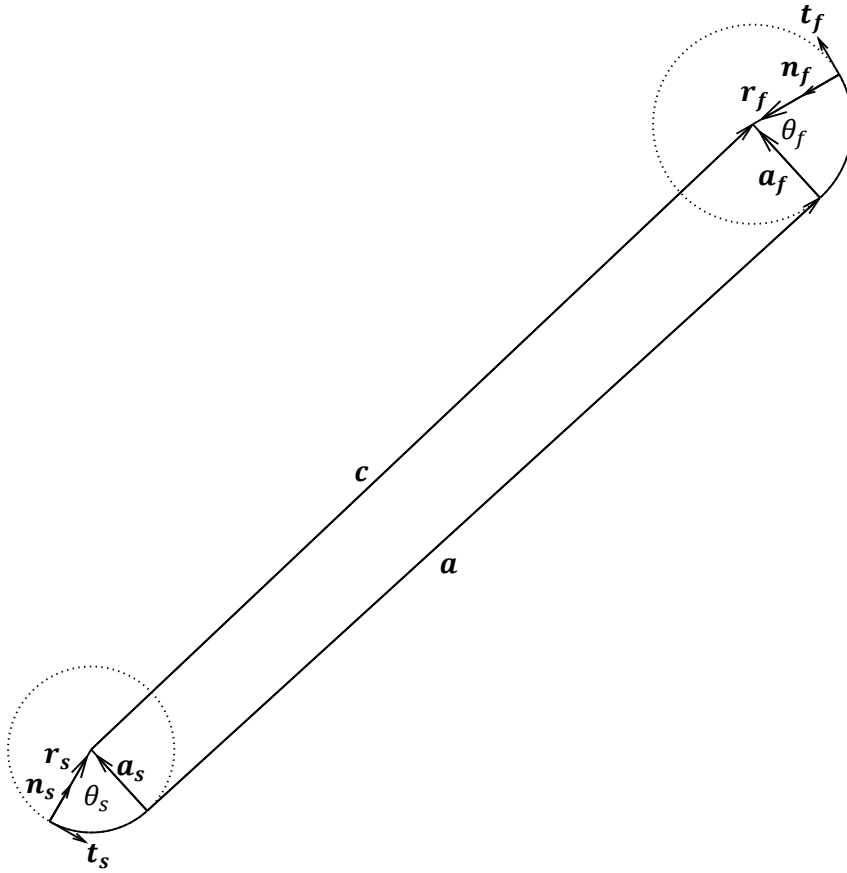


Figure-10: Dubins path for left-to-left turn ( $\varphi_s = 330^\circ, \varphi_f = 120^\circ$ )

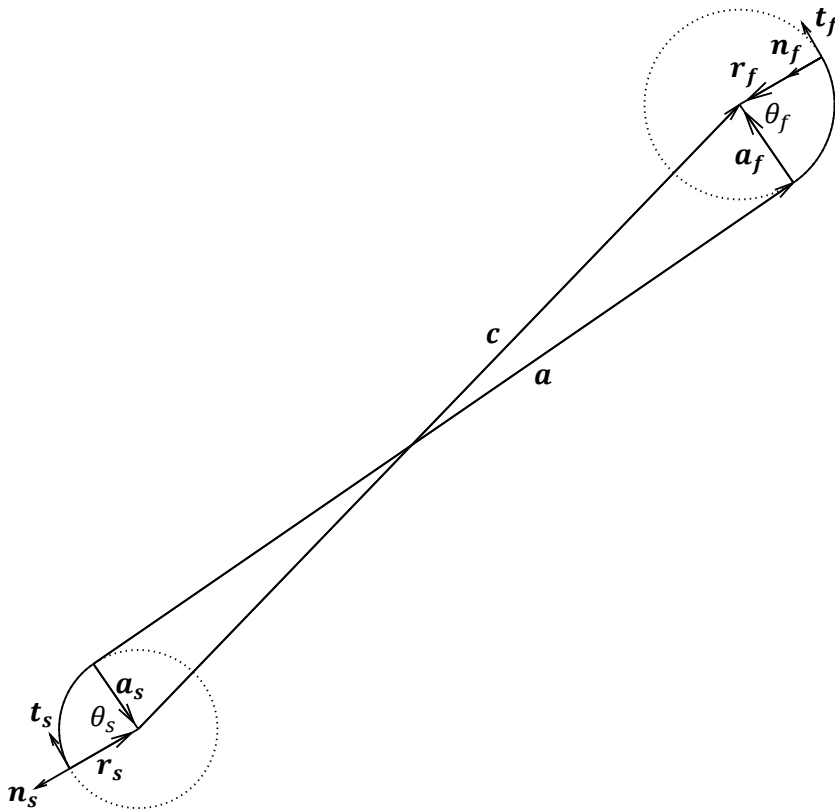


Figure-11: Dubins path for right-to-left turn ( $\varphi_s = 120^\circ, \varphi_f = 120^\circ$ )

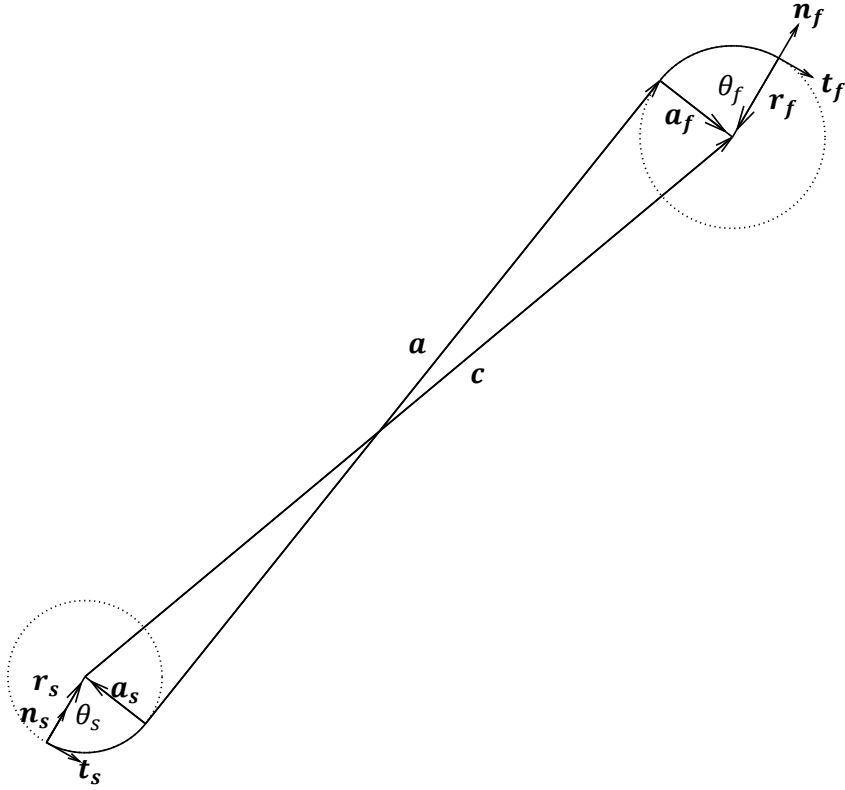


Figure-12: Dubins path for left-to-right turn ( $\varphi_s = 330^\circ, \varphi_f = 330^\circ$ )

Start circle radius and final circle radius are

$$\rho_s = \pm \frac{1}{\kappa_s}$$

$$\rho_f = \pm \frac{1}{\kappa_f}$$

Here, positive sign is used for left turn and negative sign is used for right turn. This initial assumption of sign eliminates sign confusion.

The vector from start position to finish position is

$$\mathbf{p} = \begin{bmatrix} x_f \\ y_f \end{bmatrix} - \begin{bmatrix} x_s \\ y_s \end{bmatrix}$$

From Figure 9-12, using vector addition, we have

$$\mathbf{c} = \mathbf{p} - \mathbf{r}_s + \mathbf{r}_f, \quad (1)$$

where

$$\mathbf{r}_s = \mathbf{e}_s \begin{bmatrix} 0 \\ \rho_s \end{bmatrix}$$

$$\mathbf{r}_f = \mathbf{e}_f \begin{bmatrix} 0 \\ \rho_f \end{bmatrix}$$

Again, using vector addition, we have

$$\mathbf{c} = -\mathbf{a}_s + \mathbf{a} + \mathbf{a}_f, \quad (2)$$

where

$$\mathbf{a}_s = \mathbf{e}_s \mathbf{R}(\theta_s) \begin{bmatrix} 0 \\ \rho_s \end{bmatrix}$$

$$\mathbf{a} = \mathbf{e}_s \mathbf{R}(\theta_s) \begin{bmatrix} a \\ 0 \end{bmatrix}$$

$$\mathbf{a}_f = \mathbf{e}_s \mathbf{R}(\theta_s) \begin{bmatrix} 0 \\ \rho_f \end{bmatrix}$$

and the rotation matrix is given by

$$\mathbf{R}(\theta_s) = \begin{bmatrix} \cos(\theta_s) & -\sin(\theta_s) \\ \sin(\theta_s) & \cos(\theta_s) \end{bmatrix}$$

Now, defining an unit vector  $\mathbf{t}_c = \mathbf{c}/c$ , where  $c = |\mathbf{c}|$ ,

$$\mathbf{c} = c \mathbf{t}_c$$

Equation (2) can be written as

$$c \mathbf{t}_c = -\mathbf{e}_s \mathbf{R}(\theta_s) \begin{bmatrix} 0 \\ \rho_s \end{bmatrix} + \mathbf{e}_s \mathbf{R}(\theta_s) \begin{bmatrix} a \\ 0 \end{bmatrix} + \mathbf{e}_s \mathbf{R}(\theta_s) \begin{bmatrix} 0 \\ \rho_f \end{bmatrix}$$

Up to here of this section, all vectors are defined with respect to the initial basis. Multiplying the above equation from the left by  $\mathbf{e}_s^T$ , it becomes

$$c \mathbf{e}_s^T \mathbf{t}_c = -\mathbf{R}(\theta_s) \begin{bmatrix} 0 \\ \rho_s \end{bmatrix} + \mathbf{R}(\theta_s) \begin{bmatrix} a \\ 0 \end{bmatrix} + \mathbf{R}(\theta_s) \begin{bmatrix} 0 \\ \rho_f \end{bmatrix}$$

Defining  $\mathbf{e}_s^T \mathbf{t}_c = \mathbf{t}_{ct}$ , which is actually the unit vector,  $\mathbf{t}_c$ , with respect to the start Frenet-Serret frame  $\mathbf{e}_s$ , the equation can be rewritten as

$$c \mathbf{t}_{ct} = -\mathbf{R}(\theta_s) \begin{bmatrix} 0 \\ \rho_s \end{bmatrix} + \mathbf{R}(\theta_s) \begin{bmatrix} a \\ 0 \end{bmatrix} + \mathbf{R}(\theta_s) \begin{bmatrix} 0 \\ \rho_f \end{bmatrix} = \mathbf{R}(\theta_s) \begin{bmatrix} a \\ \rho_f - \rho_s \end{bmatrix} \quad (3)$$

Equation (3) is a rotation equation. Hence,

$$\left| \begin{bmatrix} a \\ \rho_f - \rho_s \end{bmatrix} \right| = c$$

$$\text{or,} \quad \left( \frac{a}{c} \right)^2 = 1 - \left( \frac{\rho_f - \rho_s}{c} \right)^2$$

Solution of the above equation is feasible if

$$1 - \left( \frac{\rho_f - \rho_s}{c} \right)^2 > 0 \quad (4)$$

Now, replacing  $a$  in equation (3) gives

$$\mathbf{t}_{ct} = \mathbf{R}(\theta_s) \left( \frac{1}{c} \right) \begin{bmatrix} \sqrt{c^2 - (\rho_f - \rho_s)^2} \\ \rho_f - \rho_s \end{bmatrix} \quad (5)$$

The solution of the equation (5) is given by

$$\begin{bmatrix} \cos(\theta_s) \\ \sin(\theta_s) \end{bmatrix} = \left( \frac{1}{c} \right) \begin{bmatrix} \beta & \gamma \\ -\gamma & \beta \end{bmatrix} \mathbf{t}_{ct}, \quad (6)$$

where

$$\beta = \sqrt{c^2 - (\rho_f - \rho_s)^2}$$

$$\gamma = \rho_f - \rho_s$$

$c, \beta, \gamma$  and  $t_{ct}$  are known; therefore, initial rotation  $\theta_s$  can be calculated using equation (6). If angle between  $t_s$  and  $t_f$  is  $\theta$ , the final rotation angle is

$$\theta_f = \theta - \theta_s \quad (7)$$

and the path length is given by

$$\text{Path length} = \frac{\theta_s}{\kappa_s} + a + \frac{\theta_f}{\kappa_f}$$

**Example:** For start pose  $P_s(5,10,70^\circ)$  and finish pose  $P_f(100,100,10^\circ)$  four possible Dubins paths are simulated. Figure 13 shows that shortest path is the Dubins path for right-right turn.

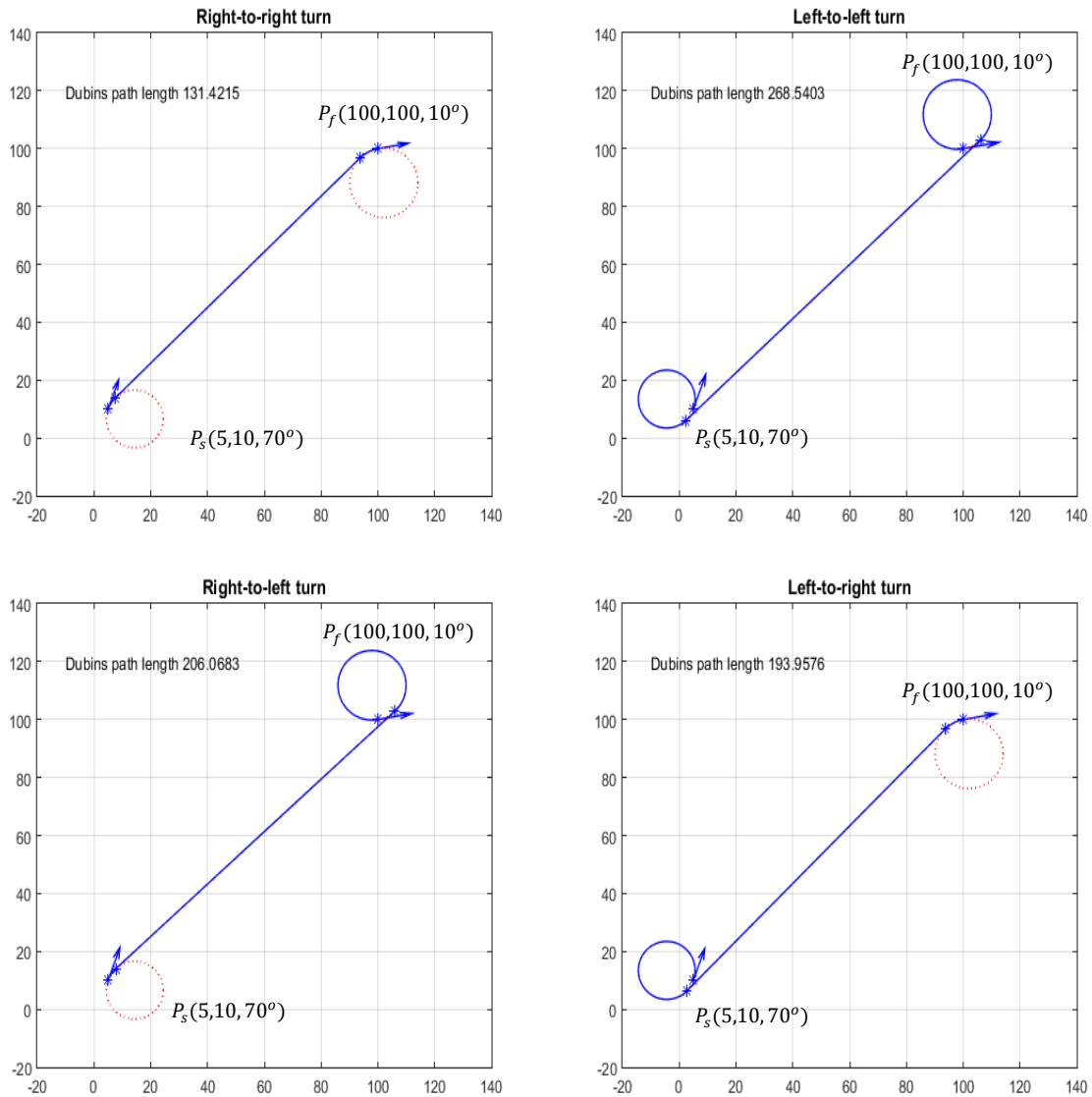


Figure-13: Four possible Dubins path for start pose  $P_s(5,10,70^\circ)$  and finish pose  $P_f(100,100,10^\circ)$ .

#### 4.2.4 Flyable Path with Continuous Curvature

Dubins path is the shortest path and its curvature changes from constant  $\kappa$  to zero at tangent exit point and zero to  $\kappa$  at tangent entry point. As curvature is directly proportional to lateral acceleration and the UAV cannot change the lateral acceleration suddenly, it is not able to follow the Dubins path. Thus, a

path is flyable if its curvature is continuous. For a curve  $\mathbf{r}(t) = (x(t), y(t))$ , the curvature can be expressed as

$$\kappa(t) = \frac{\dot{\mathbf{r}}(t) \times \ddot{\mathbf{r}}(t)}{|\dot{\mathbf{r}}(t)|^3} \quad (8)$$

where  $t$  is path parameter. Hence, for continuous curvature, the curve  $\mathbf{r}(t)$  should satisfy  $C^2$  continuity. Two methods of producing path with continuous curvature are introduced in [8]: i) Dubins path with clothoid arcs and ii) producing single curve with  $C^2$  continuity using Pythagorean Hodograph. In this section, more easier and complete algorithm compared to the one in [8], using complex algebra, for method (ii) is presented.

A parametric polynomial curve,  $\mathbf{r}(t) = (x(t), y(t))$ , is called Pythagorean-hodograph curve if derivative or hodograph of the curve,  $\dot{\mathbf{r}}(t) = (\dot{x}(t), \dot{y}(t))$ , satisfies the Pythagorean condition

$$\dot{x}^2(t) + \dot{y}^2(t) = \sigma^2(t) \quad (9)$$

To satisfy (9), a necessary and sufficient condition is that  $\dot{x}(t)$  and  $\dot{y}(t)$  can be represented by polynomials  $w(t)$ ,  $u(t)$  and  $v(t)$  as follows

$$\dot{x}(t) = w(t)(u^2(t) - v^2(t)) \quad (10)$$

$$\dot{y}(t) = 2w(t)u(t)v(t) \quad (11)$$

Choosing  $w(t) = 1$  and  $\gcd(u(t), v(t)) = 1$ , a primitive Pythagorean hodograph is produce. For shape flexible curve,  $u(t)$  and  $v(t)$  should be quadratic and resulted PH curve will be quintic (fifth order). Suppose, Bezier form of quadratic polynomials  $u(t)$  and  $v(t)$  are

$$u(t) = u_0(1-t)^2 + 2u_1t(1-t) + u_2t^2 \quad (12)$$

$$v(t) = v_0(1-t)^2 + 2v_1t(1-t) + v_2t^2 \quad (13)$$

and quintic PH curve in Bezier form is

$$\mathbf{r}(t) = \mathbf{p}_0(1-t)^5 + 5\mathbf{p}_1t(1-t)^4 + 10\mathbf{p}_2t^2(1-t)^3 + 10\mathbf{p}_3t^3(1-t)^2 + 5\mathbf{p}_4t^4(1-t) + \mathbf{p}_5t^5, \quad (14)$$

where  $\mathbf{p}_k = (x_k, y_k)$ ,  $k = 1, 2, 3, 4, 5$  are control points and  $t \in [0, 1]$ . Integrating equations (10) and (11) and equating with equation (14), the following solution can be calculated:

$$\mathbf{p}_1 = \mathbf{p}_0 + \frac{1}{5}(u_0^2 - v_0^2, 2u_0v_0)$$

$$\mathbf{p}_2 = \mathbf{p}_1 + \frac{1}{5}(u_0u_1 - v_0v_1, u_0v_1 + u_1v_0)$$

$$\mathbf{p}_3 = \mathbf{p}_2 + \frac{2}{15}(u_1^2 - v_1^2, 2u_1v_1) + \frac{1}{15}(u_0u_2 - v_0v_2, u_0v_2 + u_2v_0)$$

$$\mathbf{p}_4 = \mathbf{p}_3 + \frac{1}{5}(u_1u_2 - v_1v_2, u_1v_2 + u_2v_1)$$

$$\mathbf{p}_5 = \mathbf{p}_4 + \frac{1}{5}(u_2^2 - v_2^2, 2u_2v_2)$$

Now for complex representation, writing  $\mathbf{p}_k = x_k + i y_k$  and  $\mathbf{z}_i = u_i + i v_i$ , above solutions can be written into compact form as

$$\mathbf{p}_1 = \mathbf{p}_0 + \frac{1}{5} \mathbf{z}_0^2$$

$$\mathbf{p}_2 = \mathbf{p}_1 + \frac{1}{5} \mathbf{z}_0 \mathbf{z}_1$$

$$\mathbf{p}_3 = \mathbf{p}_2 + \frac{1}{15} (2 \mathbf{z}_1^2 + \mathbf{z}_0 \mathbf{z}_2) \quad 15$$

$$\mathbf{p}_4 = \mathbf{p}_3 + \frac{1}{5} \mathbf{z}_1 \mathbf{z}_2$$

$$\mathbf{p}_5 = \mathbf{p}_4 + \frac{1}{5} \mathbf{z}_2^2$$

Complex form representation of  $\dot{\mathbf{r}}(t) = (\dot{x}(t), \dot{y}(t))$  is

$$\begin{aligned}\dot{\mathbf{r}}(t) &= \dot{x}(t) + i \dot{y}(t) = u^2(t) - v^2(t) + i 2u(t)v(t) = (u(t) + i v(t))^2 \\ &= ((u_0 + i v_0)(1-t)^2 + 2(u_1 + i v_1)t(1-t) + (u_2 + i v_2)t^2)^2 \\ &= (\mathbf{z}_0(1-t)^2 + 2\mathbf{z}_1t(1-t) + \mathbf{z}_2t^2)^2\end{aligned}\quad (16)$$

From given initial pose  $P_s(x_s, y_s, \varphi_s)$  and final pose  $P_f(x_f, y_f, \varphi_f)$ , initial and final positions and directions are

$$\mathbf{p}_0 = x_s + i y_s$$

$$\mathbf{p}_5 = x_f + i y_f$$

$$\dot{\mathbf{r}}(0) = \mathbf{z}_0^2 = \mathbf{d}_0 = C_0(\cos(\varphi_s) + i \sin(\varphi_s)) \quad (17)$$

$$\dot{\mathbf{r}}(1) = \mathbf{z}_2^2 = \mathbf{d}_5 = C_5(\cos(\varphi_f) + i \sin(\varphi_f)) \quad (18)$$

Here,  $C_0$  and  $C_5$  are arbitrary constants. Values of these constants will be chosen iteratively to obey the curvature constraint of the path. From Hermite interpolation condition,

$$\int_0^1 \dot{\mathbf{r}}(t) dt = \mathbf{p}_5 - \mathbf{p}_0$$

or,

$$\mathbf{z}_0^2 + \mathbf{z}_0\mathbf{z}_1 + \frac{1}{3}(2\mathbf{z}_1^2 + \mathbf{z}_0\mathbf{z}_2) + \mathbf{z}_1\mathbf{z}_2 + \mathbf{z}_2^2 = 5(\mathbf{p}_5 - \mathbf{p}_0) \quad (19)$$

Solving equation (17) and (18), both  $\mathbf{z}_0$  and  $\mathbf{z}_2$  will have two solutions. Using the four combination of the solutions from  $\mathbf{z}_0$  and  $\mathbf{z}_2$ , in total eight solution of  $\mathbf{z}_1$  will be found. The number of unique solutions will be four. Once  $\mathbf{z}_0$ ,  $\mathbf{z}_1$  and  $\mathbf{z}_2$  are known, from equation (15), all control points of PH quintic will be found.

In complex form, equation (8) can be rewritten into

$$\kappa(t) = \frac{\text{Imag}(\bar{\dot{\mathbf{r}}}(t)\ddot{\mathbf{r}}(t))}{|\dot{\mathbf{r}}(t)|^3} \quad (20)$$

Taking derivative of equation (16),

$$\ddot{\mathbf{r}}(t) = 2(\mathbf{z}_0(t-1)^2 + t^2\mathbf{z}_2 - 2t\mathbf{z}_1(t-1))(\mathbf{z}_0(2t-2) - 2t\mathbf{z}_1 + 2t\mathbf{z}_2 - 2\mathbf{z}_1(t-1))$$

Flyable path will be chosen from four different PH path having minimum absolute rotation index or elastic bending energy [30]. Here, absolute rotation index is presented by

$$R_{abs} = \frac{1}{2\pi} \int_0^1 |\kappa(t)| |\dot{\mathbf{r}}(t)| dt$$

and elastic bending energy is presented by

$$E = \int_0^1 \kappa^2(t) |\dot{\mathbf{r}}(t)| dt$$

**Example:** Figure 14 shows four possible PH paths with absolute rotation index  $R_{abs}$ , and elastic bending energy  $E$ , for start pose  $P_s(5,10,120^\circ)$ , finish pose  $P_f(100,100,120^\circ)$ , and  $|\kappa_{max}| = 0.1$ . Constants  $C_0$  and  $C_5$  are iteratively calculated so that  $|\kappa(t)| < 0.1$ . Finally,  $C_0 = C_5 = 90$  is chosen where  $R_{abs} = 0.53503$ ,  $E = 0.1778$ , and  $|\kappa_{max}| = 0.0963$  are obtained, see top right subplot in Figure 14.

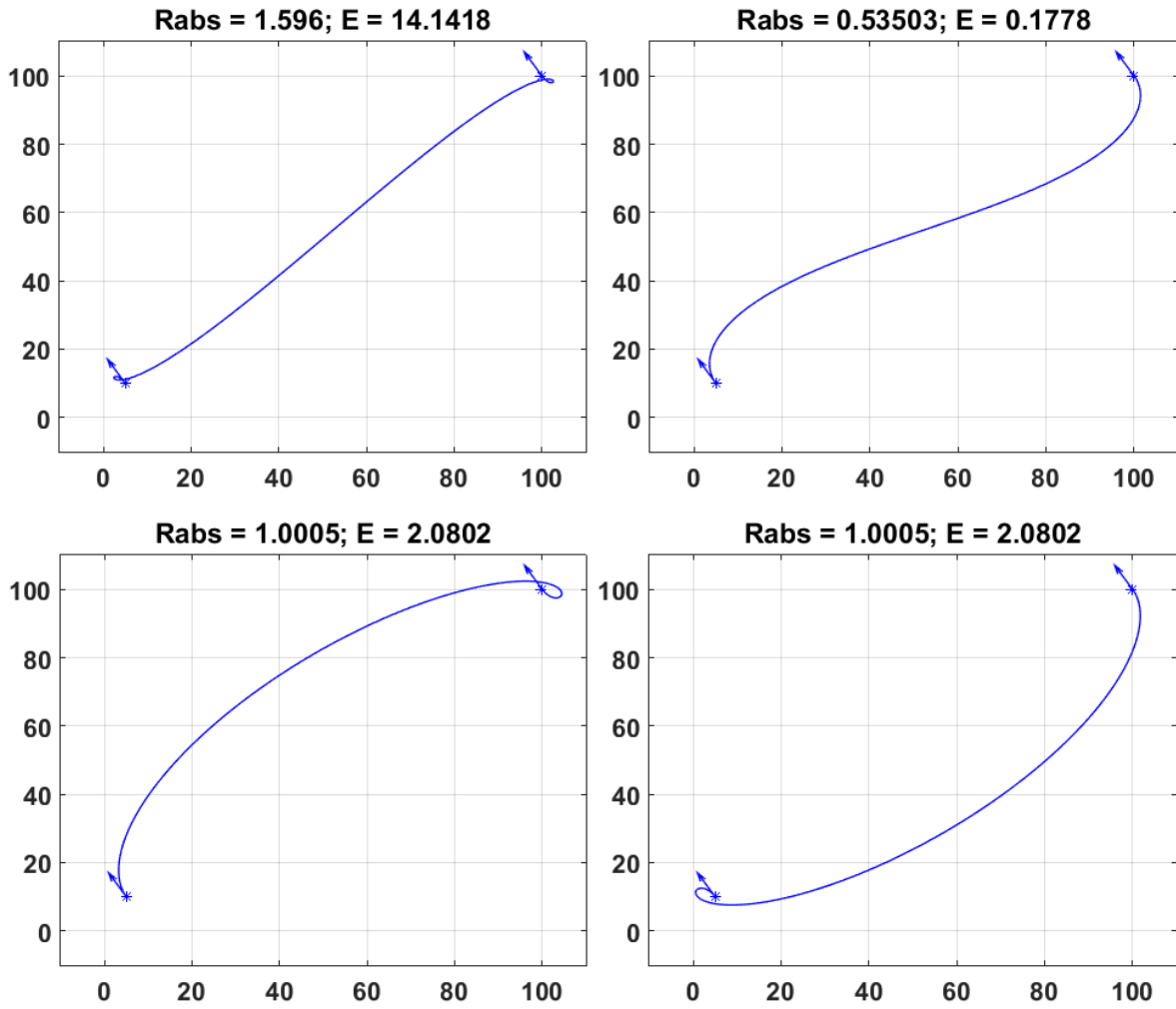


Figure-14: Four possible PH path for start pose  $P_s(5,10,120^\circ)$  and finish pose  $P_f(100,100,120^\circ)$ .

Figure 15 shows the corresponding curvature profile for all PH paths shown in Figure 14. All curvature profiles are continuous, but the curvature profile for minimum energy path changes very smoothly and follows the curvature constraint.

Figure 16 shows the comparison of Dubins and PH (dotted line) path for start pose  $P_s(5,10,120^\circ)$ , finish pose  $P_f(100,100,120^\circ)$  and  $|\kappa_{max}| = 0.1$ . PH path length is longer than Dubins path, but this path is easily flyable for its continuous curvature.

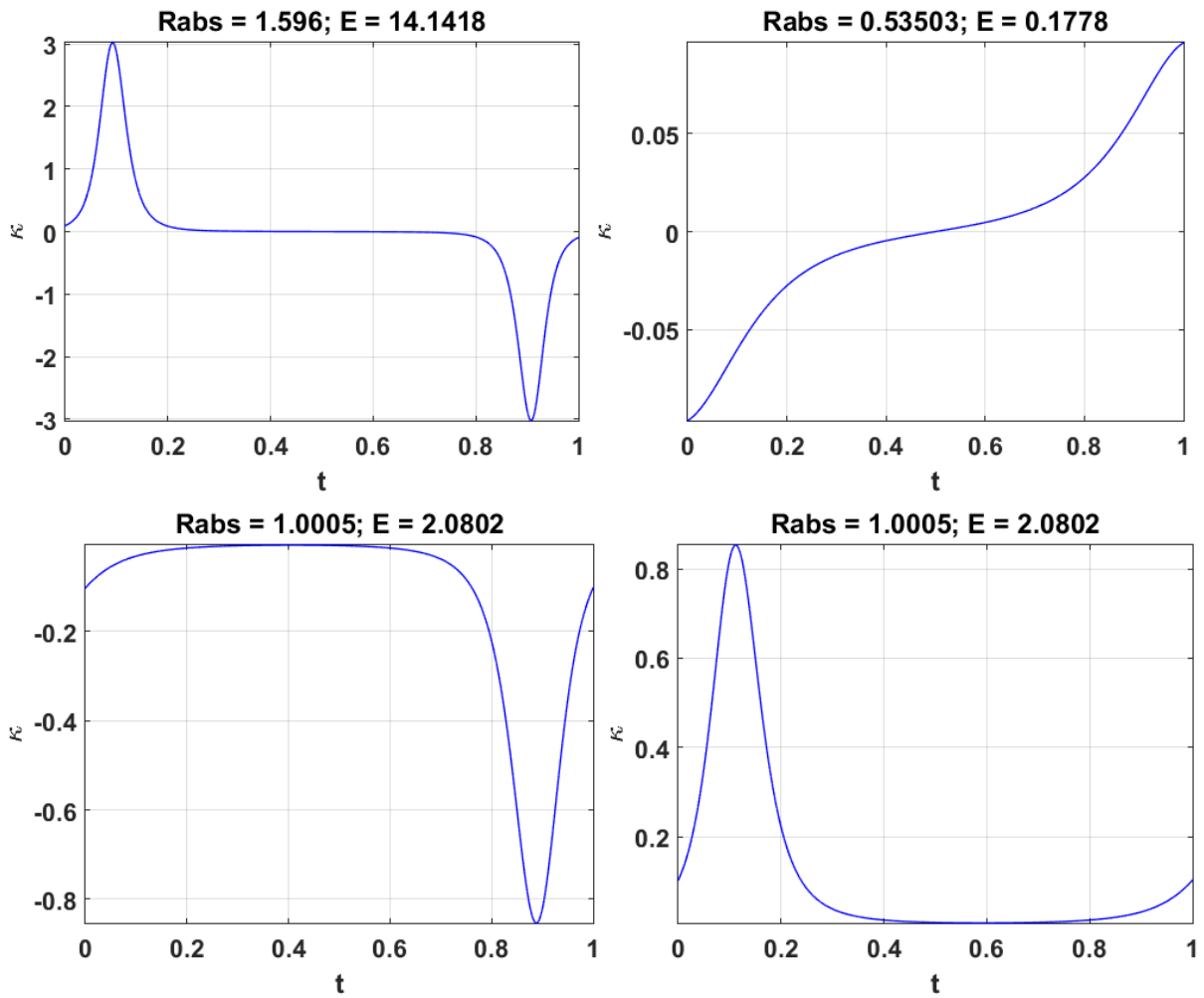


Figure-15: Curvature profile for corresponding PH paths in Figure 14.

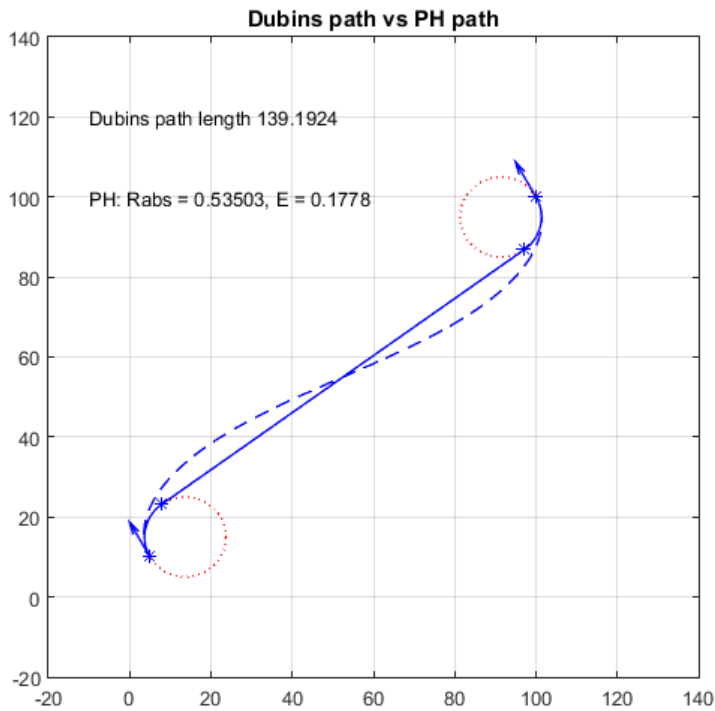


Figure-16: PH and Dubins path for start pose  $P_s(5,10,120^\circ)$  and finish pose  $P_f(100,100,120^\circ)$ .

### 4.3 Flyable Path Generation in 3D

#### 4.3.1 Problem Formulation

Similar to 2D flyable path generation, for 3D flyable path, there is no obstacle in the scenario. Now, start pose and final pose of UAV can be represented by  $P_s(x_s, y_s, z_s, \varphi_s, \theta_s)$  and  $P_f(x_f, y_f, z_f, \varphi_f, \theta_f)$  respectively,  $\varphi_s$  and  $\varphi_f$  are azimuth angles measured counter-clockwise from x-axis in x-y plane and  $\theta_s$  and  $\theta_f$  are elevation angles with x-y plane. For calculating the shortest flyable path, the problem can be mathematically defined as

$$P_s(x_s, y_s, z_s, \varphi_s, \theta_s) \xrightarrow{r(t)} P_f(x_f, y_f, z_f, \varphi_f, \theta_f), \quad (21)$$

where  $t$  is the path parameter and  $r(t)$  is the shortest flyable path. Dubins path is a shortest path between two poses which obeys curvature constraint  $|\kappa| \leq \kappa_{max}$  and torsion constraint  $|\tau| \leq \tau_{max}$ . This path is not flyable because its curvature is discontinuous at the joining point of constant curvature segment and straight line segment. To make the path flyable Pythagorean hodograph approach is used in this section.

#### 4.3.2 Flyable Path with Continuous Curvature and Torsion

For a 3D curve  $r(t) = (x(t), y(t), z(t))$ , curvature is

$$\kappa(t) = \frac{\dot{r}(t) \times \ddot{r}(t)}{|\dot{r}(t)|^3} \quad (22)$$

and torsion is

$$\tau(t) = \frac{(\dot{r}(t) \times \ddot{r}(t)) \cdot \dddot{r}(t)}{|\dot{r}(t) \times \ddot{r}(t)|^2} \quad (23)$$

Derivative or hodograph of the curve  $\dot{r}(t) = (\dot{x}(t), \dot{y}(t), \dot{z}(t))$  satisfies the Pythagorean condition

$$\dot{x}^2(t) + \dot{y}^2(t) + \dot{z}^2(t) = \sigma^2(t) \quad (24)$$

In [10], it is shown, necessary and sufficient condition to satisfy (24) is that  $\dot{x}(t)$ ,  $\dot{y}(t)$  and  $\dot{z}(t)$  can be represented by polynomials  $u(t)$ ,  $v(t)$ ,  $p(t)$  and  $q(t)$  as follows

$$\dot{x}(t) = u^2(t) + v^2(t) - p^2(t) - q^2(t) \quad (25)$$

$$\dot{y}(t) = 2(u(t)q(t) + v(t)p(t)) \quad (26)$$

$$\dot{z}(t) = 2(v(t)q(t) - u(t)p(t)) \quad (27)$$

The quadratic Bernstein form of these polynomials are

$$u(t) = u_0(1-t)^2 + 2u_1t(1-t) + u_2t^2 \quad (28)$$

$$v(t) = v_0(1-t)^2 + 2v_1t(1-t) + v_2t^2 \quad (29)$$

$$p(t) = p_0(1-t)^2 + 2p_1t(1-t) + p_2t^2 \quad (30)$$

$$q(t) = q_0(1-t)^2 + 2q_1t(1-t) + q_2t^2 \quad (31)$$

and quintic PH curve in Bezier form is

$$r(t) = \mathbf{p}_0(1-t)^5 + 5\mathbf{p}_1t(1-t)^4 + 10\mathbf{p}_2t^2(1-t)^3 + 10\mathbf{p}_3t^3(1-t)^2 + 5\mathbf{p}_4t^4(1-t) + \mathbf{p}_5t^5, \quad (32)$$

where  $\mathbf{p}_k = (x_k, y_k, z_k)$ ,  $k = 1, 2, 3, 4, 5$  are control points and  $t \in [0, 1]$ . Integrating equations (25), (26) and (27) and equating with equation (32), the following solution can be calculated

$$\mathbf{p}_1 = \mathbf{p}_0 + \frac{1}{5}(u_0^2 + v_0^2 - p_0^2 - q_0^2, 2u_0q_0 + 2v_0p_0, 2v_0q_0 - 2u_0p_0)$$

$$\mathbf{p}_2 = \mathbf{p}_1 + \frac{1}{5}(u_0u_1 + v_0v_1 - p_0p_1 - q_0q_1, u_0q_1 + u_1q_0 + v_0p_1 + v_1p_0, v_0q_1 + v_1q_0 - u_0p_1 - u_1p_0)$$

$$\mathbf{p}_3 = \mathbf{p}_2 + \frac{1}{15}(2u_1^2 + u_0u_2 + 2v_1^2 + v_0v_2 - 2p_1^2 - p_0p_2 - 2q_1^2 - q_0q_2, u_0q_2 + 4u_1q_1 + u_2q_0 + v_0p_2 + 4v_1p_1 + v_2p_0, v_0q_2 + 4v_1q_1 + v_2q_0 - u_0p_2 - 4u_1p_1 - u_2p_0)$$

$$\mathbf{p}_4 = \mathbf{p}_3 + \frac{1}{5}(u_1u_2 + v_1v_2 - p_1p_2 - q_1q_2, u_1q_2 + u_2q_1 + v_1p_2 + v_2p_1, v_1q_2 + v_2q_1 - u_1p_2 - u_2p_1)$$

$$\mathbf{p}_5 = \mathbf{p}_4 + \frac{1}{5}(u_2^2 + v_2^2 - p_2^2 - q_2^2, 2u_2q_2 + 2v_2p_2, 2v_2q_2 - 2u_2p_2)$$

For quaternion representation, writing  $\mathbf{p}_k = i x_k + j y_k + k z_k$  and  $\mathbf{A}_r = u_r + i v_r + j p_r + k q_r$ , above solutions can be written into compact form presented below

$$\mathbf{p}_1 = \mathbf{p}_0 + \frac{1}{5} \mathbf{A}_0 i \mathbf{A}_0^*$$

$$\mathbf{p}_2 = \mathbf{p}_1 + \frac{1}{10} (\mathbf{A}_0 i \mathbf{A}_1^* + \mathbf{A}_1 i \mathbf{A}_0^*)$$

$$\mathbf{p}_3 = \mathbf{p}_2 + \frac{1}{30} (4 \mathbf{A}_1 i \mathbf{A}_1^* + \mathbf{A}_0 i \mathbf{A}_2^* + \mathbf{A}_2 i \mathbf{A}_0^*) \quad 33$$

$$\mathbf{p}_4 = \mathbf{p}_3 + \frac{1}{10} (\mathbf{A}_1 i \mathbf{A}_2^* + \mathbf{A}_2 i \mathbf{A}_1^*)$$

$$\mathbf{p}_5 = \mathbf{p}_4 + \frac{1}{5} \mathbf{A}_2 i \mathbf{A}_2^*$$

Quaternion form representation of  $\dot{\mathbf{r}}(t) = (\dot{x}(t), \dot{y}(t), \dot{z}(t))$  is

$$\begin{aligned} \dot{\mathbf{r}}(t) &= i \dot{x}(t) + j \dot{y}(t) + k \dot{z}(t) \\ &= i(u^2(t) + v^2(t) - p^2(t) - q^2(t)) + j 2(u(t)q(t) + v(t)p(t)) + k 2(v(t)q(t) - u(t)p(t)) \\ &= (\mathbf{A}_0(1-t)^2 + 2\mathbf{A}_1 t(1-t) + \mathbf{A}_2 t^2) i (\mathbf{A}_0(1-t)^2 + 2\mathbf{A}_1 t(1-t) + \mathbf{A}_2 t^2)^* \\ &= \mathbf{A}(t) i \mathbf{A}^*(t) \end{aligned} \quad (34)$$

From given initial pose  $P_s(x_s, y_s, z_s, \varphi_s, \theta_s)$  and final pose  $P_f(x_f, y_f, z_f, \varphi_f, \theta_f)$ , initial and final positions and directions are

$$\mathbf{p}_0 = i x_s + j y_s + k z_s$$

$$\mathbf{p}_5 = i x_f + j y_f + k z_f$$

$$\dot{\mathbf{r}}(0) = \mathbf{A}_0 i \mathbf{A}_0^* = \mathbf{d}_0 = C_0(i \cos(\theta_s) \cos(\varphi_s) + j \cos(\theta_s) \sin(\varphi_s) + k \sin(\theta_s)) \quad (35)$$

$$\dot{\mathbf{r}}(1) = \mathbf{A}_2 i \mathbf{A}_2^* = \mathbf{d}_5 = C_5(i \cos(\theta_f) \cos(\varphi_f) + j \cos(\theta_f) \sin(\varphi_f) + k \sin(\theta_f)) \quad (36)$$

Here,  $C_0$  and  $C_5$  are arbitrary constants. Values of these constants will be chosen iteratively to obey the curvature and torsion constraints of the path. From Hermite interpolation condition,

$$\int_0^1 \dot{\mathbf{r}}(t) dt = \mathbf{p}_5 - \mathbf{p}_0$$

or,

$$\begin{aligned} (3\mathbf{A}_0 + 4\mathbf{A}_1 + 3\mathbf{A}_2) i (3\mathbf{A}_0 + 4\mathbf{A}_1 + 3\mathbf{A}_2)^* \\ = 120(\mathbf{p}_5 - \mathbf{p}_0) - 15(\mathbf{d}_0 + \mathbf{d}_5) + 5(\mathbf{A}_0 i \mathbf{A}_2^* + \mathbf{A}_2 i \mathbf{A}_0^*) \end{aligned} \quad (37)$$

Solving equation (35) and (36),  $\mathbf{A}_0$  and  $\mathbf{A}_2$  can be calculated as follows

$$\begin{aligned} \mathbf{A}_0 = \sqrt{\frac{1}{2}(1 + \lambda_0)|\mathbf{d}_0|} \left( -\sin(\phi_0) + i \cos(\phi_0) + j \frac{\mu_0 \cos(\phi_0) + v_0 \sin(\phi_0)}{1 + \lambda_0} \right. \\ \left. + k \frac{v_0 \cos(\phi_0) - \mu_0 \sin(\phi_0)}{1 + \lambda_0} \right) \end{aligned} \quad (38)$$

$$\mathbf{A}_2 = \sqrt{\frac{1}{2}(1 + \lambda_5)|\mathbf{d}_5|} \left( -\sin(\phi_2) + i \cos(\phi_2) + j \frac{\mu_5 \cos(\phi_2) + \nu_5 \sin(\phi_2)}{1 + \lambda_5} + k \frac{\nu_5 \cos(\phi_2) - \mu_5 \sin(\phi_2)}{1 + \lambda_5} \right) \quad (39)$$

Here,  $\phi_0$  and  $\phi_2$  are variables, values of these variables will be chosen iteratively to obey the curvature and torsion constraints and

$$\frac{\mathbf{d}_0}{|\mathbf{d}_0|} = i \lambda_0 + j \mu_0 + k \nu_0$$

$$\frac{\mathbf{d}_5}{|\mathbf{d}_5|} = i \lambda_5 + j \mu_5 + k \nu_5$$

Considering  $\mathbf{B} = 3\mathbf{A}_0 + 4\mathbf{A}_1 + 3\mathbf{A}_2$  and  $\mathbf{d} = 120(\mathbf{p}_5 - \mathbf{p}_0) - 15(\mathbf{d}_0 + \mathbf{d}_5) + 5(\mathbf{A}_0 i \mathbf{A}_2^* + \mathbf{A}_2 i \mathbf{A}_0^*)$  equation (37) can be written as  $\mathbf{B}i\mathbf{B}^* = \mathbf{d}$ , which is same as equation (35) and (36), and solved as

$$\mathbf{B} = \sqrt{\frac{1}{2}(1 + \lambda)|\mathbf{d}|} \left( -\sin(\phi_1) + i \cos(\phi_1) + j \frac{\mu \cos(\phi_1) + \nu \sin(\phi_1)}{1 + \lambda} + k \frac{\nu \cos(\phi_1) - \mu \sin(\phi_1)}{1 + \lambda} \right)$$

or,

$$\mathbf{A}_1 = -\frac{3}{4}(\mathbf{A}_0 + \mathbf{A}_2) + \frac{1}{4} \sqrt{\frac{1}{2}(1 + \lambda)|\mathbf{d}|} \left( -\sin(\phi_1) + i \cos(\phi_1) + j \frac{\mu \cos(\phi_1) + \nu \sin(\phi_1)}{1 + \lambda} + k \frac{\nu \cos(\phi_1) - \mu \sin(\phi_1)}{1 + \lambda} \right), \quad (40)$$

where  $\phi_1$  is a variable which will also be chosen iteratively to obey the curvature and torsion constraints, and

$$\frac{\mathbf{d}}{|\mathbf{d}|} = i \lambda + j \mu + k \nu$$

Figure 17 shows lowest energy PH path with bending energy  $E$  for start pose  $P_s(0,0,0, 120^0, 0^0)$ , finish pose  $P_f(0,0,0, 120^0, 10^0)$ ,  $|\kappa_{max}| = 0.1$ , and  $|\tau_{max}| = 0.05$ .  $C_0, C_5, \phi_0, \phi_1$  and  $\phi_2$  are iteratively calculated so that  $|\kappa(t)| < 0.1$  and  $|\tau(t)| < 0.05$ . Reference [10] showed that considering  $\phi_1 = -\pi/2$  minimum bending energy curve will be found where values of  $\phi_0$  and  $\phi_2$  are closer to  $-\pi/2$ . Finally,  $C_0 = C_5 = 100$ ,  $\phi_1 = -\pi/2$ ,  $\phi_0 = -1.5\pi/2$ , and  $\phi_2 = -0.7\pi/2$  give minimum bending energy path following all constraints. Equation (22) and (23) are solved and plotted in Figure 18. Bending energy is calculated using equation

$$E = \int_0^1 (\kappa^2(t) + \tau^2(t)) |\dot{\mathbf{r}}(t)| dt \quad (41)$$

From equation (34)

$$\dot{\mathbf{r}}(t) = \dot{\mathbf{A}}(t)i\mathbf{A}^*(t) + \mathbf{A}(t)i\dot{\mathbf{A}}^*(t)$$

$$\ddot{\mathbf{r}}(t) = \ddot{\mathbf{A}}(t)i\mathbf{A}^*(t) + 2\dot{\mathbf{A}}(t)i\dot{\mathbf{A}}^*(t) + \mathbf{A}(t)i\ddot{\mathbf{A}}^*(t),$$

where

$$\mathbf{A}(t) = \mathbf{A}_0(1 - t)^2 + 2\mathbf{A}_1 t(1 - t) + \mathbf{A}_2 t^2$$

$$\dot{\mathbf{A}}(t) = \mathbf{A}_0(2t - 2) + 2\mathbf{A}_1(1 - 2t) + 2\mathbf{A}_2 t$$

$$\ddot{\mathbf{A}}(t) = 2\mathbf{A}_0 - 4\mathbf{A}_1 + 2\mathbf{A}_2$$

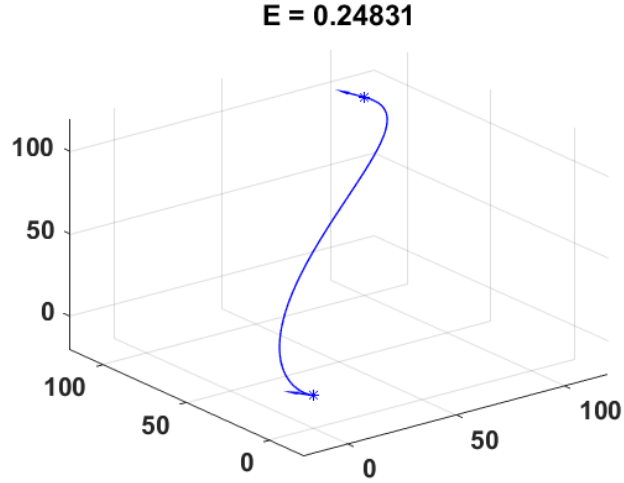


Figure-17: 3D PH path for start pose  $P_s(0,0,0, 120^0, 0^0)$  and finish pose  $P_f(0,0,0, 120^0, 10^0)$ .

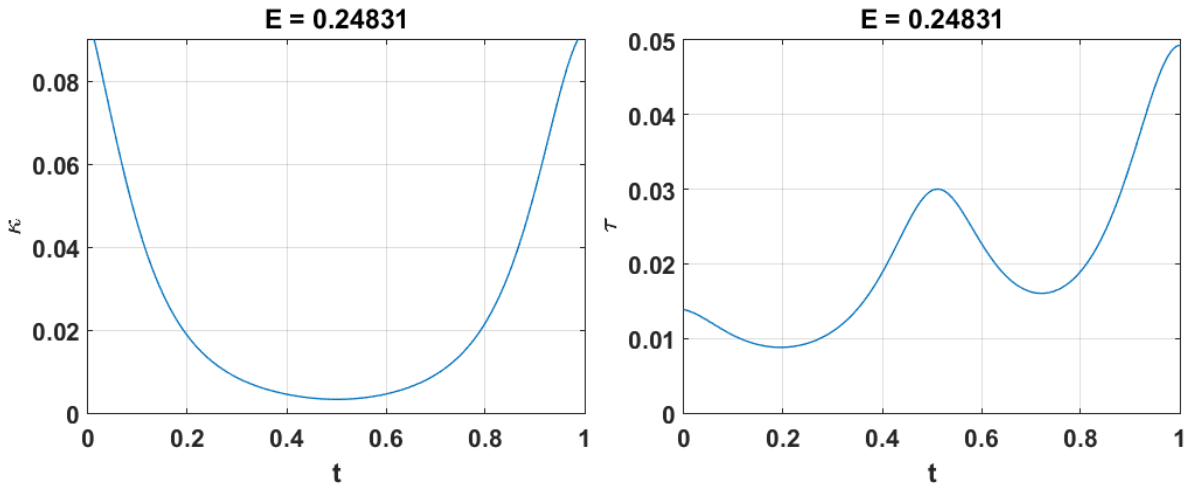


Figure-18: Curvature and torsion profile for 3D PH paths in Figure 17.

## 4.4 Flyable Lawn-mower Search Path Generation

### 4.4.1 Problem Formulation

For autonomous operation of UAV a flyable search path is generated prior to launching of the UAV where one or more unmapped static or dynamic obstacles are present. We are not considering any mapped obstacles in the sea environment. Thus, there is no obstacles in the initial flyable path. More precisely, UAV is launched from a launching pose  $P_l(x_l, y_l, z_l, \varphi_l, \theta_l)$  and travelled 3D flyable path up to lawn-mower search path start pose  $P_s(x_s, y_s, z, \varphi_s, 0^0)$ . Then UAV flies 2D flyable lawn-mower search path and again 3D flyable path to return from lawn-mower search path finish pose  $P_f(x_f, y_f, z, \varphi_f, 0^0)$  to the retrieval pose  $P_r(x_r, y_r, z_r, \varphi_r, \theta_r)$ . Finally, during the flight, if a collision is detected, 3D flyable path will be generated to avoid the collision without much deviating from the search path. Collision avoidance part will be discussed in the section 4.5.

### 4.4.2 Flyable Search Path with Continuous Curvature and Torsion

The algorithms used in section 4.2 and 4.3 are combined to generate flyable path for complete mission. Figure 19 shows the simulation result for complete mission for launching pose  $P_l(0,0,0, 120^0, 20^0)$ , lawn-mower search path start pose  $P_s(100,100,100, 0^0, 0^0)$ , lawn-mower search path finish pose

$P_f(100,1025,100,180^0,0^0)$  and retrieval pose  $P_r(0,5,5,300^0,-10^0)$ . Here, curvature and torsion constraints are  $|\kappa(t)| < 0.1$  and  $|\tau(t)| < 0.05$  respectively. Figure 20, 21 and 22 showed that all flyable path segments obey the curvature and torsion constraints.

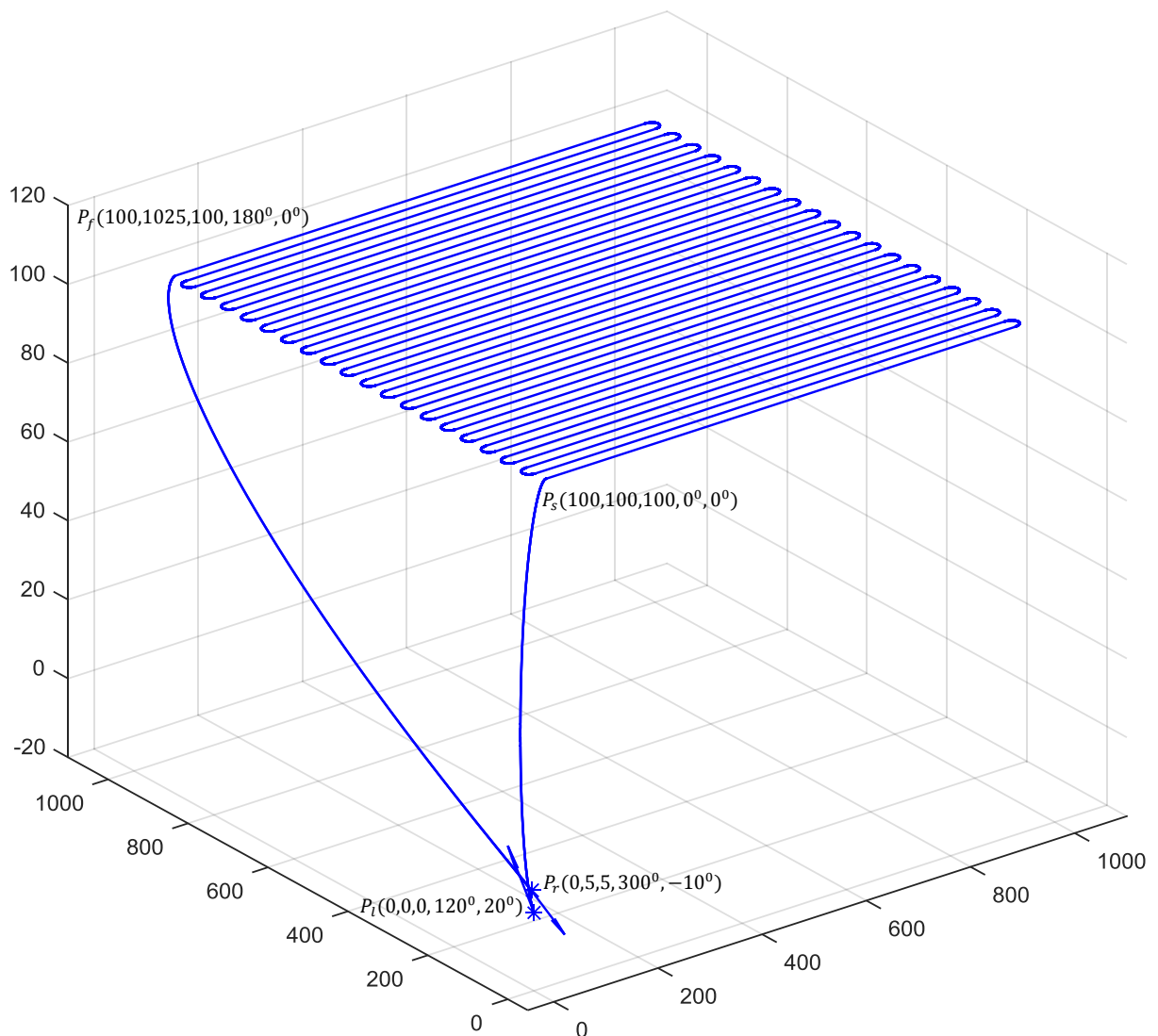


Figure-19: Flyable lawn-mower search path for launching pose  $P_l(0,0,0,120^0,20^0)$  and retrieval pose  $P_r(0,5,5,300^0,-10^0)$

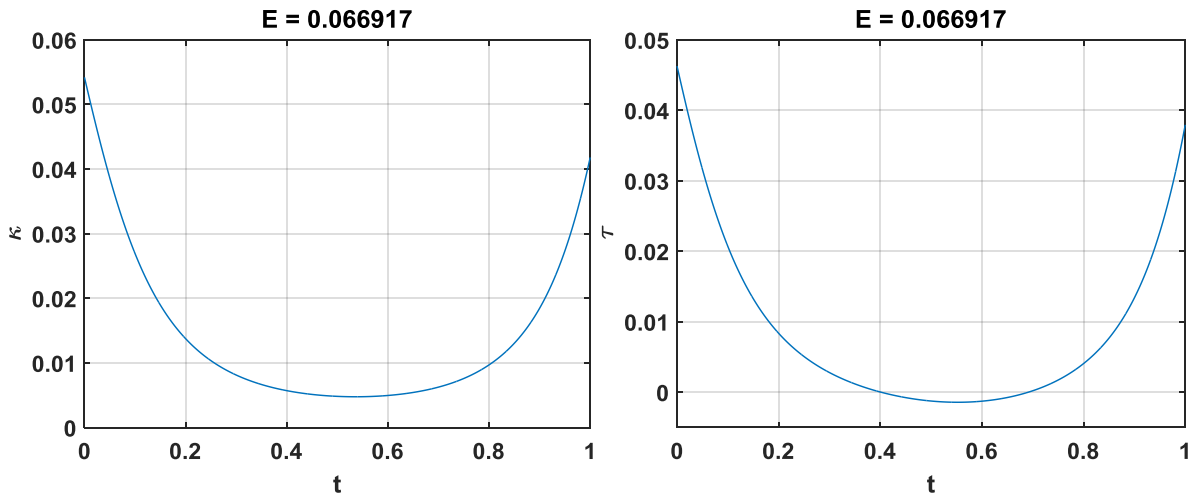


Figure-20: Curvature and torsion profile for 3D flyable path from launching pose  $P_l(0,0,0, 120^0, 20^0)$  to lawn-mower search path start pose  $P_s(100,100,100, 0^0, 0^0)$

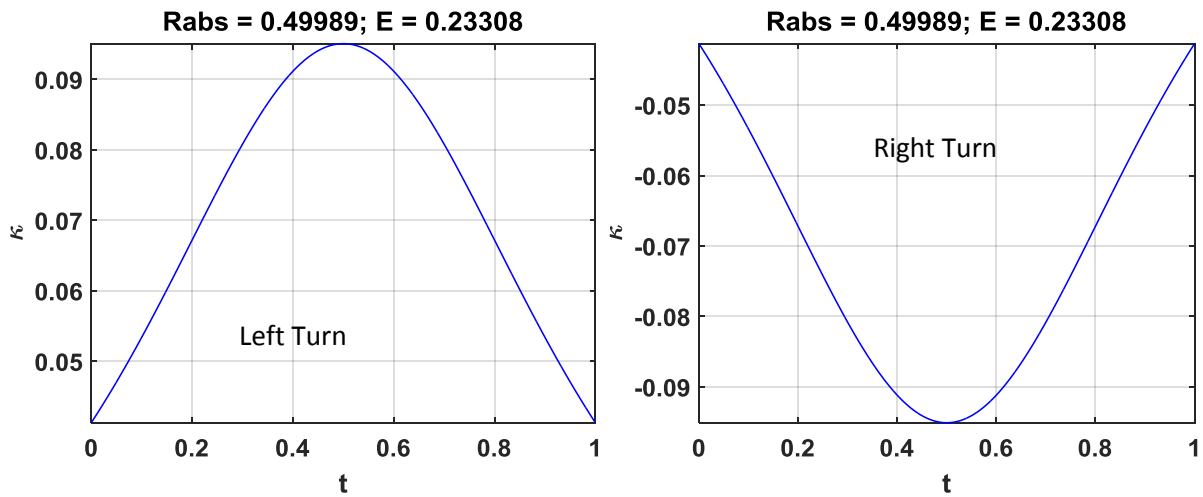


Figure-21: Curvature profile for left and right turn in lawn-mower search path from start pose  $P_s(100,100,100, 0^0, 0^0)$  to finish pose  $P_f(100,1025,100, 180^0, 0^0)$

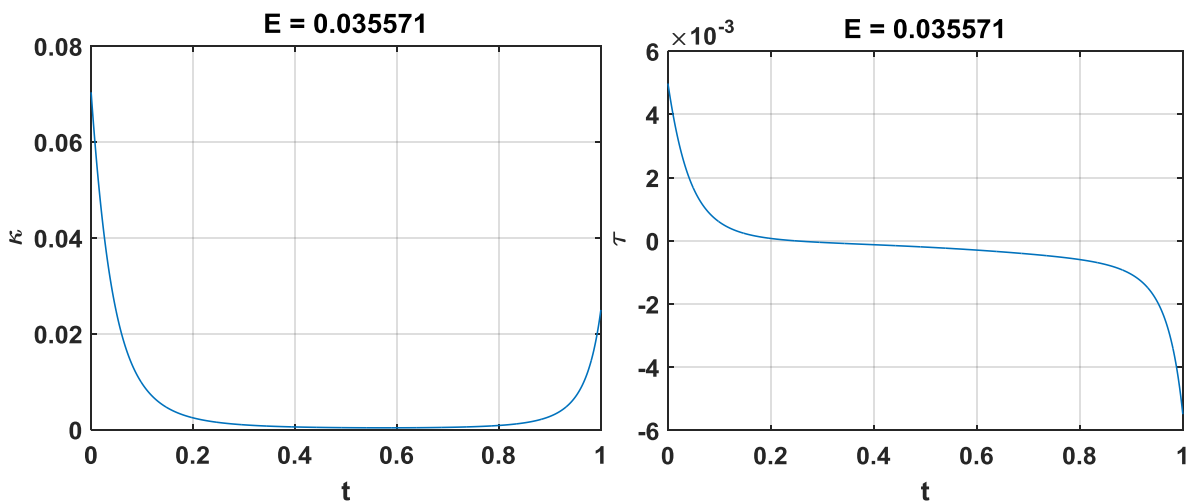


Figure-22: Curvature and torsion profile for 3D flyable path from lawn-mower search path finish pose  $P_f(100,1025,100, 180^0, 0^0)$  to retrieval pose  $P_r(0,5,5, 300^0, -10^0)$ .

#### 4.5 Collision Avoidance

Flyable path generation by considering mapped static obstacle avoidance is done by global path planner. Sensors mounted in the ship continuously sense unmapped static and dynamic obstacles in the scenario. When an obstacle is detected, the processor mounted in the ship will re-plan the path to avoid the collision. As it is assumed that there is no mapped static obstacles in the sea environment, a detailed discussion is presented on unmapped obstacles only.

Let's consider a UAV flying from a start pose to its final pose and sensors mounted in the ship continuously monitoring the air space. At a certain instant, UAV is flying at speed  $\mathbf{V}_{UAV}$  and an aerial vehicle (AV) is detected with speed  $\mathbf{V}_{AV}$ . If UAV is getting closer to the AV, after a certain amount of time, UAV will reach a certain point when distance between the UAV and the AV is minimum. This minimum distance is called miss distance, the point is called closest point of approach (CPA) and the time is called CPA time. In the Figure 23, miss distance vector is  $\mathbf{r}_m$ .

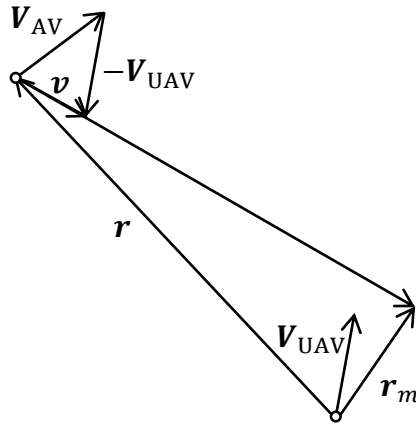


Figure-23: Calculation of miss distance and CPA time.

**Conflict detection:** The relative velocity between the UAV and the aerial vehicle is  $\mathbf{v} = \mathbf{V}_{AV} - \mathbf{V}_{UAV}$ . Defining the unit vector  $\hat{\mathbf{v}} = \mathbf{v}/|\mathbf{v}|$ , miss distance vector is

$$\mathbf{r}_m = \hat{\mathbf{v}} \times \mathbf{r} \times \hat{\mathbf{v}}, \quad (42)$$

where  $\mathbf{r}$  is relative distance vector. As  $\mathbf{r}_m$  and  $\mathbf{v}$  is orthogonal, according to the property of vector dot product

$$\mathbf{r}_m \cdot \mathbf{v} = 0 \quad (43)$$

Now, if CPA time is  $\tau$ , from Figure 23, using vector addition, we have

$$\mathbf{r}_m = \mathbf{r} + \tau \mathbf{v} \quad (44)$$

Hence, using equation 43 and 44, CPA time is

$$\tau = \frac{\mathbf{r} \cdot \mathbf{v}}{\mathbf{v} \cdot \mathbf{v}} \quad (45)$$

In equation 45, when  $\tau > 0$ , UAV and aerial vehicle are getting closer and when  $\tau < 0$ , they are going further from each other. If  $|\mathbf{r}_m|$  is less than minimum required separation  $r_s$ , this is considered as a conflict. Thus, conflict condition is

$$r_d = r_s - |\mathbf{r}_m| > 0 \quad (46)$$

**Conflict resolution:** If a conflict is detected, from Figure 23, it is easy to understand that miss distance vector can be increased by turning both UAV and AV to the left. For cooperative conflict resolution two new intermediate way points,  $P_U$  and  $P_A$  for UAV and AV respectively, are created in Figure 24.

These intermediate positions are calculated by using vector addition

$$P_U = P_{UAV} + \tau \mathbf{V}_{UAV} + \mathbf{r}_U \quad (47)$$

$$P_A = P_{AV} + \tau \mathbf{V}_{AV} + \mathbf{r}_A \quad (48)$$

Here,  $P_{UAV}$  is the UAV position and  $P_{AV}$  is the AV position at the time of conflict detection,

$$\mathbf{r}_U = \frac{r_d |\mathbf{V}_{AV}|}{|\mathbf{V}_{UAV}| + |\mathbf{V}_{AV}|} \frac{-\mathbf{r}_m}{|\mathbf{r}_m|}$$

and

$$\mathbf{r}_A = \frac{r_d |\mathbf{V}_{UAV}|}{|\mathbf{V}_{UAV}| + |\mathbf{V}_{AV}|} \frac{\mathbf{r}_m}{|\mathbf{r}_m|}$$

For non-cooperative conflict resolution

$$\mathbf{r}_U = r_d \frac{-\mathbf{r}_m}{|\mathbf{r}_m|}$$

and

$$\mathbf{r}_A = 0$$

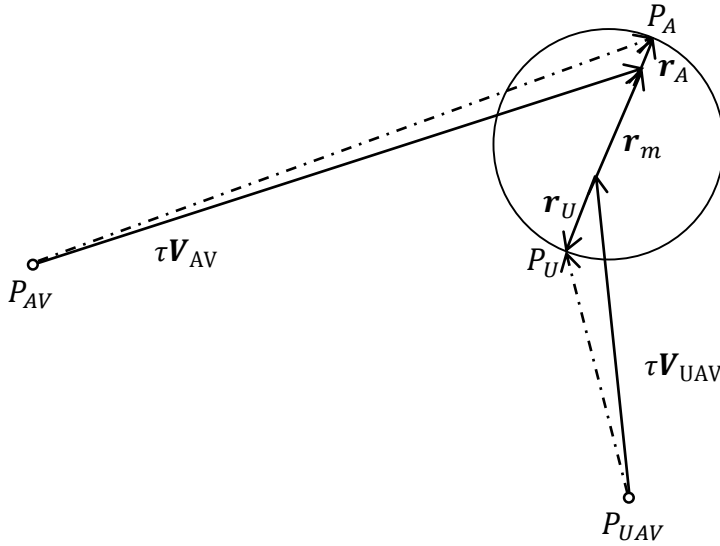


Figure-24: Conflict resolution by creating intermediate way points.

**Example:** Figure 25 shows the simulation result for 2D collision avoidance. Here, a UAV is heading from pose  $(100, 100, 0^0)$  to the pose  $(1000, 100, 0^0)$  at speed 15 unit/s and an AV is heading from the pose  $(1500, 800, 227.5^0)$  to the pose  $(400, -400, 227.5^0)$  at speed 20 unit/s. In this scenario, a conflict is detected with miss distance 21.1889. By considering safe distance 100, using the algorithm already discussed, an intermediate position is created at  $(795.1519, 170.0072, 27.34^0)$  for non-cooperative collision avoidance, and the flyable path planning algorithm is used to generate new flyable path.

Figure 26 shows the simulation result for 3D collision avoidance. Here, a UAV is heading from position  $(100, 100, 100, 0^0, 0^0)$  to the position  $(1000, 100, 100, 0^0, 0^0)$  at speed 15 unit/s and an AV is heading from the position  $(1500, 800, 120, 227.5^0, -1.41^0)$  to the position  $(400, -400, 80, 227.5^0, -1.41^0)$  at speed 20 unit/s. In this scenario, a conflict is detected where miss distance is 21.1889. By considering safe distance 100, using the algorithm already discussed, an intermediate position is created at  $(795.8022, 168.4738, 114.4851, 26.49^0, 5.39^0)$  for non-cooperative collision avoidance, and flyable

path planning algorithm is used to generate new flyable path. The azimuth and elevation angle of this intermediate point is calculated by considering that great circle in Figure 26 is on the plane containing miss distance vector and final position.

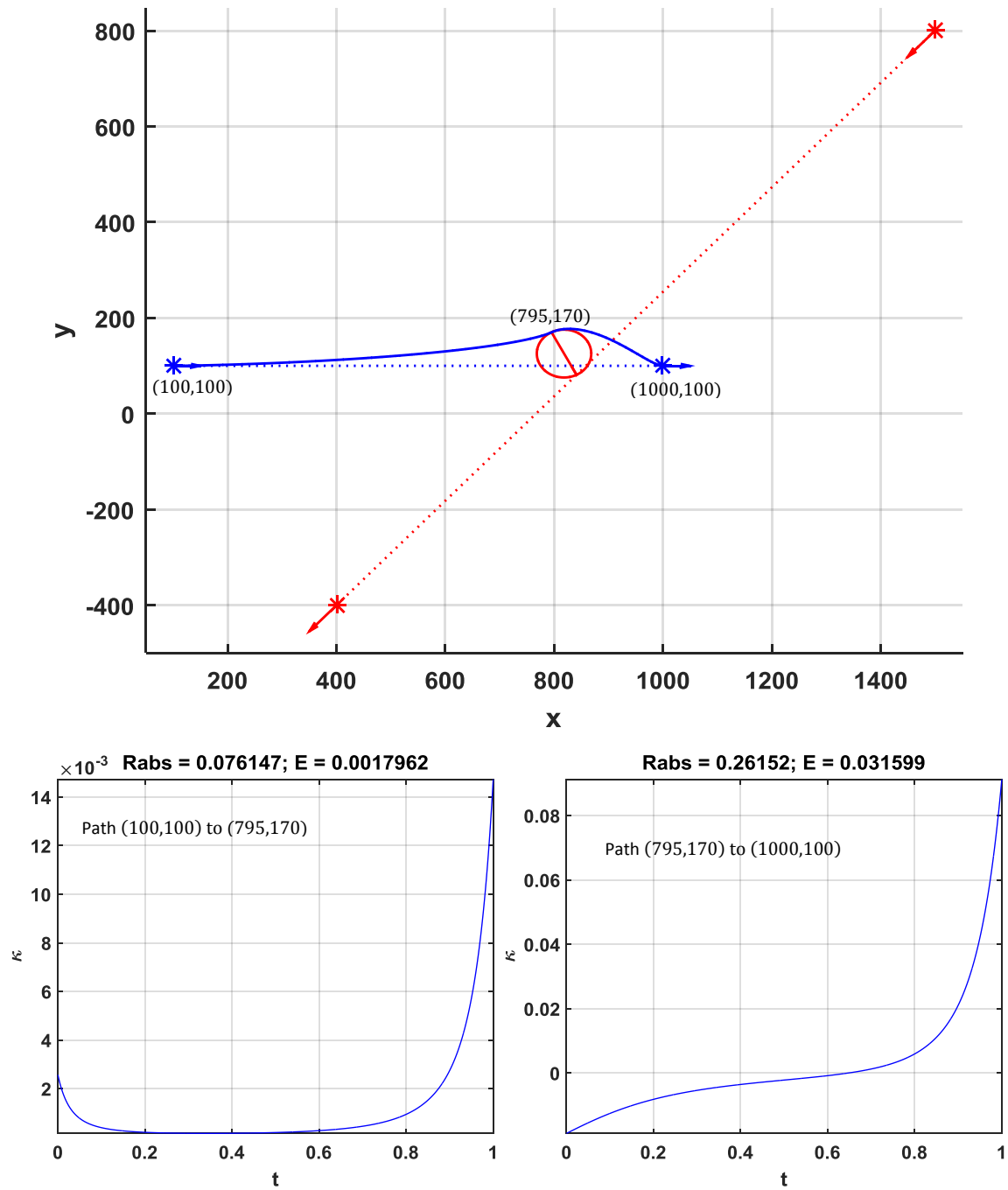


Figure-25: UAV collision avoidance in 2D.

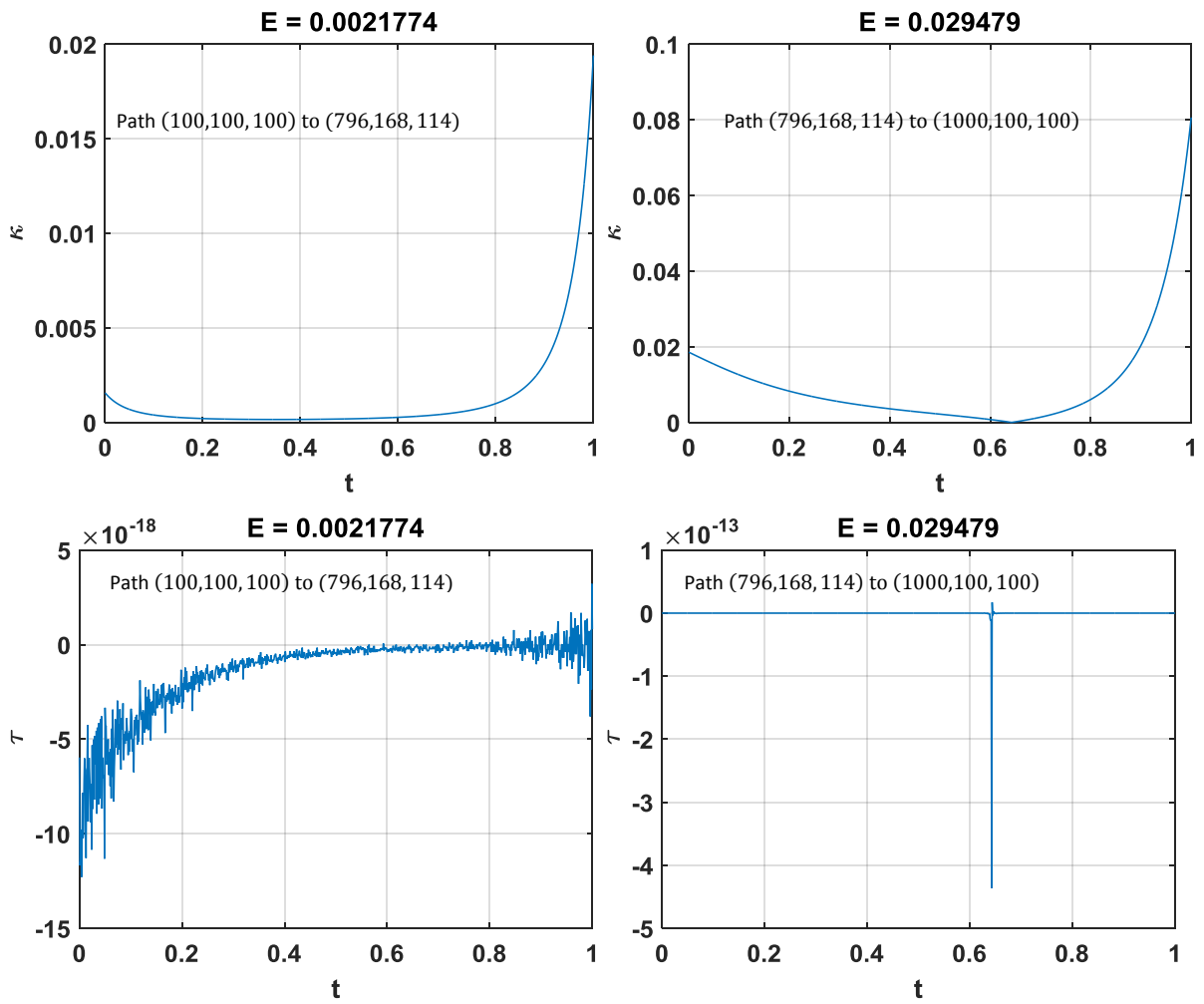
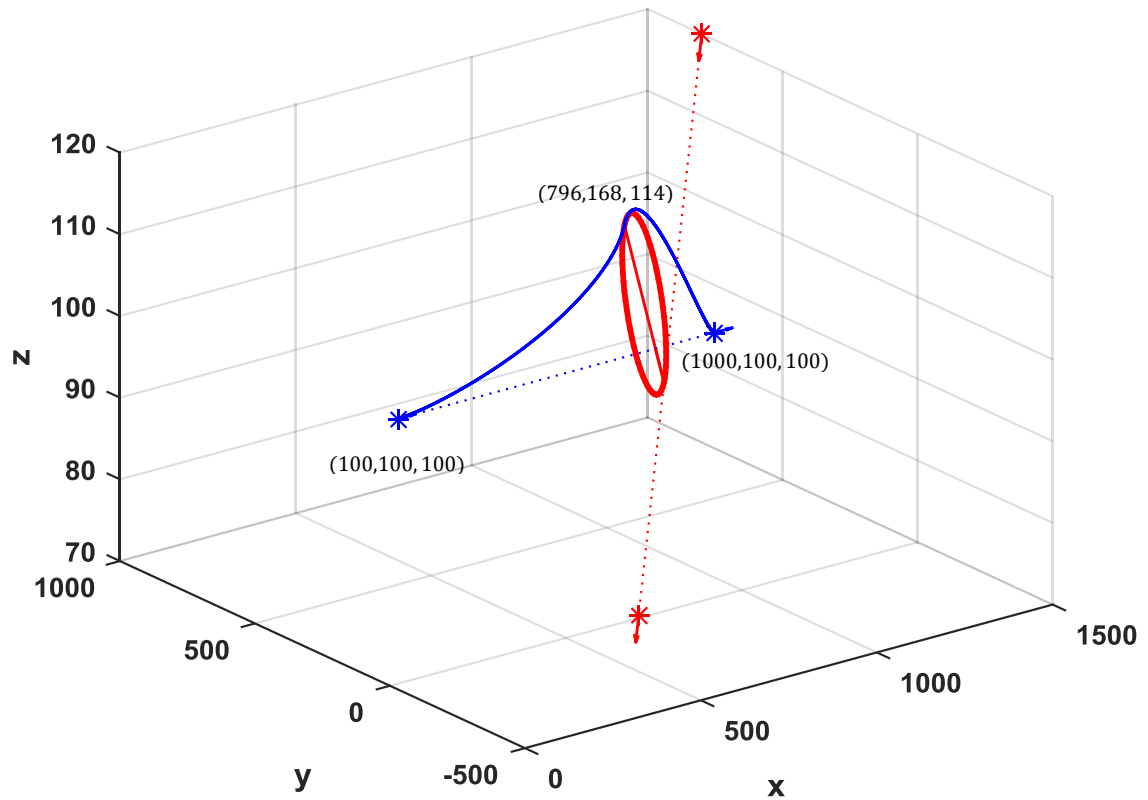


Figure-26: UAV collision avoidance in 3D.



## **5. Conclusion**

Using existing FMCW ship radar might be difficult to detect non-cooperative aerial vehicles, but there are low cost alternative in defence based on solid state radar transmitter which is used for simultaneous air and marine detection.

The algorithms for 2D and 3D flyable path generation from initial pose to a final pose are described and simulated clearly. However, when these algorithms are used for flyable search path generation, transition from one section of the path to another section sometimes presents a small curvature discontinuity. This should be handled carefully during implementation of the algorithms, or further study is required to solve this issue.

Simple collision avoidance algorithm based on intermediate way point generation is described and simulated. Similar but not same method is used for ship collision avoidance.

## **6. Future Work**

One important future work is the validation of the algorithms for flyable path generation and collision avoidance. Study on path following guidance is the next step of this thesis work. Further study on FMCW ship radar for detecting high speed aerial vehicles is also important – characterizing the situation where existing FMCW ship is feasible without much modification and using available low cost alternatives.



## 7. References

- [1] <http://www.detect-inc.com/security.html> (Accessed: 26th May 2015)
- [2] Corucci L. et al., 'An X-band Radar-Based Airborne Collision Avoidance System Proof of Concept', Radar Symposium (IRS), 2014 15th International, DOI: 10.1109/IRS.2014.6869238.
- [3] Roos J. C., Peddle I. K., 'Autonomous Take-Off and Landing of a Low Cost Unmanned Aerial Vehicle', R & D Journal of the South African Institution of Mechanical Engineering 2009, 25.
- [4] Shouzhao S. et al., 'Autonomous takeoff and landing control for a prototype unmanned helicopter', Control Engineering Practice 18 (2010) 1053–1059, Elsevier Ltd.
- [5] Peng K. et al., 'Design and implementation of an autonomous flight control law for a UAV helicopter', Automatica 45 (2009) 2333-2338, Elsevier Ltd.
- [6] Skulstad R. et al., 'Net Recovery of UAV with Single-Frequency RTK GPS', Proc. of the IEEE Aerospace Conference, Big Sky, Montana, 7-14 March, 2015.
- [7] Johansen T. A., Zolich A. et al., 'Unmanned Aerial Vehicle as Communication Relay for Autonomous Underwater Vehicle – Field Tests', IEEE Globecom Workshops 2014, DOI: 10.1109/GLOCOMW.2014.7063641
- [8] Tsourdos A., White B., Shanmugavel M., 'Cooperative Path Planning of Unmanned Aerial Vehicles' John Wiley & Sons, 2011.
- [9] Farouki, R. T., 'The elastic bending energy of pythagorean-hodograph curves', Computer Aided Geometric Design, 1996.
- [10] Farouki R.T., Al-Kandari M., Sakkalis T. 'Hermite interpolation by rotation-invariant spatial Pythagorean hodograph', Advances in Computational Mathematics, Volume 17 (369–383), 2002.
- [11] Park J. W. et al., 'UAV Collision Avoidance Based on Geometric Approach', SICE Annual Conference, 2008, IEEE, DOI: 10.1109/SICE.2008.4655013.
- [12] Carbone C. et al., 'A Novel 3D Geometric Algorithm for Aircraft Autonomous Collision Avoidance', Proceedings of the 45th IEEE Conference on Decision & Control, 2006.
- [13] Moccia A., 'A Novel 3D Analytical Algorithm for Autonomous Collision Avoidance Considering Cylindrical Safety Bubble', IEEE Aerospace Conference, Big Sky, 2010.
- [14] Briggs J. N., 'Target Detection by Marine Radar', The Institution of Engineering and Technology, United Kingdom, 2009.
- [15] Skolnik M. I., 'RADAR HANDBOOK', Third edition, New York: McGraw-Hill, 2008
- [16] Ward K., Tough R., Watts S., 'Sea Clutter: Scattering, the K-Distribution and Radar Performance', Second edition, The Institution of Engineering and Technology, United Kingdom, 2013
- [17] Ellonen I., Kaama A., 'Rain Clutter Filtering from Radar Data with Slope Based Filter', 2006, 3rd European Radar Conference, IEEE DOI: 10.1109/EURAD.2006.280264
- [18] Ellonen I., Kaama A., 'Rain Clutter Filtering from Radar Data with Discrete Wavelet Transform', 2006, International Radar Symposium, IEEE DOI: 10.1109/IRS.2006.4338033
- [19] Tuzlukov. V. P., 'Signal and image processing in navigational systems', CRC Press, 2004
- [20] Özdemir C., 'Inverse Synthetic Aperture Radar Imaging with MATLAB Algorithms', John Wiley & Sons, 2012
- [21] O'Donnell R. M., 'Free Video Course in Radar Systems Engineering', IEEE Aerospace and Electronic Systems Society and IEEE New Hampshire Section, Available at: <http://aess.cs.unh.edu/> (Accessed: 29th June 2014)
- [22] Schikorr M., 'HIGH RANGE RESOLUTION WITH DIGITAL STRETCH PROCESSING', Radar Conference, 2008. RADAR '08. IEEE.
- [23] Watts S., 'Cell-averaging CFAR gain in spatially correlated K-distributed clutter', IEE Proc.-Radar, Sonar Navig., Vol. 143, No. 5, October 1996

- [24] Axelsson, Sune R.J., 'Area Target Response of Triangularly Frequency-Modulated Continuous-Wave Radars', Aerospace and Electronic Systems, IEEE Transactions on (Volume: AES-14, Issue: 2), IEEE DOI: 10.1109/TAES.1978.308647
- [25] Langer D., 'An Integrated MMW Radar System for Outdoor Navigation', Thesis report for Doctor of Philosophy in Robotics.
- [26] 'Guidelines for GNSS positioning in the oil & gas industry', Report No. 373-19 June 2011, International Association of Oil & Gas Producers & International Marine Contractors Association.
- [27] Richards W.R., O'Brien K., Miller D.C., 'New Air Traffic Surveillance Technology'.
- [28] 'Guidelines for the installation of a shipborne Automatic Identification System (AIS)', International Maritime Organization, SN/Circ.227, 6 January 2003.
- [29] Chao H., Cao Y., Chen Y., 'Autopilots for Small Unmanned Aerial Vehicles: A Survey', International Journal of Control, Automation, and Systems 8(1):36-44 DOI 10.1007/s12555-010-0105-z (2010).
- [30] Farouki, R. T., 'Pythagorean – Hodograph Curves: Algebra and Geometry Inseparable', 2008.
- [31] Mahafza. B. R., 'Radar Systems Analysis and Design Using MATLAB', Third edition, CRC Press, 2013
- [32] Stove A.G., 'Linear FMCW radar techniques', IEE Proceedings-F, Volume No. 139, Issue 5, October 1992, Page(s):343 - 350.
- [33] Ward K. D., 'Compound representation of high resolution sea clutter', Electronics Letter, Vol.17, No. 16, 561–563, August 1981
- [34] Wolff C., 'Radar Basic', available at: <http://www.radartutorial.eu/index.en.html> (Accessed: 29th June 2014)
- [35] Leus G., 'Multi-Carrier Acoustic Underwater Communication', Conference lecture, March 2011, Available at: <http://tv.campusdomar.es/en/video/91.html/> (Accessed: 15th October 2014)
- [36] Farouki, R. T., Neff, C. A., 'Hermite interpolation by pythagorean hodograph quintics'. Mathematics of Computation, 1995.
- [37] Dietz R., Hoschek J., Jüttler B., 'An algebraic approach to curves and surfaces on the sphere and on other quadrics', Computer Aided Geometric Design (211–229), 1993.
- [38] Ajami A., Balmat J., Gaulthier J. P., Maillot T., 'Path Planning and Ground Control Station Simulator for UAV', Aerospace Conference, 2013 IEEE.
- [39] Ousingsawat J., Earl M. G., 'Modified Lawn-Mower Search Pattern for Areas Comprised of Weighted Regions', Proceedings of the 2007 American Control Conference, July 2007.
- [40] Nex F., Remondino F., 'UAV for 3D mapping applications: a review', Springer Berlin Heidelberg, Journal of Applied Geomatics, March 2014, Volume 6, Issue 1, pp 1-15, DOI 10.1007/s12518-013-0120-x.
- [41] Luo C. et al., 'UAV Position Estimation and Collision Avoidance Using the Extended Kalman Filter', IEEE TRANSACTIONS ON VEHICULAR TECHNOLOGY, VOL. 62, NO. 6, JULY 2013.
- [42] Valavanis K.P., 'Advances in Unmanned Aerial Vehicles – State of the Art and the Road to Autonomy', 2007 Spinger.
- [43] Fahroo F. et al., 'Recent Advances in Research on Unmanned Aerial Vehicles', Springer-Verlag Berlin Heidelberg 2013.
- [44] Leira F.S., Johansen T. A., 'Automatic Detection, Classification and Tracking of Objects in the Ocean Surface from UAVs Using a Thermal Camera', IEEE Aerospace Conference, Big Sky, 2015.